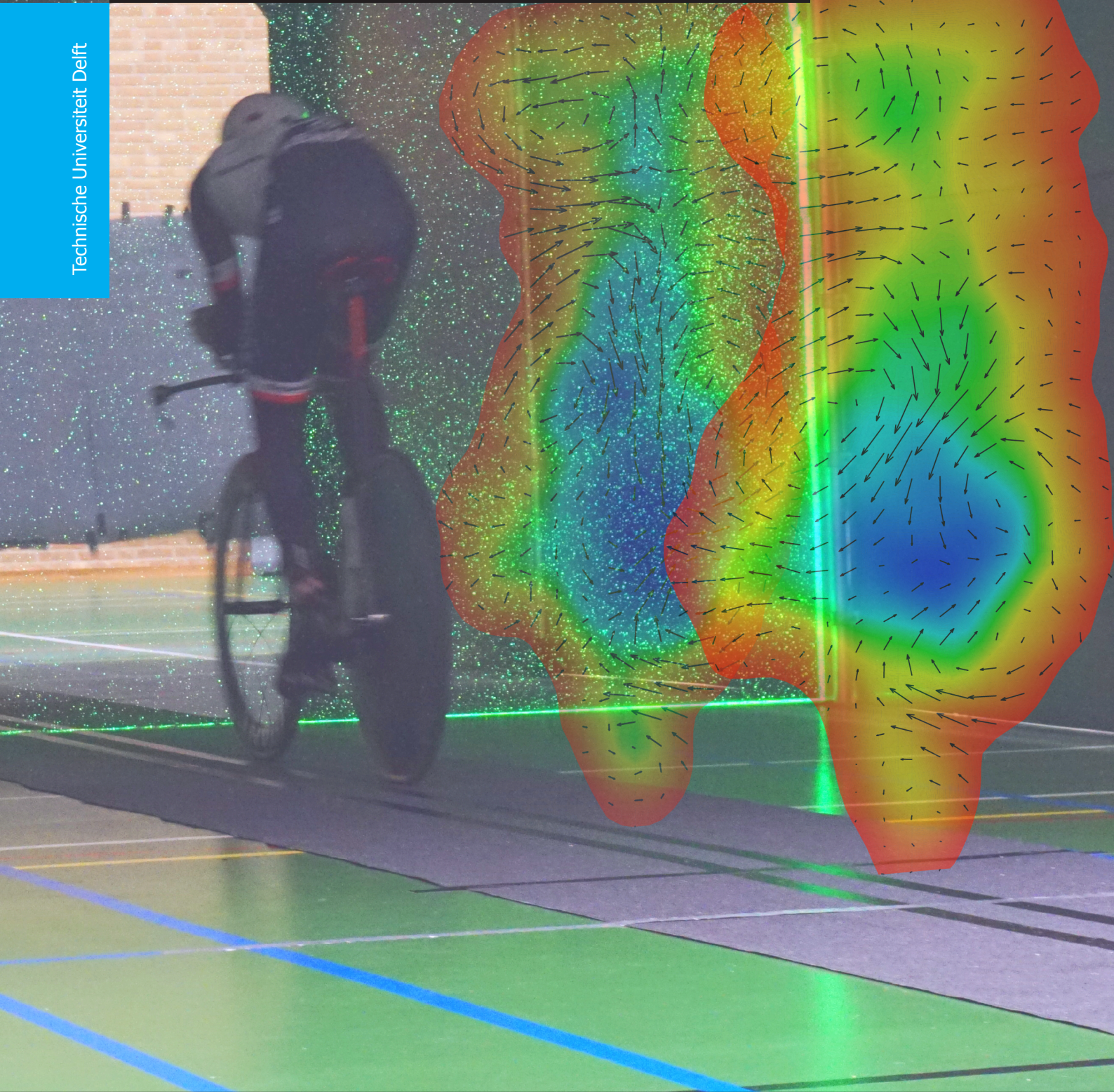


# Advances and assessment of the Ring of Fire concept for on-site cycling aerodynamics

Luigi de Martino Norante

Technische Universiteit Delft





# Advances and assessment of the Ring of Fire concept for on-site cycling aerodynamics

by

**Luigi de Martino Norante**

in partial fulfillment of the requirements for the degree of

**Master of Science**  
in Aerospace Engineering  
Aerodynamics Profile

at the Delft University of Technology,  
to be defended publicly on Thursday June 7, 2018 at 9:00 AM.

Student number:	4449533	
Project duration:	August 23, 2017 – June 7, 2018	
Supervisor:	Dr. A. Sciacchitano	
Thesis committee:	Prof. dr. F. Scarano	chairman
	Prof. dr. ir. J. Westerweel	external member
	Ir. W. Terra	daily supervisor
	Ir. A.M.C.M.G. Spoelstra	PhD candidate

An electronic version of this thesis is available at <http://repository.tudelft.nl/>.



# Acknowledgements

In cycling, drag force can account up to 90% of the total resistive force the athlete has to overcome. Because of that, road cycling strategies are strongly affected by aerodynamics and by the benefit of drafting. As a consequence, although counter-intuitive for the people not following this sport, road cycling is a team sport and not an individual one. Similarly, a master thesis project is a grand tour that requires the contribution of all the members of the team in order to achieve the final objectives: firstly, completing the grand tour; secondly, winning.

In March 2017 *Andrea*, the sportive director of a successful team, offered me an exciting opportunity as GC (General Classification) rider for the next grand tour: a Ring of Fire MSc Thesis Project. During the tour he has been supportive and accurate, suggesting me the best training techniques and listening to my doubts with a sincere interest in my physical shape for the upcoming mountains. His contribution has been accompanied by the constant interest of *Fulvio*, our funding title-sponsor, in my training progress. Within the team, a GC rider relies the most on two fundamental people for his own preparation: his lieutenant and his masseur. The first, *Wouter*, followed me along the entire grand tour, occasionally allowing me to stay in his slipstream and suggesting me the appropriate moments to gain time on the opponents. The second, *Alexander*, has perfectly played his role during the grand tour, as the masseur is the first person the cyclist confides in, sharing his own difficulties and ambitions.

As a part of this team, I could have not finished the grand tour without the rouleurs, who permitted not to lose valuable time in the longest stages: *Dennis, Colette, Henk-Jan, Peter, Frits* and *Nico*. Young riders as *Winter* and *Nathan* provided a valuable contribution as well. Furthermore, the finisseurs enriched the path for the final victory, given that they contributed with brilliant and successful breakaways but decided as well to put on a secondary level their own ambition to be of help for the team's captain: *Simo, Edo, Dani, Mitro, Peppe C.A., Sumedh, Blanca, Ale P.* A special thanks to my photographer and interviewer for the local newspaper of Delft, *Mario*, who shared with me the dream to make this tour publicly known. Last, but not least, nothing would have been possible without the only real cyclist among all of us: *Robert*, brave enough to let himself being aerodynamically investigated in this report.

Aside of the team, as a captain I have been supported during all the stages by four fan clubs, who followed my stages directly on the road, as the *Basement fan club* and *Karting and More*, or on TV, as my second family from *Terzo Piano Valentino* and the *Barletta fan club*, led by *Fede*. Special mention to *Hilbert*, who has kindly shared the role as a personal chef of the team's captain.

I have not enough words to express gratitude to the five people who have made me the person and the athlete I am, always giving me the happiest moments and the strongest support since my early local races as an amateur up to my promotion in professional cycling: my father *Raffaele*, my mother *Stella* and my brothers *Stefano, Fabio* e *Nicola*.

Although cycling is a team sport, my first fan has always struggled to understand that. Nevertheless, her different opinion on the subject is supported by clear evidence. In fact, she has constantly remembered me that when you are climbing the Zoncolan, it does not matter how many team members are with you. It only matters how strong your legs are and how far you can dream to go. In those moments I could reach the top of the climb thanks to her, my fiancée *Chiara*.

Today, the final stage of the tour consists of this joyful individual time-trial: I am going to look at cheerful faces of my fans and to try to stop the clock as early as I can.

*Luigi de Martino Norante*  
*Delft, 7<sup>th</sup> July 2018*



# Abstract

Aerodynamics investigations in speed sports as cycling are of paramount importance to reduce race times. They generally consist of measurements of aerodynamic loads through wind tunnel experiments or on-site techniques. These experimental tools are often used to validate computational fluid dynamics studies, which help correlating aerodynamic loads with flow phenomena. Lately, a new technique has emerged, known as the Ring of Fire ([Sciacchitano et al., 2015](#)). The Ring of Fire is a drag measurement technique applied on-site for transiting athletes. It is based on the application of integral momentum conservation through Large-Scale PIV measurements, hence it provides flow field data as well as aerodynamic loads. [Spoelstra \(2017\)](#) applied for the first time the Ring of Fire concept at full-scale, by using a High Speed Stereo-PIV system to capture the wake of a transiting cyclist in an outdoor environment.

This project deals with the implementation and the advances of the Ring of Fire concept. The research is initiated by the hypothesis that an indoor implementation of the Ring of Fire with a Low Speed PIV system can provide a more accurate drag determination than in the case of [Spoelstra \(2017\)](#). In addition, it aims at improving the system by: conceiving a new seeding container; implementing a synchronisation system between PIV image acquisition and the cyclist's passage; evaluating the performance of a cyclist's speed measurement by a magnetic sensor.

An experiment is conducted on an amateur cyclist in a sports hall. The cyclist is tested in pedalling and non-pedalling conditions in time-trial and upright postures at a torso-based  $Re_T = 2 \cdot 10^5$ . The pedalling conditions are tested with a reduced frequency  $k$  equal to 0.12, representative of racing conditions for professional time-trial cyclists. Ensemble-averaged flow fields support the discussion on the variation of aerodynamic loads with the cyclist posture and highlight the presence of large-scale structures in the cyclist's wake, as in [Spoelstra \(2017\)](#); [Crouch et al. \(2014, 2016a\)](#).

The mean cyclist's drag area and drag coefficient fall within the values of the relevant past investigations. The standard deviation of the drag area over multiple passages is between 4% to 10% of the mean drag area. Fluctuations introduced with a pedalling motion do not play a relevant role in the drag area standard deviation. Twenty to thirty passages provide a mean drag area with an uncertainty below 2% at a 95% confidence level. Twenty passages are performed in a time-frame of thirty minutes. The system is capable of measuring drag differences of the order of 6%, as between a symmetric and asymmetric leg posture.

The performances of the Low-Speed PIV system are characterised by a  $DVR = 250$  and  $DSR = 25$ . The  $DSR$  is primarily limited by the lack of uniformity in the seeding distribution among the different passages and within the same field of view.

With the contribution of this research, the Ring of Fire becomes a more mature technique for application in speed sports aerodynamics, even at an industrial level. With further improvements in the uniformity of seeding density and in the synchronisation between cyclist's passage and image acquisition the technique can reach an accuracy level that allows for a full exploitation of the concept. To a broader extent, this would include investigations on group of athletes, aerodynamics on curvilinear paths and objects with unsteady speed.



# Contents

<b>List of Figures</b>	<b>ix</b>
<b>List of Tables</b>	<b>xiii</b>
<b>List of Symbols</b>	<b>xv</b>
<b>1 Introduction and Literature Study</b>	<b>1</b>
1.1 Background . . . . .	1
1.2 Cycling aerodynamics . . . . .	3
1.2.1 Experimental research. . . . .	3
1.2.2 The cyclist wake topology . . . . .	5
1.2.3 Numerical research . . . . .	8
1.3 Drag measurement techniques in experimental studies . . . . .	9
1.3.1 Wind tunnel experiments . . . . .	9
1.3.2 On-site measurement techniques . . . . .	10
1.3.3 The Ring of Fire. . . . .	11
1.4 Project goal and associated research questions . . . . .	12
<b>2 Theoretical principles</b>	<b>17</b>
2.1 Particle Image Velocimetry in Aerodynamics. . . . .	18
2.1.1 Stereoscopic PIV . . . . .	19
2.1.2 Large Scale PIV . . . . .	21
2.1.3 Low-speed and High-speed PIV . . . . .	22
2.2 Control volume approach . . . . .	23
2.2.1 Wind tunnel model reference system . . . . .	23
2.2.2 Ring of Fire reference system: application on transiting objects . . . . .	25
<b>3 Experimental Setup and Procedures</b>	<b>29</b>
3.1 The Indoor Facility and the Tunnel . . . . .	30
3.2 The Tested Object . . . . .	31
3.3 PIV Setup . . . . .	33
3.4 Wake synchronisation . . . . .	35
3.5 Cyclist Velocity measurement . . . . .	36
3.6 Testing procedure . . . . .	38
<b>4 Data analysis and Reduction techniques</b>	<b>43</b>
4.1 Streamwise relocation . . . . .	44
4.2 Spanwise relocation . . . . .	45
4.3 Cyclist's speed measurement. . . . .	47
4.4 Determination of each wake position and crank angle. . . . .	48
4.5 PIV processing . . . . .	49
4.6 Test outlier selection. . . . .	52
4.7 Upstream plane choice . . . . .	54
4.8 Frontal area evaluation . . . . .	56
4.9 Drag area and flow field variables . . . . .	56
<b>5 Results and Discussion</b>	<b>61</b>
5.1 Cyclist's speed . . . . .	62
5.2 Flow fields . . . . .	62
5.2.1 Time-trial static configurations . . . . .	62
5.2.2 Time-Trial Comparison between Static and Dynamic . . . . .	70
5.2.3 Dynamic Comparison between Time-Trial and Upright . . . . .	73

---

5.3	Drag analysis . . . . .	75
5.3.1	Mean Drag area: Static cases . . . . .	76
5.3.2	Mean Drag area: Dynamic cases. . . . .	77
5.3.3	Drag Summary and uncertainty analysis . . . . .	78
5.4	Low-Speed ROF and High-Speed ROF . . . . .	81
<b>6</b>	<b>Conclusions and Recommendations</b>	<b>87</b>
6.1	Conclusions . . . . .	87
6.2	Recommendations . . . . .	88
6.2.1	Further works. . . . .	89
	<b>Bibliography</b>	<b>91</b>
<b>A</b>	<b>Determination of the synchronisation system delay</b>	<b>97</b>
<b>B</b>	<b>On the influence of the environment spatial variation</b>	<b>101</b>

# List of Figures

1.2	Force diagram on a cyclist; only components in the proceeding direction, forces not in scale . . . . .	2
1.3	The main four positions: traditional upright (a), drops (b), hill-descent (c), time-trial (d), reproduced from Lukes <i>et al.</i> (2005) . . . . .	3
1.4	Evolution of bicycle frames of the Olympic gold medal athletes in the individual pursuit, reproduced by Crouch <i>et al.</i> (2017) . . . . .	5
1.5	Cyclist wake flow topology, reproduced from Crouch <i>et al.</i> (2014) . . . . .	6
1.6	Wind tunnel balance measurements in time-trial posture for different reduced frequencies, reproduced from Crouch <i>et al.</i> (2016a); crank angle here indicated with $\theta$ . . . . .	6
1.7	Cyclist wake structures for $k = 0.115$ , isosurface swirling strength criterion, reproduced from Crouch <i>et al.</i> (2016a); crank angle here indicated with $\theta$ . . . . .	7
1.8	Cyclist structures in asymmetric static condition, isosurface of streamwise vorticity $\omega_x = \pm 100s^{-1}$ and $\omega_x$ -contour 10mm from centreline, reproduced from Jux (2017) . . . . .	7
1.9	Drag area relative error between CFD and wind tunnel, reproduced from Defraeye <i>et al.</i> (2010a) . . . . .	8
1.10	Symmetric (left) and Asymmetric (right) time-trial static streamwise vorticity 0.6m far from the cyclist back. First figure refers to experimental results of Crouch <i>et al.</i> (2012a), second and third to SST- $k-\omega$ and SAS-SST results respectively, reproduced from Griffith <i>et al.</i> (2014) . . . . .	8
1.11	Wind tunnel Tomo-PIV measurement in asymmetric static time-trial posture, reproduced from Terra <i>et al.</i> (2016) . . . . .	10
1.12	Schematic of the Ring of Fire concept as introduced by Sciacchitano <i>et al.</i> (2015) . . . . .	11
1.13	Ring of Fire setup of Spoelstra (2017) . . . . .	12
2.1	Working principle and setup of Planar PIV, reproduced from Giaquinta (2018) . . . . .	18
2.2	Projection error on 2C2D-PIV . . . . .	20
2.3	Control volume approach in the wind tunnel reference frame . . . . .	23
2.4	Control volume approach in the Ring of Fire: upstream flow measured at $t_i$ , downstream flow at $t_o$ . . . . .	25
3.1	Setup overview . . . . .	31
3.2	2017 Team Sunweb Bike . . . . .	32
3.3	Cyclist configurations silhouettes - Front view . . . . .	32
3.4	Cyclist configurations silhouettes - Side view . . . . .	33
3.5	Imperx Bobcat IGV-B1610 . . . . .	33
3.6	Trigger modes comparison: two sample tests for each mode . . . . .	36
3.7	HS camera reconstructed cyclist image . . . . .	37
3.8	Magnetic speed sensor and magnets on the rear wheel . . . . .	37
3.9	Particle density and light intensity comparison . . . . .	38
3.10	Calibration Plate and origin . . . . .	39
3.11	Crank angle - streamwise position correspondence for all the tests; fixed laser plane position . . . . .	39
4.1	Same Image number 12 after reception of external trigger; synchronisation mode 2; Time-Trial Dynamic configuration . . . . .	44
4.2	Average near wake normalised $0.98V_z$ - Effect of streamwise relocation . . . . .	45
4.3	$\bar{\omega} = -4.5Hz$ contour; right foot detail; blue: not relocated; red: spanwise relocated . . . . .	45
4.4	Lack of repeatability in spanwise position; Time-Trial Asymmetric Static configuration . . . . .	46
4.5	Spanwise relocation on corrected image; zoomed rear wheel . . . . .	47

4.6	Sample start and end frames . . . . .	47
4.7	Velocity history of a typical static test run . . . . .	48
4.8	Image preprocessing effect on a $64 \times 64$ px window . . . . .	50
4.9	Percentile SNR trend with choice of normalisation filter window - logarithmic scaled axes . . . . .	51
4.10	Planes average of 5 percentile SNR for each test run in symmetric static configuration; uncertainty bars indicate minimum and maximum . . . . .	53
4.11	Seeding density comparison between a typical $ppp$ level and an outlier - Raw images . . . . .	53
4.12	Potential flow for a cylinder $C_p - z/L$ with $L = 1.684\text{m}$ . . . . .	55
4.13	$C_d A$ momentum deficit variation with the choice of the upstream plane - asymmetric static configuration . . . . .	55
4.14	Upstream flow field for a single typical test run; axes ticks every 0.1 m . . . . .	55
4.15	Time-Trial Asymmetric Cyclist's frontal area . . . . .	56
4.16	$\overline{C_d A}$ momentum term variation with the method adopted to measure the cyclist's speed - time-trial dynamic configuration . . . . .	57
5.1	Wake mean flow in Time-Trial Static Asymmetric configuration . . . . .	63
5.2	Wake growth for Time-Trial Static Configurations . . . . .	64
5.3	Wake growth rate as a function of the chosen $\overline{V_z}$ contour level . . . . .	64
5.4	Near wake at $z/\sqrt{A_c} \approx 1$ in Time-Trial Static configurations: Asymmetric (left), Symmetric (right) . . . . .	66
5.5	Near wake at $z/\sqrt{A_c} \approx 1$ in Time-Trial Static configurations: Asymmetric (left), Symmetric (right) . . . . .	68
5.6	Near wake at $z/\sqrt{A_c} \approx 1$ in Time-Trial Static configurations: Asymmetric (top), Symmetric (bottom) . . . . .	69
5.7	$\overline{\omega}[s^{-1}]$ ; Time-Trial Static at $\varphi = 0^\circ$ ; colour scale as in Fig.5.6; reproduced from Crouch <i>et al.</i> (2014) . . . . .	70
5.8	Near wake at $z/\sqrt{A_c} \approx 1$ in Time-Trial Asymmetric configurations: Static (left), Dynamic (right) . . . . .	71
5.9	Wake at $z/\sqrt{A_c} \approx 5$ in Time-Trial Symmetric configurations . . . . .	72
5.10	Near wake at $z/\sqrt{A_c} \approx 1$ in Time-Trial Dynamic configuration . . . . .	73
5.11	Near wake at $z/\sqrt{A_c} \approx 1$ in Dynamic Asymmetric configurations: Time-Trial (left), Upright (right) . . . . .	74
5.12	Vorticity field in Upright configuration, reproduced and rescaled from Spoelstra (2017); cyclist silhouette unreal . . . . .	75
5.13	Streamwise variation of the drag area for Static configurations . . . . .	76
5.14	Streamwise variation of the mean pressure term of the drag area for Static configurations . . . . .	76
5.15	Streamwise variation of the drag area for Dynamic configurations . . . . .	77
5.16	Streamwise variation of the mean pressure term of the drag area for Dynamic configurations . . . . .	78
5.17	Overall drag area comparison . . . . .	79
5.18	Standard deviation in the momentum term of the drag area across the runs for each downstream plane and relation to the minimum five percentile SNR in the PIV measurement . . . . .	80
5.19	Near wake at $z/\sqrt{A_c} \approx 1$ in Time-Trial configuration: Low-Speed ROF (left), High-Speed ROF (right); right figures reproduced from Spoelstra (2017) . . . . .	82
5.20	Momentum term of drag area for five instantaneous randomly sampled runs; Time-Trial Dynamic . . . . .	84
5.21	Standard deviation of drag area across the runs in the High-Speed ROF (Spoelstra, 2017) . . . . .	85
A.2	Measurement procedure to quantify the synchronisation system delay . . . . .	98
A.3	Frequency distribution of the synchronisation system delay . . . . .	98
A.4	Streamwise variation of the imprecision in attributing the wake position relative to the cyclist . . . . .	99
B.1	Streamwise mean momentum term of $C_d A$ for dynamic upright configuration; effect of constant inflow . . . . .	102

---

B.2 Streamwise mean momentum term of $C_d A$ for dynamic upright configuration; effect of null inflow . . . . .	102
---	-----



# List of Tables

1.1	Summary of some references' results for time-trial and upright postures . . . . .	4
3.1	Equipment and setup parameters . . . . .	34
3.2	Single test passage - typical timeline . . . . .	40
4.1	Stereo cross correlation processing parameters . . . . .	51
5.1	Cyclist speed statistics for the first downstream plane . . . . .	62
5.2	Main and secondary structures in the two static configurations . . . . .	67
5.3	Configurations drag summary . . . . .	79



# List of Symbols

## Abbreviations

2D2C	Two-dimensions Two-Components
2D3C	Two-dimensions Three-Components
CAD	Computer-Aided Design
CCD	Charge-Coupled Device
CFD	Computational Fluid Dynamics
CMOS	(complementary metal-oxide-semiconductor)
<i>CS</i>	Control Surfaces
<i>CV</i>	Control Volume
<i>DSR</i>	Dynamic Spatial Range
<i>DVR</i>	Dynamic Velocity Range
FOV	Field of view
<i>GR</i>	Gear ratio
HFSB	Helium-Filled Soap Bubbles
IW	Interrogation window
LES	Large Eddy Simulation
PIV	Particle Image Velocimetry
<i>ppp</i>	particle per pixel
PTU	Programmable Timing Unit
PTV	Particle Tracking Velocimetry
RANS	Reynolds-Averaged Navier-Stokes equations
ROF	Ring of Fire
SAS	Scale-Adaptive Simulation
SNR	Signal-to-noise ratio
SNR <sub>5</sub>	Fifth percentile of SNR
SST	Shear Stress Transport
Std	Standard deviation

## Latin symbols

$A_c$	Cyclist's frontal area
$C_d$	Drag coefficient
$C_d A$	Drag area
$C_d A_{mom}$	Momentum term of drag area
$C_d A_p$	Pressure term of drag area
$C_d A_{u_i}$	Drag area contribution due to $u_i$
$C_p$	Pressure coefficient

$conv_f$	Convection factor
$D, D$	Drag force
$D_a$	Lens aperture
$d_o$	Object distance
$f$	Frequency
$f$	Focal length
$F_g$	Gravity force component along the streamwise direction
$F_r$	Rolling resistance
$I_o$	Pulse energy
$k$	Reduced frequency
$M$	Magnification factor
$n_z$	Component of normal vector along $z$
$p_\infty$	Ambient pressure
$p$	Static pressure
$r$	Crank length
$Re_T$	Torso-based Reynolds number
$T$	Cyclist's thrust force
$T$	Torso length
$t_l$	Time instant at which the back wheel of the bike touches the laser
$U_c$	Cyclist's speed
$u$	Velocity component along $z$
$u_i$	$u$ measured at upstream plane (ROF)
$u_o$	$u$ measured at downstream plane (ROF)
$u_w$	$u$ in the wake of the cyclist (wind tunnel)
$u_\infty$	free stream $u$
$u'$	Fluctuation of $u$
$V_z$	Normalised streamwise velocity deficit
$V_{xy}$	Normalised in-plane velocity
$v_x$	Velocity component along $x$
$v_y$	Velocity component along $y$

### Greek symbols

$\Delta t$	Pulse separation
$\Delta z$	Laser thickness
$\lambda_{ci}$	Imaginary part of complex eigenvalue of the velocity gradient tensor
$\rho$	Air density
$\sigma_{C_d A}$	Standard deviation of drag area
$\sigma_{C_d A_{mom}}$	Standard deviation of momentum term of drag area
$\bar{\tau}$	Viscous stress tensor
$\varphi$	Crank angle
$\omega$	Vorticity



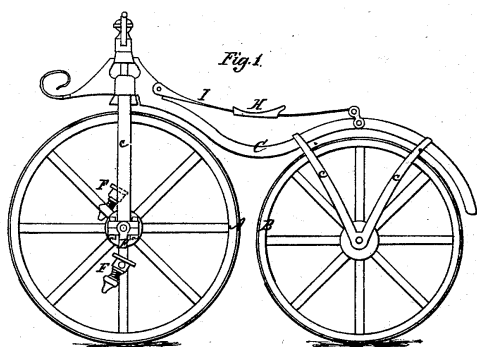


# 1

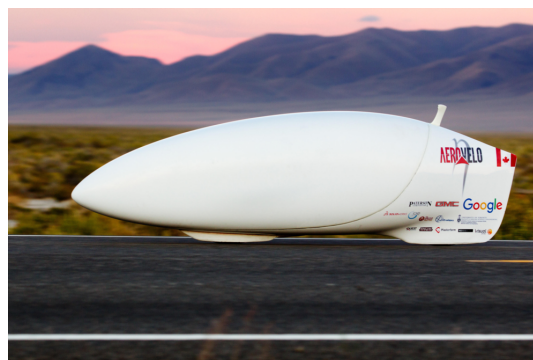
## Introduction and Literature Study

### 1.1. Background

In 1866 the world witnessed several war events ending: in the USA the bloody civil war was followed by the Civil Right Acts, stating American citizens equality in front of the law, while the Third War of Independence brought the Kingdom of Italy to obtain Venice from the Austrians after Treaty of Vienna. Moreover, relevant world personalities left us as the genius founder of elliptic non-Euclidean geometry Bernhard Riemann as well as the Italian prime minister Massimo D'Azeglio, the patriotic mythiciser of the national hero Ettore Fieramosca. At the same time, in Connecticut, a Frenchman inventor was set to make a giant leap for human transportation: on 20<sup>th</sup> November the first patented bicycle was issued and publicly presented (Lallement, 1866). Despite some early predecessors, the Pierre Lallement's invention (Fig.1.1a) is acknowledged as the first example of what is currently considered as a bike, given the human power being provided through the front hub crank pedals. Along the years, the bike has experienced little evolution of its basic concept, while it has spread around the world. To a certain extent, the advent of motorisation has tried to confine the bike functions given its limitation in maximum achievable speed. However, progress in understanding the bike physics has allowed to reach a maximum speed equal to 144.17 km/h on flat surface, by the AeroVelo team (Fig.1.1b).



(a) Drawing of Lallement's bike (Lallement, 1866)



(b) ETA bike ( $v_{max} = 144.17$  km/h) (AeroVelo, 2016)

Comparison between Fig.1.1a and Fig.1.1b could pose the reader to wonder whether the bike shape and the relative cyclist posture has any sort of effect on the bicycle maximum speed. The answer, as it will be highlighted throughout this introduction, is yes.

In cycling, the rider produces a power output transferred to the rear tyre through a chain system. For a certain angular speed, this power corresponds to a wheel torque. Because of the torque, local friction forces between tyres and ground are generated and permit movement. Such a movement is possible

if the cyclist produces a thrust force  $T$  sufficient to overcome three main forces in the proceeding direction: the aerodynamic drag  $D$ , the rolling resistance  $F_r$  and the gravity component  $F_g$  tangential to the ground (Atkinson *et al.*, 2003), disregarding frictional chain and bearing losses. In Fig.1.2, a schematic of the three forces is presented. In uphill conditions the gravity force component is the main contributor to the total resistive force; in downhill, the gravity force sums up to the cyclist thrust so that the propulsive force can overcome the resistive one. While gravity and rolling resistance are mostly independent of velocity (Chowdury and Alam, 2012), the drag force depends on the square of the velocity and can account up to 90% of the total resistive force (Kyle and Burke, 1984) in professional cycling. With a small road gradient of 0.3%, 56% (uphill) to 96% (downhill) of the cyclist power is used to overcome drag non-conservative work per time (Martin *et al.*, 1998).

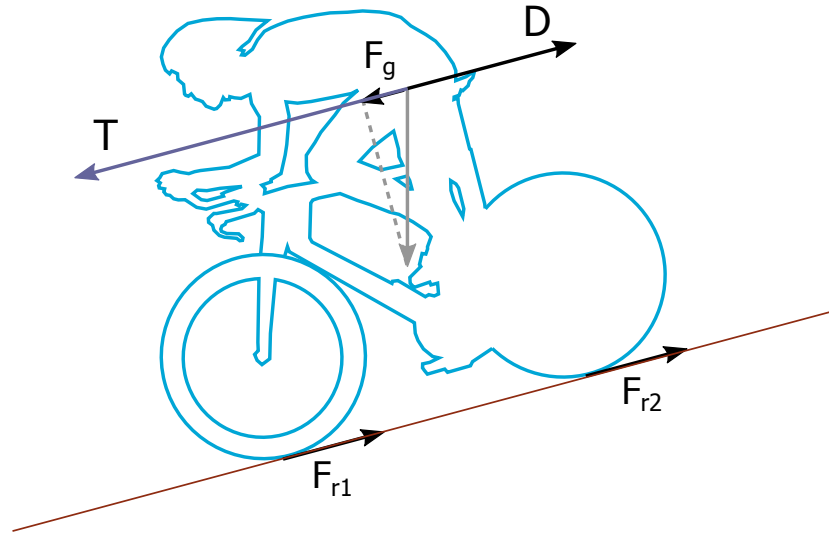


Figure 1.2: Force diagram on a cyclist; only components in the proceeding direction, forces not in scale

In the cyclist's reference frame, the aerodynamic drag is the streamwise component of the aerodynamic force exerted by the surrounding fluid on the object overall surface. As it is a surface force due to fluid pressure and shear stress distribution (Anderson, 2011), dimensional analysis permits to write it as:

$$D = \frac{1}{2} \rho C_d A U_c^2 \quad (1.1)$$

with  $\rho$  the fluid density,  $C_d$  the dimensionless drag coefficient,  $A$  the object reference area,  $U_c$  the tested object velocity, so the cyclist velocity. For the cyclist, the reference area corresponds to the frontal area. As both  $C_d$  and  $A$  depend on the body shape, it is common to analyse the cyclist aerodynamic performance through the concept of drag area  $C_d A$ . Overall cyclist drag areas are of the order of 0.2 to 0.4  $m^2$ , depending on the cyclist posture and the drag measurement technique. To give an idea of the drag area influence on the cyclist performance, consider that a reduction of 0.01  $m^2$  in drag area corresponds to a reduction in race time of one second per kilometre (Gibertini and Grassi, 2008).

Because of the role of the drag in the generation of non-conservative work harming the power expenses of the cyclist, professional cycling teams have always been strongly interested in improving the athletes' performance through drag reduction. Their research has been accompanied by exploitation of experimental techniques and computational fluid dynamics (CFD) simulations to evaluate the drag of the cyclist-bike combination. While the first could be regarded as closer to the reality, on the other hand the second provides extensive data over the entire cyclist. Understandably, both simulation tools and experimental techniques accuracy and precision are matters of concern for the engineers, given the necessity to compare innovative solutions to reduce drag in comparison to an established baseline. As discussed in section 1.2.3, CFD simulations present inaccuracy of the order between 10% to 20% with respect to experimentally determined loads (Crouch *et al.*, 2017). Therefore, Debraux *et al.* (2011) and Crouch *et al.* (2017) clearly indicate that the general trend in cycling aerodynamics is to evaluate

the drag based on force measurements in wind tunnel facilities or through on-site experimental techniques. Nevertheless, both wind tunnel force measurements and on-site measurements miss the link with the aerodynamic phenomena causing drag variations. As a consequence, the amount of research on cycling aerodynamics in the past decades is clearly not proportional to the reached understanding. Although these tools have been useful to evaluate cyclist's drag or drag area and to compare different configurations among themselves, the aerodynamics motivation supporting certain results is lacking and the progress is slowed down by blind optimisation. Already more than ten years ago, [Lukes et al. \(2005\)](#) underlined the problem and indicated in CFD the future solution to link flow phenomena and drag force.

In the most recent years, the situation has dramatically changed. Two concurrent works from Monash University and Technische Universiteit Delft have strongly contributed in generating flow phenomena understanding through experimental aerodynamics, with the former focussing on the wake flow topology characterisation and the latter on improving the experimental techniques to reach deeper awareness. The Delft University has emerged as the front runner in establishing the link among drag measurements and flow phenomena even in the most real case scenario as on the road.

## 1.2. Cycling aerodynamics

### 1.2.1. Experimental research

The first scientific investigation on cycling aerodynamics dates as late as 1956 with the work of [Nonweiler \(1956\)](#). A closed test section wind tunnel experiment was carried out on three local amateurs through a sophisticated suspended wiring system allowing for force balance measurements. In this early work the drag dependency to the square of the velocity was underlined, highlighting a missing drag crisis Reynolds number range typical of simpler bluff bodies. Furthermore, given the frontal area variation of the cyclist with the posture and legs position, the author stressed the benefit of addressing the aerodynamic performance through the concept of drag area.

On the experimental side, challenges still common to current wind tunnel experiments as the errors introduced in wrong yaw alignment and the difficulty in replicating exact positions were addressed. Experiments repeatability is a concern that characterises the whole research in cycling. In fact, as the cyclist is not an idealised model used as a reference among the several researchers, absolute value results in drag coefficient or drag area are often in disagreement among themselves.

Differently from later works, [Nonweiler \(1956\)](#) recorded a slight variation with respect to cyclist posture. In fact, the work from [Kyle and Burke \(1984\)](#), considered the "most in-depth study of the time" in the cycling aerodynamics review of [Lukes et al. \(2005, p.60\)](#), underlined a hierarchical approach in evaluating factors contributing to the drag, posing the cyclist posture at the first place.

Several studies have tried to summarise the differences among the cyclist postures and their aerodynamic effects. In general, the earlier studies made an effort in reducing the cyclist frontal area so that the more streamlined was the cyclist, the lowest was the drag area. Therefore, from the traditional upright position (a in Fig.1.3), in 70s cyclists started adopting drops position (b) on flat surfaces and (c) hill-descent positions downhill. In 1989, after Greg LeMond's victory at the Tour de France, [Kyle \(1989\)](#) investigated the adoption of tri-bars given their drag reduction: these elongated bars allow the cyclist to have the torso aligned with the ground and assume the time-trial position (d in Fig.1.3). [Kyle and Burke \(1984\)](#) found the drops position to have 19% less drag area than the traditional position, while [Kyle \(1989\)](#) underlined a further 15% reduction from the drops position with the time-trial posture. In both cases, balance measurements were performed in a wind tunnel with stationary ground.

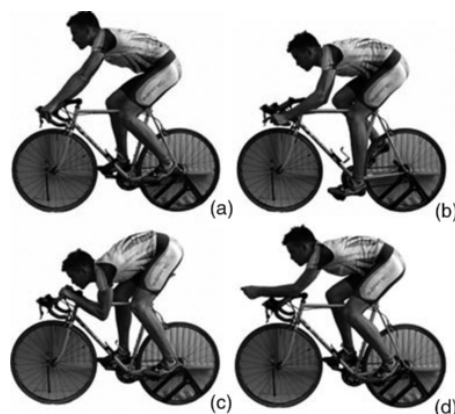


Figure 1.3: The main four positions: traditional upright (a), drops (b), hill-descent (c), time-trial (d), reproduced from [Lukes et al. \(2005\)](#)

Further studies confirm the relevance of the posture on the cyclist drag area. [Grappe et al. \(1997\)](#) assessed twelve cyclists' drag area in an open velodrome by a linear regression analysis based on a powermeter. The time-trial drag area was found 12% lower than in upright position. [Gibertini and Grassi \(2008\)](#) performed a force balance wind tunnel experiment comparing the time trial position and variations of the upright positions for two cyclists. The time-trial drag area was found between 21% and 25% lower than the brake hoods one, i.e. the traditional upright position. Moreover, [Gibertini and Grassi \(2008\)](#) found that the upright position with the hands on the stem had 5% more drag than the traditional brake hoods one, despite the reduction in frontal area.

[Defraeye et al. \(2010b\)](#) conducted a similar test and found the time-trial position to have 20% less drag area than the upright stem position. The authors tried to separate the drag contribution of the cyclist from the bike, with the former accounting for 70% of the total. [Barry et al. \(2015\)](#) performed wind tunnel balance measurements on a pedalling cyclist in nine different positions and distinguished the contribution of the frontal area from the drag coefficient on the drag area. They underlined the effect of small details in the posture, as lowering the head or closing the elbows in time-trial position, shrugging in the upright one. In addition, the major contribution in drag area for the brake hoods position was attributed to the cyclist frontal area, as the drag coefficient was noticed lower than the time-trial one. Wake surveys were performed through dynamic pressure probes: variations around 7% of the drag coefficient among the nine postures is linked to the spatial distribution of streamwise velocity deficit in the cyclist wake as well as different velocity levels.

A summary of some references' results cited in this literature review is shown in Tab.1.1 for both the time-trial and upright postures.

Table 1.1: Summary of some references' results for time-trial and upright postures

Reference	Time-Trial 		Upright 		Condition	Measurement technique
	$C_d$	$C_dA$ [m <sup>2</sup> ]	$C_d$	$C_dA$ [m <sup>2</sup> ]		
Capelli et al. (1993)	0.652	0.256	-	-	Dynamic	On-site - towing method
Grappe et al. (1997)	-	0.262	-	0.299	Dynamic	On-site - powermeter linear regression
Martin et al. (1998)	-	0.269	-	-	Dynamic	Wind tunnel - force balance
Candau et al. (1999)	-	0.262	-	-	Dynamic	On-site - deceleration method
Gibertini and Grassi (2008)	0.792	0.235	0.76	0.304	Dynamic	Wind tunnel - force balance
Defraeye et al. (2010b)	-	0.211	-	0.27	Static	Wind tunnel - force balance
Chowdury and Alam (2012)	0.86	0.327	1.04	0.427	Static	Wind tunnel - force balance
Crouch et al. (2014)	0.52	0.216	-	-	Static	Wind tunnel - force balance
Barry et al. (2015)	0.734	0.283	0.694	0.343	Dynamic	Wind tunnel - force balance
Terra et al. (2016)	-	0.243	-	-	Static	Wind tunnel - force balance
Terra et al. (2016)	-	0.244	-	-	Static	Wind tunnel - control volume (Tomo-PIV)
Crouch et al. (2017)	-	0.24	-	-	Static	Wind tunnel - force balance
Crouch et al. (2017)	-	0.242	-	-	Dynamic	Wind tunnel - force balance
Crouch et al. (2017)	-	0.236	-	-	Dynamic	Wind tunnel - control volume ( $p_{tot}$ probes)
Shah (2017)	-	0.235-0.243	-	-	Static	Wind tunnel - force balance
Shah (2017)	-	0.231-0.251	-	-	Static	Wind tunnel - control volume (4D PTV)
Spoelstra (2017)	-	0.227	-	0.303	Dynamic	Ring of Fire (Stereo TR-PIV)

Although the mentioned authors have tried to separate the contribution of the bike from the one of the cyclist, [Gibertini and Grassi \(2008\)](#) stressed their strong interrelation, given the flow interactions. After the cyclist posture, the second main factor in affecting the overall drag area is the bike geometry ([Kyle and Burke, 1984](#)), with the wheels being the main argument of research in the past ([Lukes et al., 2005](#); [Crouch et al., 2017](#)). [Tew and Sayers \(1999\)](#) investigated the yaw behaviour of six isolated wheel geometries in an open test section wind tunnel. It is important to underline that their results should be considered with care given the geometry isolation, even though a DC motor was used to let them rotate. [Tew and Sayers \(1999\)](#) underlined that less spokes and a smaller rim diameter can significantly reduce the drag in straight conditions, with the disc wheel reducing up to 70% of the drag. However, at small yaw angles side forces fluctuation occurs while at larger angles a spoked wheel should be preferred. [Capelli et al. \(1993\)](#) performed a comparison between the lenticular lens disc wheel with a traditional one by adopting a towing method to measure the cyclists' drag area on-site, obtaining similar conclusions.

Regarding the bike frames, Kyle (1989) is a main contributor with his investigation on different aero frames and the introduction of the tri-bars. In the early stages of the aerodynamics understanding, the bike frame design objective hinged on providing the structure for the most aerodynamic rider posture. Instead, the relevance of aerodynamically shaping the bike for cycling performance was first affirmed with the advent of the 1992 Lotus Sport bike (Hill, 1993), labelled (c) in Fig.1.4. Since 1992 the bike frame has followed the same trend behind the cyclist posture optimisation: reducing pressure drag as major contributor to the bluff-body drag. This evolution has led towards streamlining each tubular section of the frame, within the concurring major restrictions from l'Union Cycliste Internationale.

In addition to the bike frames, research for detail optimisation has influenced the cyclist's equipment as well. For a review of the historical aerodynamics optimisation of helmets and rider suits, the reader is referred to the works of Lukes *et al.* (2005) and Crouch *et al.* (2017).

For the purpose of this research, the investigation of Oggiano *et al.* (2013) is worthy to be mentioned. Drag measurements through force balances were performed on cylinders covered with various suit fabric. Drag crisis associated with varying Reynolds number is reported together with hysteresis trend for strong accelerations as for sprinters. However, the analogy of an isolated cylinder with either the torso or the leg is an open question as, to the best knowledge of the author, none has proved the presence of a Reynolds effect on the drag area of a cyclist. In fact, studies at different velocities of both Chowdury and Alam (2012) and Crouch *et al.* (2014) were performed above the critical Reynolds number for either the torso or the legs. To a certain extent, differences across the critical Reynolds number for the cyclist torso are noticeable in Crouch *et al.* (2016b), where a full-scale model wake acquired with pressure probes in a wind tunnel is compared with a 22% scaled model wake acquired by Particle Image Velocimetry in a water tunnel. The comparison is only qualitative and pertains the flow structures in the cyclist wake in both static and dynamic conditions: the authors underlined a similarity between the two results, although a drag area comparison is not reported. The relation between drag area and wake structures is drawn in the studies performed at Monash University, to which the following section is dedicated.

### 1.2.2. The cyclist wake topology

One of the earlier works of Crouch *et al.* (2012b) underlined some new insights in cycling aerodynamics: by analysing the drag area variation with the crank angle for time-trial configuration, the existence of a cyclic variation over half of the crank period was highlighted. The lower drag condition corresponds to an inclination of  $15^\circ$  down of one of the foot with respect to the horizontal crank line, while the higher drag condition to  $75^\circ$ . In the former, the cyclist's thighs are aligned; in the latter, one leg is stretched. Projected area measurements brought to discover that the variation in the drag area is primarily attributed to the variation in aerodynamics phenomena, i.e. in the drag coefficient. These observations were not only based upon wind tunnel balance measurements. In fact, smoke visualisations revealed the existence of a symmetric separation from the hips for  $\varphi = 15^\circ$ , while an asymmetric separation at  $\varphi = 75^\circ$ , with the flow strongly curving downwards in correspondence of the hip of the bent leg.

Following total pressure probes and oil flow visualisations (Crouch *et al.*, 2014) confirmed the previous results and linked the different degrees of symmetry to the existence of main vortical structures: two counter-rotating vortices coming from the hip separations and two counter-rotating vortices from

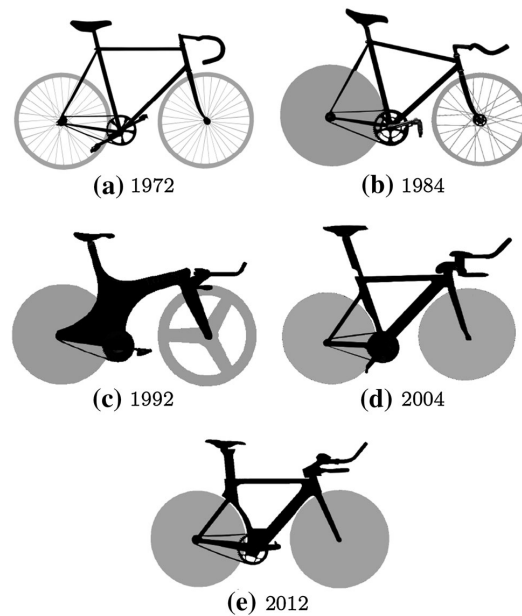
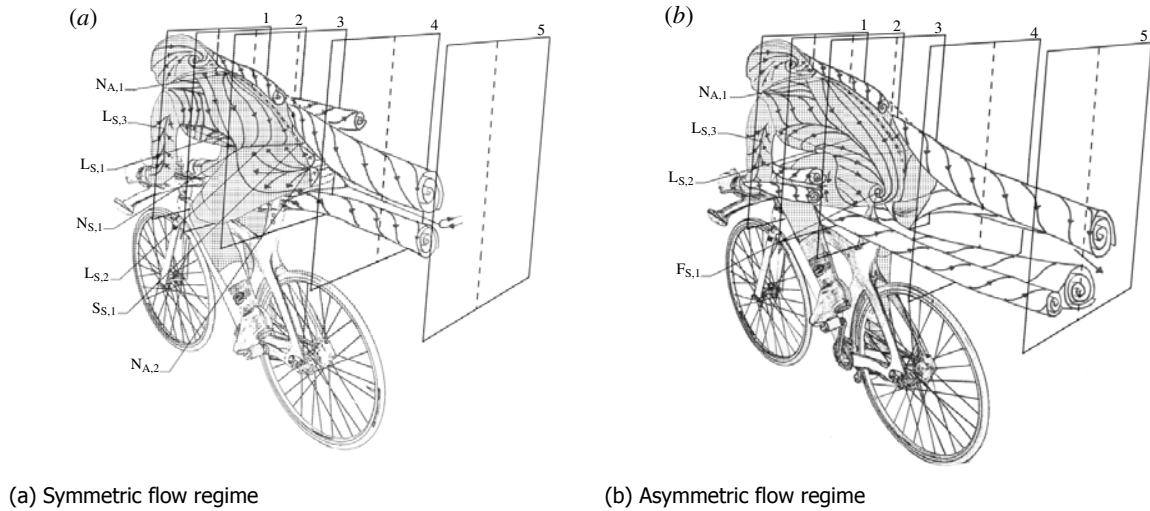


Figure 1.4: Evolution of bicycle frames of the Olympic gold medal athletes in the individual pursuit, reproduced by Crouch *et al.* (2017)

the inner thighs, co-rotating with the hip vortices. Based on that, [Crouch et al. \(2014\)](#) proposed the wake topology as in Fig.1.5. Notice that only the right part of the wake topology is shown in Fig.1.5a, as the left part is the mirrored version.

Figure 1.5: Cyclist wake flow topology, reproduced from [Crouch et al. \(2014\)](#)



(a) Symmetric flow regime

(b) Asymmetric flow regime

In the symmetric flow regime the two hips and inner thighs vortices have similar strength and symmetric position. However, at a wake one torso length far from the cyclist back (plane 5 in Fig.1.5a), the vortices strength is considerably lower than in the previous planes. This brought [Crouch et al. \(2014\)](#) to speculate about a cross-annihilation diffusive process of the vortices, with a consequent lower drag area. In the asymmetric case the balance measurements reported a drag area 20% higher than in the symmetric regime. The stretched leg hip vortex is stronger and higher than the hip and thigh vortices from the bent leg. This asymmetry is caused by the asymmetric pressure distribution and consequent skin-friction pattern on the cyclist back. Between the two hip vortices the flow strongly tends down because of the induced flow velocity, with a lateral component towards the stretched leg because of the vortices height asymmetry.

This wake topology slightly varies along the other crank angles, with a general less or more strong asymmetry governing the cyclist's wake with the crank angle less or more close to  $\varphi = 75^\circ$ . A similar reasoning occurs for its complementary angle  $\varphi = 255^\circ$ , with the hip vortices position and strength inverting, as visible in the cycle isosurface swirling strength criterion ([Zhou et al., 1999](#)) in Fig.1.7. [Crouch et al. \(2016b\)](#) did not underline substantial difference in the wake topology with one order of magnitude different Reynolds number, while [Crouch et al. \(2016a\)](#) performed a full wake survey for different reduced frequencies<sup>1</sup> and compared the results with static measurements. The authors underlined a "very little variation in the wake flow" ([Crouch et al., 2016a](#), p.136), comparing flow fields for phase-averaged different reduced fre-

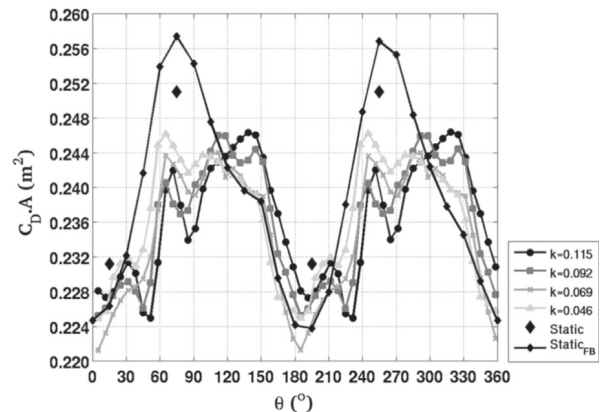


Figure 1.6: Wind tunnel balance measurements in time-trial posture for different reduced frequencies, reproduced from [Crouch et al. \(2016a\)](#); crank angle here indicated with  $\theta$

<sup>1</sup>The reduced frequency is a dimensionless parameter expressing the weight of unsteady phenomena with respect to steady phenomena. For the cyclist, it is a ratio of the leg speed around the crank and the freestream flow  $k = 2\pi r f / U_\infty$  that can be written as a sole function of the bike geometry  $k = r / (GR)$ , with  $f$  the pedalling cadence,  $r$  the crank length,  $R$  the wheel radius,  $G$  the gear ratio.

quencies and static conditions, although the judgement was a qualitative indication of the presence of similar features. On a quantitative side, despite a small effect of the reduced frequency on the drag area (Fig.1.6), the asymmetric flow regime ( $\varphi = 75^\circ$  and  $\varphi = 255^\circ$ ) showed a considerably lower drag area in dynamic conditions than in quasi-steady ones. Notice that  $k = 0.115$  is a typical reduced frequency for time-trial athletes.

Other important conclusions pertain the estimation of an average convective velocity based on the primary thigh vortex (equal to  $0.61 U_\infty$ ), the presence of a consequent  $30^\circ$  phase lag in the wake planes and the existence of secondary flow structures as the ankle-calf vortices.

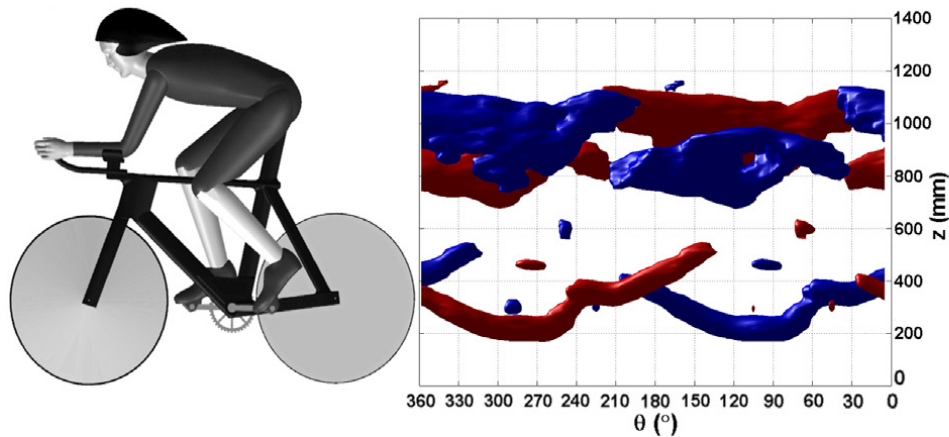


Figure 1.7: Cyclist wake structures for  $k = 0.115$ , isosurface swirling strength criterion, reproduced from [Crouch et al. \(2016a\)](#); crank angle here indicated with  $\theta$

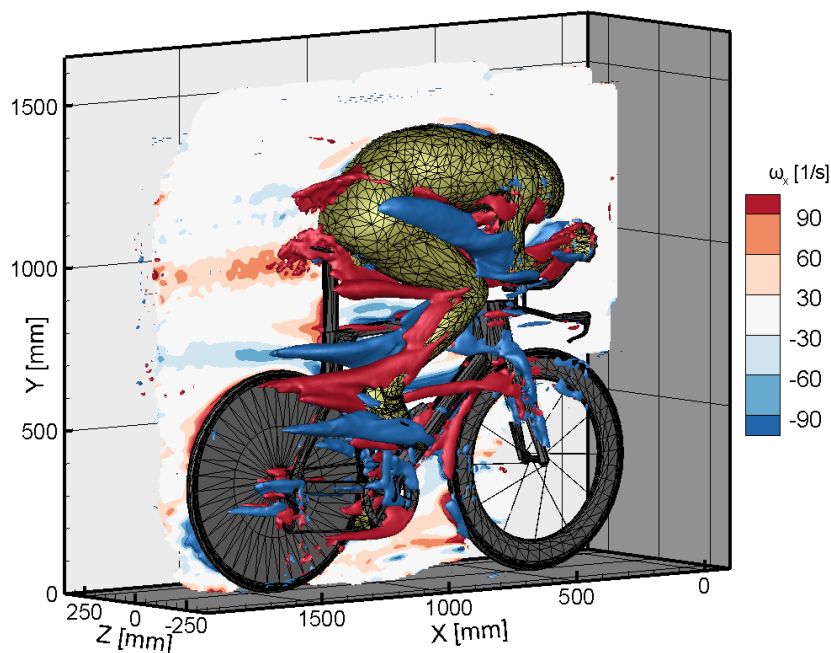


Figure 1.8: Cyclist structures in asymmetric static condition, isosurface of streamwise vorticity  $\omega_x = \pm 100s^{-1}$  and  $\omega_x$ -contour 10mm from centreline, reproduced from [Jux \(2017\)](#)

Nevertheless, reduction of the cyclist wake topology to the hip, thigh and ankle-calf vortices is unsatisfactory. In fact, the complexity of the cyclist's wake is well beyond the presence of streamwise vorticity and advancements in a thorough understanding require three-dimensional measurement techniques. In fact, as [Scarano \(2013\)](#) underlined, 3D and 4D techniques are advisable to understand the unsteadiness of the vortex dynamics as well as to distinguish coherent structures from shear layers

(Jeong and Hussain, 1995). The work of Jux (2017) is a milestone for a new era of cycling aerodynamics understanding, as the application of particle tracking through Robotic PIV allows to optically access the cyclist surrounding and obtain the full velocity tensor in a volume, even though only from a statistical perspective. For instance, isosurfaces of streamwise vorticity in Fig.1.8 show the complexity of the structures characterising the cyclist flow topology. Planar measurements might fail at detecting the peak vorticity of such structures as their planar projection is obtained.

### 1.2.3. Numerical research

The large complexity of the object and substantial inability to obtain volumetric measurements (before the work of Jux (2017) emerged) has made appealing the study of the cyclist's flow phenomena through computational fluid dynamics (CFD). When talking about numerical simulations, the first arising question regards which trade-off is the best between accuracy and simulation time in terms of turbulence-modelling. Defraeye *et al.* (2010a) compared Large-Eddy-Simulations (LES) and several turbulence modelling of Reynolds-Averaged Navier-Stokes (RANS) equations with the results of a wind tunnel test on a scaled model. The relative error for the drag area is shown in Fig.1.9. Given the bluffness of the cyclist, the standard  $k - \omega$  model is the most unsuitable for predicting drag area, while the best choices are either the standard  $k - \epsilon$ , its Shear-Stress-Transport correction, or LES. However, the latter can require between 5 to 15 times more computational cost than the former ones. These results were consistent with static pressure measurements performed over the cyclist body. Moreover, the authors underlined the negative effects of adopting wall functions for RANS and the advantage of LES over RANS in studying the unsteady flow (even though the authors did not take into account U-RANS).

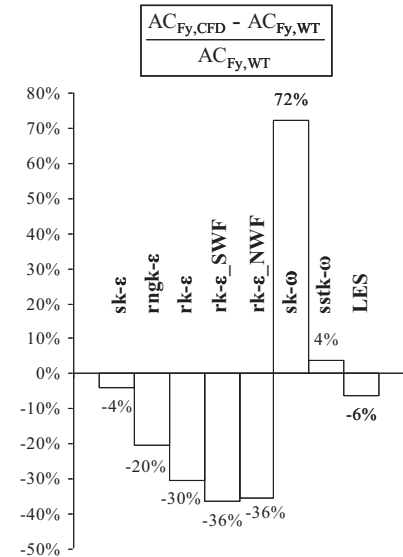


Figure 1.9: Drag area relative error between CFD and wind tunnel, reproduced from Defraeye *et al.* (2010a)

Drag area and static pressure comparisons were performed for different positions in Defraeye *et al.* (2010b), resulting in an inaccuracy of the order of 10% between CFD and wind tunnel but with the possibility of distinguishing a higher drag area for upright posture and lower for time-trial. Similarly, Roa *et al.* (2016) compared CFD results with powermeter measurements, highlighting the drag area reduction in drops position compared to the upright one. Even in this case a steady simulation was performed with a Spalart-Allmaras model and the authors underlined the oscillatory convergence typical of unsteady phenomena.

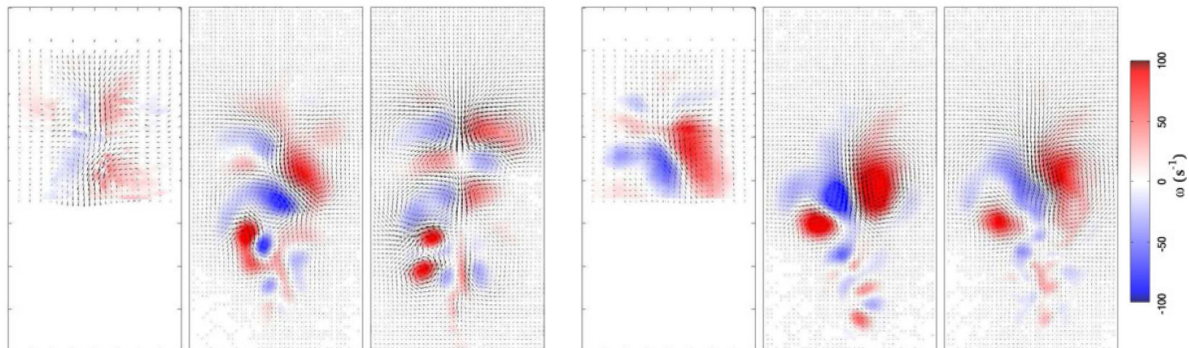


Figure 1.10: Symmetric (left) and Asymmetric (right) time-trial static streamwise vorticity 0.6m far from the cyclist back. First figure refers to experimental results of Crouch *et al.* (2012a), second and third to SST- $k - \omega$  and SAS-SST results respectively, reproduced from Griffith *et al.* (2014)

With regards to meshing, the general tendency is towards a hybrid mesh with prism-layers in the vicinity of the cyclist boundary and tetrahedra in the whole field. The difficulty in mesh refinement sometimes requires extreme approximations of the cyclist body, for instance with a set of spheres and cylinders or by removing the wheel spokes as in Griffith *et al.* (2014). In this research the authors investigate the flow fields with the crank angle variation, observing the same trends as Crouch *et al.* (2014, 2012a). Moreover, SST  $k - \omega$  simulations were accompanied by transient Scale-Adaptive Simulation (SAS)-SST studies. The latter permitted a more relevant comparison with the experimental data (first in Fig.1.10), as the flow symmetry was clearly more noticeable for  $\varphi = 15^\circ$  with the balanced hip-thighs vortices quadrupole by SAS-SST (third in Fig.1.10) than by steady SST (second in Fig.1.10). A more trustworthy comparison is noticeable as well for  $\varphi = 75^\circ$ , with the asymmetry in vortices height and lateral wake motion in the experiment (fourth Fig.1.10) and in SAS-SST results (sixth Fig.1.10).

Among the other advantages, CFD allows for an analysis of the drag generated by each body segment (Defraeye *et al.*, 2011). Moreover, it is particularly suitable for multiple cyclists study and drafting effects (Defraeye *et al.*, 2014; Blocken *et al.*, 2013; Oggiano *et al.*, 2016).

### 1.3. Drag measurement techniques in experimental studies

In cycling aerodynamics investigations, the measurement of the drag force can be performed in either a direct way through a force balance or in indirect ways with methods estimating the drag coefficient and the reference area or their product, called the drag area (Debraux *et al.*, 2011). In this section, a review of these methodological approaches is presented.

#### 1.3.1. Wind tunnel experiments

In reviewing the less recent advancement in understanding cycling aerodynamics, wind tunnel balance force measurements emerge as current methodological reference to establish drag force or drag area (Debraux *et al.*, 2011), as shown in the previous section. They are generally performed in either open or closed test sections with model supported by struts. An underneath balance composed of strain gauges is able to measure forces and moments on the three axes. An effective representation of the reality would require ground and wheels with same tangential velocity as the free stream one, with cost of implementation of rotating belts being a deterrent. Therefore, a cheaper alternative consists of a stationary elevated ground plate placed between the balance and the model in open-test section wind tunnels or boundary layer suction systems placed ahead of the model in closed-test section ones. In both the cases, the purpose is to avoid the wind tunnel boundary layer entrainment but these solutions do not solve the problem of replicating the same relative speeds as in reality. Other typical problems in the wind tunnel are common to the aircraft industry and are well summarised in Barlow *et al.* (1999) and Crouch *et al.* (2017). Especially, the balance force measurements can be affected by balance imprecision for dynamic tests (Candau *et al.*, 1999) or repeatability of the cyclist position (Crouch *et al.*, 2017). Wind tunnels specifically equipped for cycling testing mitigate the issues regarding position repeatability (Chowdury and Alam, 2012), can investigate limited drafting cycling aerodynamics (Celis and Ubbens, 2016) or reproduce ground movement and weather conditions (Bäckström *et al.*, 2016).

While balance measurements are the preferred choice in wind tunnel experiments, an alternative method to measure the cyclist drag area is based upon a control volume approach (Unal *et al.*, 1997; Van Oudheusden *et al.*, 2007). A detailed theoretical explanation is presented in section 2.2. In practice, the momentum conservation is applied on an ideal streamtube under the assumption that all the variations of momentum within the tube can be obtained by measuring the momentum deficit and relative pressure in the wake of the tested object, i.e. the outlet plane of the streamtube. Crouch *et al.* (2016a) applied this technique with the data from total pressure probes spaced 25 mm in both directions, finding a drag area with 3% inaccurate underestimation with respect to the reference balance measurement.

Nevertheless, dynamic pressure probes are an intrusive point-wise measurement technique and have a limitation in case of reverse flow or high crossflow. Therefore, the advent of Large-Scale PIV (section 2.1.2) applications for wind tunnel measurements (Scarano *et al.*, 2015) opened unprecedented possibilities for control volume measurements based on Particle Image Velocimetry.

The first application of the integral momentum conservation by using Tomographic PIV was performed by Terra *et al.* (2016) in an open test section wind tunnel. The cyclist full-scale model was in static asymmetric condition and the same relevant structures as Crouch *et al.* (2016a) were highlighted (Fig.1.11). The authors underlined the necessity of considering the pressure term in the drag area evaluation, by applying pressure reconstruction (Van Oudheusden, 2013). The control volume drag force was within one standard deviation of the reference balance measurement. Later work of Shah (2017) showed the possibility to use 4D-PTV for the control volume approach, but the drag area differed up to 5% from the balance measurement, depending on the considered velocity. Although he retrieved the usual flow structures, Shah (2017) underlined a Reynolds number effect in comparison to the experiment of Terra *et al.* (2016): in fact, the wake velocity contour was shrunk in both the vertical and horizontal direction due to a Reynolds number three to four times higher. However, it is important to point out that the measurement plane was 0.2m closer to the same cyclist model in the 4D-PTV experiment and this might have played a role in the wake width difference.

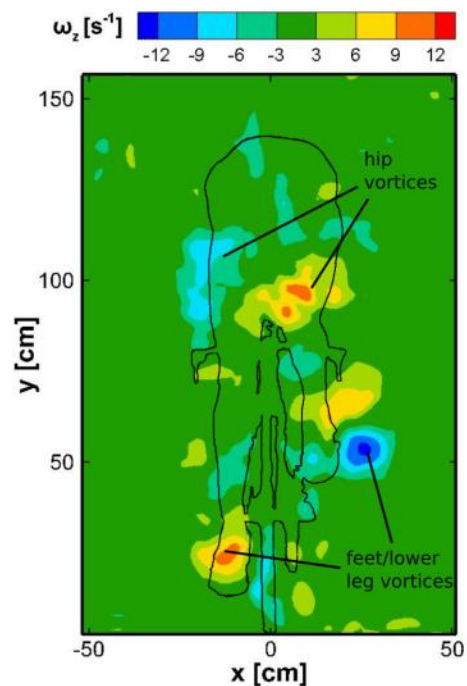


Figure 1.11: Wind tunnel Tomo-PIV measurement in asymmetric static time-trial posture, reproduced from Terra *et al.* (2016)

### 1.3.2. On-site measurement techniques

Apart from wind tunnel measurements, in the field of experimental aerodynamics, on-site techniques offer a possible cheaper and less accurate alternative (Debraux *et al.*, 2011). If little variation of the rolling resistance with velocity (Martin *et al.*, 1998) and the drag coefficient (Chowdury and Alam, 2012) were assumed, the cyclist power would depend on the cube of the cyclist speed. Therefore, simultaneous power and speed measurements allow to retrieve both the drag area and the rolling resistance coefficient through a linear regression analysis. However, the results have an inaccuracy that might bring to deceiving conclusions as for Grappe *et al.* (1997), who found little variations between the time-trial and the drops posture. Currently, higher sampling frequency powermeters from SRM are the preferred choice among the professional athletes (SRM, 2015) and their accuracy was validated by Martin *et al.* (1998). However, as crank-based power meter, they provide information about the power delivered by the cyclist and chain losses may affect the evaluation of power provided at the rear wheel. Nowadays only one manufacturer, PowerTap, sells powermeters at the rear hub.

Another on-site technique is known as the towing method, whose setup presents a vehicle towing the cyclist with a strain gauge equipped cable. Similarly, linear regression is applied but based on the relation between force and square of velocity (Capelli *et al.*, 1993). Because of the air turbulence generated by the towing vehicle (Debraux *et al.*, 2011), Candau *et al.* (1999) stressed the dependence of the results on the atmospheric conditions as well as the distance of the cyclist from the vehicle back. Therefore, he introduced a simplified deceleration method. It is an evolution of the coasting-down method, but it differs as it is performed on flat terrains rather than in descents. At a certain time the athlete stops pedalling and application of the Newton's second law allows to estimate drag area and rolling resistance coefficient through velocity and time measurement by infrared detectors. The accuracy of the method strongly depends on accurate time and velocity measurements. The method was applied to distinguish the effect of different head positions on the drag area, with a reported standard deviation not exceeding 5% of the mean. Reduction of air environment effects brought Candau *et al.* (1999) to suggest as a good practice performing deceleration methods in hallways.

For the purpose of this research, the effect of environmental fluctuations on cycling performance deserves supplementary attention. [Watkins and Alam \(2014\)](#) distinguished two major effects, one due to wind and the other to turbulence intensity in the flow, coming from the ground boundary layer. While the former can vary the cyclist yaw angle, the second can be source of different transition and separation points on the cyclist body. In the first case, yawed winds generally increase the traditional bike drag up to an angle of  $10^\circ$ , while aerodynamically shaped bike frames generate local side force whose component can create a thrust effect as for sails ([Hill, 1993](#)). Rather than the environmental fluctuations per se, [Watkins and Alam \(2014\)](#) underlined that the ratio between turbulence intensity and cyclist speed is of interest. In order to reduce the effect of environment turbulence intensity, experiments in residential suburbs with smooth terrains (turbulence intensity lower than 10%) were advised, with the tested object proceeding headwind rather than tailwind.

When comparing these on-site techniques with respect to the wind tunnel, the advantages of a better reproducibility of the reality and lower cost is counterbalanced by a large amount of sources of uncertainty as assumptions in constant drag area or rolling coefficient with velocity, atmospheric variables, chain efficiency, power measurements inaccuracy due to variations in pace ([Crouch et al., 2017](#)). Moreover, they are not capable of providing flow field data, as it could happen in the wind tunnels or in CFD simulations.

On one hand, it is for this reason that [Lukes et al. \(2005\)](#) saw in CFD the tool to promote further cycling aerodynamics understanding. On the other hand, although [Debraux et al. \(2011\)](#) and [Candau et al. \(1999\)](#) recognised the wind tunnel as the current reference benchmark, [Crouch et al. \(2017, p. 92\)](#) has regarded on-site techniques as “the true metric of success for any aerodynamic optimisation”.

### 1.3.3. The Ring of Fire

The mentioned advent of Large-Scale PIV applications in wind tunnels was favoured by increased production rates of sub-millimetre flow tracers known as Helium-Filled Soap Bubbles (HFSB). The possibility to measure velocity on volumes up to  $10^4 \text{ cm}^3$  and to evaluate the cyclist's drag area through the control volume approach ([Terra et al., 2016](#)) brought [Sciacchitano et al. \(2015\)](#) to envisage a new on-site measurement techniques: the Ring of Fire. In the original Ring of Fire concept, the authors imagined the possibility to set up a Tomographic PIV measurement system in a training facility that the athlete would use, as a velodrome. HFSBs would be dispersed by a *ring* equipped with both the illumination and imaging system. The authors underlined the following advantages:

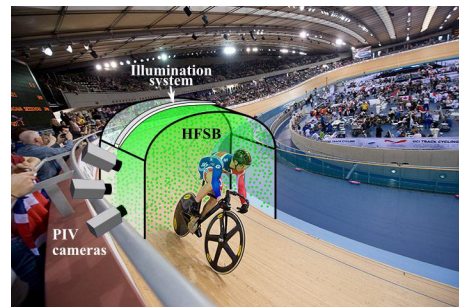


Figure 1.12: Schematic of the Ring of Fire concept as introduced by [Sciacchitano et al. \(2015\)](#)

- The full flow field velocity tensor can be obtained in a non-intrusive manner and on a real tested object without further sensors;
- As it is an on-site technique, dynamic measurements are naturally possible without facing the difficulty in replicating relative ground motion as in the wind tunnels;
- Flow field variables are supported by drag evaluation in terms of both instantaneous and average data;
- It is easier to perform drafting investigations as well as cornering studies.

The Ring of Fire has not been conceived only for cycling aerodynamics but it can be applied to any speed sports as skating, running, bobsleigh and motorsport aerodynamics.

A proof of concept of the technique was performed on a transiting sphere by [Terra et al. \(2017\)](#). Tomographic PIV and associated pressure reconstruction ([Van Oudheusden, 2013](#)) allowed to evaluate momentum, pressure and Reynolds stress terms in the sphere drag area, with an overall value independent of the downstream plane choice. Moreover, the authors proved the technique to be suitable for both instantaneous and average acquisitions, with the drag area within the reported literature. [Terra](#)

*et al.* (2017) underlined two fundamental aspects following their research. Firstly, differently from a wind tunnel application, it is necessary to accurately measure the model speed and the inflow conditions in applying integral momentum conservation for a transiting object. Secondly, future reductions in system complexity were advised as in the far wake of the sphere (after five diameters) the pressure term contribution on the drag is negligible and the wake recovers the free stream pressure: thus only momentum deficit is necessary and a Stereo-PIV measurement is suitable enough to perform momentum integral conservation.

Spoelstra (2017) successfully applied the Ring of Fire concept on a cyclist in an outdoor environment (Fig. 1.13). By using Stereo-PIV with a high-speed system (acquisition frequency  $f = 2\text{kHz}$ ) the author performed for the first time a streamwise wake scan of a cyclist in dynamic conditions on-site. Both time-trial and upright brake-hoods postures were investigated. Comparison with the literature was considered satisfactory at a qualitative level and uncertainty on the mean drag area was reported below 5%. In comparison to Crouch *et al.* (2016a), Terra *et al.* (2016) and Shah (2017), the author underlined the differences with a fixed-floor conditions in a wind tunnels. After conducting the same experiment in the wind tunnel, balance measurements differed up to 10% in mean drag area, after applications of wind tunnel corrections.

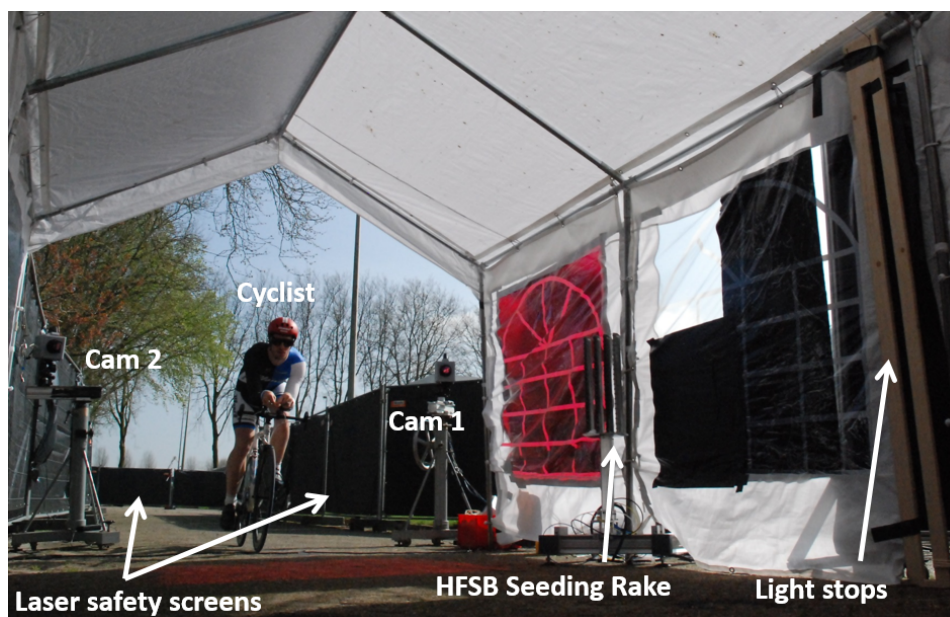


Figure 1.13: Ring of Fire setup of Spoelstra (2017)

Despite the crank angle variation, no clear cyclic trend in the drag area was underlined, while streamwise fluctuations can be referred to low reproducibility of the cyclist posture, influence of the outdoor environment conditions, measurement error, tendency of the cyclist wake to abandon the acquisition plane, lack in seeding concentration uniformity. Regarding the measurement error, peak locking affected the PIV vectors evaluation, due to the large pixel size of the camera sensor and the lens aperture used to gather enough light. This limitation seems proper of the adoption of a high-speed system. Moreover, the author stressed the data acquisition with high-speed systems to pose a bottleneck on the experiment total time, given a time frame of five to ten minutes per passage to store all the images.

#### 1.4. Project goal and associated research questions

For long time, research and optimisation in cycling aerodynamics has been mostly based on a trial-and-error procedure due to the lack of phenomena insights linked to forces variation. Applications of wind tunnel measurement systems including qualitative and quantitative flow visualisations have made a step forward in determining the main flow features governing the cyclist wake. However, the trial-and-error based approach is the only possible for on-site measurements, which benefit from

simplicity and cost. When comparing on-site measurements and wind tunnel measurements, the main favourable points to be underlined are a more representative reality and lower cost for the first while a more controlled environment and easier quantitative aerodynamic investigations for the second. As computational fluid dynamics has potentially an advantage in this respect, it does not come to surprise that it is taking over in cycling and more in general in sport aerodynamics (Hanna, 2012), despite its difficulties in replicating a real model and its measurement inaccuracy. In the latest years, an innovative concept has emerged after Technische Universiteit Delft proposal regarding conducting large scale PIV experiments in on-site conditions for speed sports (Sciacchitano *et al.*, 2015). The work of Terra *et al.* (2017) and Spoelstra (2017) has posed a basis for a potentially more mature evolution.

Spoelstra (2017) could apply integral momentum conservation via Stereo-PIV at a full scale level with a high-speed system<sup>2</sup> in outdoor conditions. On the negative side, the usage of a high-speed system generates a large amount of data leading the execution of two cyclist passages in a time frame between five to ten minutes. Moreover, uncategorised sources of uncertainties harm the accuracy and precision of the mean result. They could be divided in three categories:

- Caused by the used PIV system, for instance the size of the pixels for a high-speed camera and the relatively low power of a high-speed laser, better discussed in section 2.1.3;
- Caused by the outdoor setup, for instance the atmospheric fluctuations, the seeding concentration and its spatial distribution;
- Proper of a Ring of Fire experiment, for instance cyclist's posture, crank angle, trajectory and velocity repeatability.

These uncertainties could pose an open question regarding small drag differences between two different configurations.

Given that, the project goal is to make the Ring of Fire concept feasible for industrial applications through the implementation of an indoor low-speed PIV system. The hypothesis regards the fact that a Ring of Fire concept using low-speed system and being performed in a more controlled environment, such as an indoor test site, could lead to: higher precision in drag area and velocity field; consequent better quantification of the accuracy in the drag evaluation; increased Dynamic Velocity and Spatial Ranges (Adrian, 1997); lower total experiment time given lower image storage time with a low-speed system. Moreover, additional development of the system is envisaged to further strive towards the goal and make the Ring of Fire a drag measurement tool benchmark for speed sports. Therefore, the main research question reads:

*Which drag area precision and time per passage has an indoor Ring of Fire got by using a low-speed Stereo-PIV system and which factors contribute to its precision in comparison to a high-speed system?*

The time frame proposed to answer this research question is confined to the typical time frame for a MSc thesis at TU Delft. System improvement is envisaged before the experiment with the project resources being allocated via the Aerodynamics department of TU Delft. Answering this research question provides an achievement of the project goal.

On the negative side, the use of a low-speed system limits the experiment in terms of streamwise resolution of the cyclist wake: in fact, time-resolved data cannot be obtained. Nevertheless, this is not necessary to compute the drag area once the pressure term is less influential (Terra *et al.*, 2017). By using 4D-PTV, Shah (2017) concluded that the pressure term in the evaluation of the drag is lower than 1% already at a distance equal to one cyclist hip width, while Tomo-PIV measurements of Terra *et al.* (2016) highlighted the pressure term to be about 3.6% at a similar location. Despite the works of Terra *et al.* (2016) and Shah (2017), a sub-question relates which is the extent of the streamwise pressure decay in the wake so as to consider unaffected by bias errors the simplified control volume approach. In fact, none has ever evaluated the streamwise pressure field variation for a cyclist. At the

<sup>2</sup>The experiment of Spoelstra (2017) is hereafter referred as the High-Speed ROF experiment because of the acquisition frequency being of the order of *kHz*, while the current project is referred as Low-Speed ROF, with an acquisition frequency of the order of *Hz*.

same time, the stagnation pressure of the cyclist also affects the choice of the inflow plane and this choice on the mean and drag area standard deviation is an open question.

Among its advantages, the high-speed setup benefited from the high acquisition frequency because phase-locked flow fields average could be performed even without a synchronisation between the PIV user and the cyclist. Frequency of order of  $Hz$  for the Low-Speed ROF would require design for a synchronised image acquisition setup. Instead, a primary corner point of the Low-Speed setup deals with the advantage of lower amount of data acquisition. This would reduce both the acquisition time and the post-processing time and open the question regarding the time performances of a Low-Speed ROF in comparison to a High-Speed ROF. Therefore it is crucial for future industrial applications to establish how long a single cyclist passage experiment would last and how long an experimental campaign capable of providing satisfactory average data.

The main research question aims at evaluating the drag area standard deviation and thus it provides information about the possibility of distinguishing unambiguously the drag between two different configurations. Assessment of the factors contributing to the standard deviation opens the question whether the uncertainty depends on the unsteadiness caused by the variation of the crank cycle and legs posture, given the maximum variation between asymmetric and symmetric regimes to be 20% (Crouch *et al.*, 2014). Hence, a sub-question regards which is the standard deviation for both static and dynamic measurements. Successful static measurements would allow to distinguish the small drag differences between asymmetric and symmetric flow regimes. However, if this did not happen, comparison between upright and time-trial postures could be considered as in Spoelstra (2017).

In Spoelstra (2017)'s experiment the cyclist's wake tended to get out of the measurement domain and this affected the drag evaluation. One may wonder whether this was an effect due to the outdoor conditions rather than an intrinsic effect of the wake. Moreover, the measurement of the cyclist speed was conducted for a single streamwise location for each passage, with the assumption of a constant velocity for each of the streamwise wakes. Therefore, it is relevant to consider how the drag evaluation varies if the cyclist speed is measured as a function of time.

The setup in the high-speed Ring of Fire suffered low planar uniformity in the seeding concentration and advancements in this are foreseen with additional design for an indoor experiment.

For validation purposes, one would ask whether flow features are in accordance to the findings of Crouch *et al.* (2016a) and Crouch *et al.* (2014) and the extent of possible bias error in the drag area.

A successful achievement of the research goal would introduce a velocity field and drag area measurement system less expensive, more representative of the reality and capable of investigating innovative configurations (real cornering, group drafting, ...) in comparison to a wind tunnel. Furthermore, the Ring of Fire would be more informative than current on-site techniques. This application is foreseen at an industrial level and with applications extended to various speed sports.

**Thesis outline** The theoretical principles regarding Particle Image Velocimetry and drag evaluation from integral momentum conservation are presented in chapter 2. The setup of the experiment and relative procedures are discussed in chapter 3, while the necessary data reduction techniques in chapter 4. Chapter 5 discusses the results and answers the research questions while conclusions and recommendations are summarised in chapter 6. In addition, appendix A shows an additional experiment performed to evaluate the performance of the adopted synchronisation system between image acquisition and cyclist's passage. Finally, appendix B discusses the influence of the assumption of constant environmental conditions on the drag results.





# 2

## Theoretical principles

In this chapter the theoretical basis necessary to implement the Ring of Fire concept is presented. As the main aim of the Ring of Fire is to provide a drag measurement on a transiting object based on flow field visualisations, the principles of Particle Image Velocimetry are firstly introduced (sec.2.1). Particle Image Velocimetry permits to measure the velocity flow field in the wake of the transiting object, i.e. the pedalling cyclist. As the drag force is obtained by applying momentum conservation through the streamwise direction, Stereo-PIV is discussed in section 2.1.1. Moreover, the full-scale object dimensions require the employment of tracers known as helium-filled soap bubbles, so as to illuminate a large domain of interest and capture the full wake of the cyclist. This can be referred as Large Scale PIV (sec.2.1.2). Finally, it is pertinent to discuss the most relevant differences in the use of systems with either high or low acquisition frequencies in PIV (sec.2.1.3), as one of the project research question aims at answering the specific capability of a low-speed system.

As mentioned, drag force is evaluated through the application of integral momentum conservation. This is applied from an Eulerian point of view in a control volume and the relations are derived for a reference system with a typical wind tunnel mindset (sec.2.2.1) and modified accordingly for the reference system proper of the Ring of Fire (sec.2.2.2).

### Contents

---

<b>2.1 Particle Image Velocimetry in Aerodynamics</b> . . . . .	<b>18</b>
2.1.1 Stereoscopic PIV . . . . .	19
2.1.2 Large Scale PIV . . . . .	21
2.1.3 Low-speed and High-speed PIV . . . . .	22
<b>2.2 Control volume approach</b> . . . . .	<b>23</b>
2.2.1 Wind tunnel model reference system . . . . .	23
2.2.2 Ring of Fire reference system: application on transiting objects . . . . .	25

---

## 2.1. Particle Image Velocimetry in Aerodynamics

Particle Image Velocimetry is a non-intrusive whole field technique used to perform an indirect velocity measurement by acquiring subsequent frames of illuminated flow particles. Its working principle and setup are shown in Fig.2.1. While a brief explanation of the general setup and theoretical principles is provided in this section, the reader is referred to the book of [Raffael \*et al.\* \(2007\)](#) for a more comprehensive discussion.

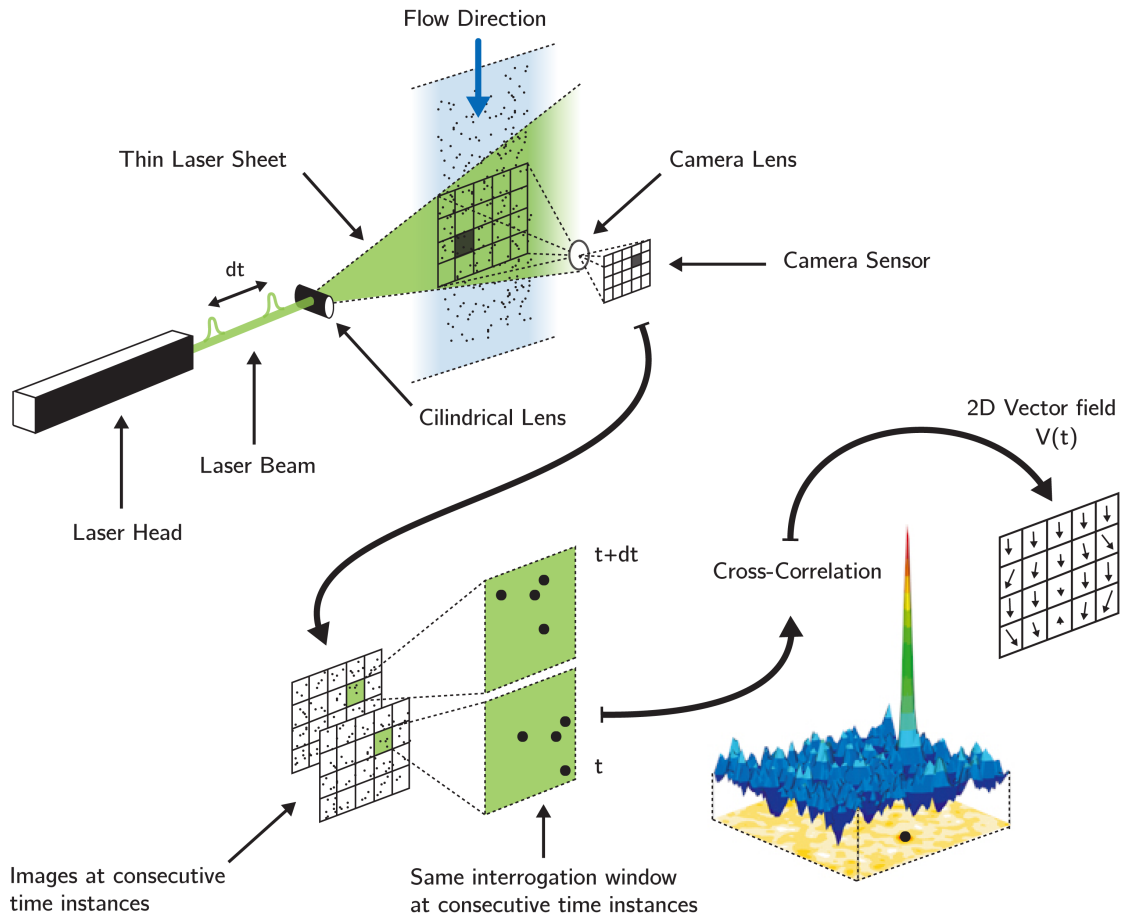


Figure 2.1: Working principle and setup of Planar PIV, reproduced from [Giaquinta \(2018\)](#)

The area of interest, called field of view (FOV) is illuminated by a high intensity light source, with lasers being the most common choice in aerodynamic investigations due to the ease in bundling them in sheets without chromatic aberrations. In the illuminated area, particles with a diameter of the order of  $\mu m$  are dispersed in a uniform manner. Their small diameter permits a good tracing fidelity of the air flow as their time response is proportional to  $d_p^2$ . This is a consequence of them being characterised by a Stokes' flow regime ([Mei, 1996](#)). Moreover, the relative dimension of their diameter with respect to the laser wavelength collocates them in the Mie scattering regime, such that the light is scattered in spherical vector wave functions with power proportional to a range between  $d_p^2$  and  $d_p^6$ . A recording device with either a CCD or a CMOS sensor is used to record the image plane of the illuminated object plane. A lens is used to focus the image particles. Due to the finite lens aperture, the Airy disc characteristic of the Fraunhofer diffraction pattern is dominant in determining the image particle size. The camera sensor size and the desired FOV determines the magnification factor of the optical system. Based on that, the relative position of the laser plane with respect to the lens is chosen as well as the lens focal depth.

At least two subsequent frames are acquired by the camera synchronised with the laser pulse sep-

eration  $\Delta t$  (dt in Fig. 2.1). This is one of the most important design parameters of a PIV experiment, chosen in such a way that the majority of the particles are correlated between the two frames within a small subset of the field of view, called interrogation window (IW). In each interrogation window there must be a sufficient amount of particles to retrieve statistical information about the mean particle displacement, through the application of cross-correlation. The correlation functions of the two frames of the interrogation window are Fourier-transformed. Then, their resulting product is inversely transformed in the discrete cross-correlation function of the two frames for that window. As the cross-correlation function is a function of the planar coordinates, the displacement of the highest correlation function peak from the origin (which corresponds to the particles position on the first frame) corresponds to the integer mean pixel displacement of the flow within the interrogation window. Applications of Gaussian fitting of the peak can provide particles displacement with a sub-pixel accuracy, which is possible only if the particles image diameter is about 2 pixels, otherwise a bias error known as peak locking occurs. In practice, the highest cross-correlation peak position relative to the origin of the cross-correlation map provides the most probable mean displacement of the particles. Based on the cross-correlation result and on the known time interval  $\Delta t$  between the two frames and the magnification factor of the image, a planar velocity vector per interrogation window is obtained. A more accurate estimation of the velocity vector includes multi-passes cross-correlation and a weighted average of the interrogation window while an increased spatial resolution can be obtained with overlapped windows. This process is repeated for each frames couple, separated by a time interval equal to the acquisition frequency. When this time separation between two successive frame couples is considerably smaller than the flow characteristic time, time-resolved PIV data can be obtained, while in the other cases the technique provides statistical information on the flow field.

A fundamental metric for a PIV experiment is the dynamic velocity range (DVR), i.e. the ratio of the maximum measured velocity with respect to the minimum one. In fact, it is an indication of the ratio between the maximum measurable particle displacement within a chosen interrogation window and the uncertainty of the displacement measurement.

### 2.1.1. Stereoscopic PIV

As shown in section 2.2, the computation of the cyclist's drag through a control volume approach requires to evaluate the flow velocity in the streamwise direction. Differently from the derivation of the drag evaluation from a control volume in Anderson (2011), a cyclist is a highly 3D object and Planar PIV with a plane aligned to the cyclist centreline is not sufficient to capture the mean momentum deficit. Therefore, a different PIV measurement technique is necessary to compute the out-of-plane velocity component in a plane orthogonal to the streamwise direction, as Stereoscopic-PIV. The use of Stereo-PIV rather than PIV volume measurements (e.g. Tomographic PIV, 4D-PTV, among the others) is suggested by Terra *et al.* (2017), in the application of the Ring of Fire concept to a transiting sphere. This approach has been verified by Spoelstra (2017) with a PIV high-speed system. Its limitations concern the impossibility to obtain information regarding the streamwise gradient of the velocity vector components, in comparison to volumetric measurements, and so to be limited in pressure reconstruction and unambiguous vortex detection (Scarano, 2013).

In describing the working principle of Stereoscopic PIV, an introduction regarding the limitation of Planar PIV in presence of strong out-of-plane velocity component is discussed.

**The limitation of Planar PIV** In the classical planar PIV arrangement only one camera is employed. The camera view axis is orthogonal to the laser plane and the technique aims at measuring the in-plane projection of the velocity flow field. As the field of view is two-dimensional and only two components of the velocity vector are obtained, planar PIV can be referred as 2D2C-PIV as well.

Because of the possibility to measure only the in-plane projection of the velocity vector, care should be taken in performing 2D2C-PIV measurements: in fact, the technique can retrieve reliable data when the laser plane is aligned with the freestream flow and it is regarded as two-dimensional. Still the technique has been applied to three dimensional flows when the planar velocity is of interest even at industrial level, although the out-of-plane component can introduce error up to 16% on the planar mean flow, as reported by Raffael *et al.* (2007). The same authors underline the reason for this inaccurate application of PIV in the fact that the error can be barely visible in the qualitative aspect of the results (Raffael *et al.*, 2007, p. 59).

In order to understand the influence of the perspective error in the results, consider the schematic shown in Fig. 2.2, where a sample particle displacement is evaluated with planar PIV. The plane is intentionally shown with an exaggerated thickness: to avoid a loss of correlation due to the out-of-plane component, a 2D2C PIV configuration for a three-dimensional flow needs a laser plane thicker than in conventional 2D flows. The particle moves with a displacement  $\vec{Dx}$  in  $\Delta t$  and the horizontal planar projection of the displacement is equal to  $Dx$ . However, the perspective error due to the angle between the camera view axis and the axis connecting the object and its image causes an overestimation of the particle displacement, equal to  $dx$  in the object plane and to  $dX$  in the image plane. From this example, it is noticeable how the perspective error would decrease with a longer distance  $d_o$  between the lens plane and the laser plane, while at equal plane-to-plane distances it increases radially on the laser plane. Prasad and Adrian (1993) reports the error to be proportional to  $(\Delta z/d_o)^2$ , with  $\Delta z$  being the laser thickness. In the shown figure, the lens plane has been treated as an ideal spherical lens.

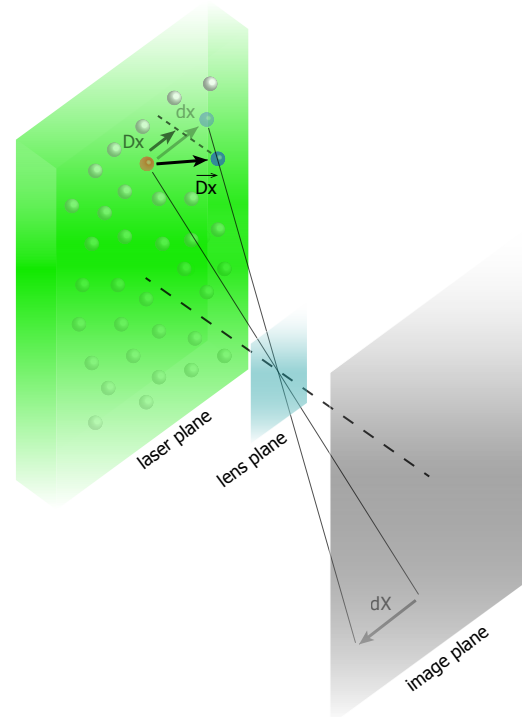


Figure 2.2: Projection error on 2C2D-PIV

**Stereoscopic principle** The planar projection of a three-dimensional vector constitutes an important source of uncertainty in the reconstruction of the in-plane velocity field. Along the years, multiple solutions have been proposed that mainly consist in a modification of the setup and the acquisition principle. All of them share the necessity of evaluating the third vector component to cancel the perspective error. Among these methods, some measure the third velocity component by an additional view using stereoscopic principles while others apply either multiple lasers or multiple laser sheets or variable light intensity and focus arrangement (Raffael *et al.*, 2007; Prasad, 2000). Due to its relative simplicity compared to other 3C-PIV techniques, Stereo-PIV is currently widely used at industrial and academic level. Some examples concerning turbo-machinery, turbulent flows, biomedical flows, car and naval industry are presented in the book of Schroeder and Willert (2008).

Stereoscopic PIV is part of the 2D3C-PIV techniques group: in this case two camera views are employed to acquire the same field of view. The same basic principles as for the classical PIV apply, with the particle displacement evaluated for the two different views. The two views are in general based on two synchronised cameras, although this is not the only possibility. The employment of two cameras allows to perform two Planar PIV and then to reconstruct the three vector components. Understandably, this is possible provided that the angle  $\theta$  between the camera axis and the laser plane vector is known. In fact, as two views are necessary in order to have a different planar pair of components, the camera view axes are not orthogonal with respect to the laser sheet. This is obtained either by tilting both the lens and image plane or by translating the lens plane with respect to the image plane. As the latter configuration has an out-of-plane displacement error three to four times larger than the in-plane displacement for  $\theta = 15^\circ$  (Prasad and Adrian, 1993), the former is more interesting due to the possibility to provide more accurate results. However, the fact that the cameras are tilted causes a variable magnification factor across the field of view together with the fact that the domain is pictured with a skewness increasing with larger  $\theta$ . This requires the adoption of small lens aperture (thus large depth of field) or the satisfaction of the Scheimpflug criterion in order to have all the particles in the FOV in focus (Prasad and Jensen, 1995).

Depending on the cameras relative position with respect to the laser plane<sup>1</sup>, the single frames are corrected based on the results of reconstruction process. The reconstruction process can be either based on mathematical modelling of the studied geometry and its relative position to the cameras or based on a prior calibration, which has the advantage of being more easily implemented on any geometry (Prasad, 2000). Nowadays the current trend is to obtain the mapping functions from the 3D object position to the 2D image one based on a calibration performed on a two-level calibration plate, as large as the area of interest. With the introduction of mapping functions based on perspective equations for a camera pinhole model (Willert, 1997) and the mapping functions correction based on the disparity vectors of particle dewarped images (Wieneke, 2005), it is possible to perform Stereo-PIV even without a perfect alignment of the calibration plate with the laser sheet. Based on the resulting dewarped images correction, the vector field computation proceeds as follows (Wieneke, 2005): the two camera frames are firstly reconstructed on a common grid and 2C cross-correlation is performed. Then the 3C reconstruction through triangulation filtering out the vectors with large reconstruction error. As in 2D2C, after cancelling these badly reconstructed vectors, multi-pass cross-correlation provides more accurate results.

Both Raffael *et al.* (2007) and Prasad (2000) mention  $2 \cdot \theta = 90^\circ$  to be the optimum angle between the two camera view axes. However, the resulting large non-uniformity in the magnification factor strongly affects the in-plane components computation because of a reduced common interrogation window size and an angle  $2 \cdot \theta$  between  $30^\circ$  and  $45^\circ$  is advised.

### 2.1.2. Large Scale PIV

The existence of the Ring of Fire concept completely relies on the introduction of the helium-filled soap bubbles (HFSB, in short). As reported by Caridi (2018), despite they being patented in 1938, helium-filled soap bubbles have been used as qualitative visualisation tool for a long time. Employment of the bubbles for quantitative measurements was limited due to the low achievable production rate and their high response time. Recently, the production rate improvement and the use of sub-millimeter bubbles reopened the possibility to use them for quantitative flow visualisation such as Large-scale PIV with both low-speed systems (Bosbach *et al.*, 2009) and high-speed systems (Kühn *et al.*, 2011). With the term "Large-Scale PIV" it is hereby referred to the possibility of performing PIV with FOV of the order of a square meter.

With a diameter around 0.4 mm, the helium-filled soap bubbles lie in a different light scattering regime than the conventional PIV seeding. In fact, their light scattering power is proportional to  $d_p^2$ , they being in geometric scattering regime (Adrian and Yao, 1985), so with a power ratio  $10^4 - 10^5$  higher than conventional PIV seeding. In practice, Scarano *et al.* (2015) underline how the HFSBs have been the solution towards Large-Scale PIV to bypass the relatively low advancement in the pulse energy of light sources.

The helium-filled soap bubbles are made of a thin film of soap enclosing helium. The helium counterbalances the weight of the soap providing neutrally buoyant particles. This results in a response time of the order of  $10^1 \mu s$  (Scarano *et al.*, 2015) for submillimeter bubbles. The most recent advancements corresponded to an augment of the bubbles production rate to make them suitable for wind tunnel applications. Caridi *et al.* (2016) introduced an aerodynamic rake with staggered wings releasing the bubbles at the airfoils trailing edge through an accumulation system, with a reported rate of 50000 bubbles/s per nozzle and an overall theoretical production rate of  $10^6$  bubbles/s. This allowed to perform Tomographic PIV (3D3C) in low-speed windtunnels. Subsequently, the work by Caridi (2018) led to bubbles being produced directly at the wings trailing edges, through nozzles characterised by air ducts separating the soap solution enclosing helium in tiny bubbles. Shah (2017) and Terra *et al.* (2016) could exploit the new system to perform 4D-PTV and Tomographic PIV respectively in the wake of a cyclist in an open test section wind tunnel, with measurement volumes between  $100 \times 170 \times 3m^3$  and  $100 \times 160 \times 5cm^3$ . Finally, Spoelstra (2017) employed a four wings generator to perform the first Large-Scale Ring of Fire experiment on a transiting cyclist by using a high-speed PIV system in an outdoor environment. The latest improvement within the TU Delft Aerodynamics research group

<sup>1</sup>Among the possible setup configurations there are: Forward-Backward (FB) scattering, with the laser plane vector being the angle bisector of the angle between the camera axes; Forward-Forward or Backward-Backward scattering, with the laser plane being the angle bisector of the angle between the camera axes; Side-Side scattering, similar to FB scattering but with the laser illuminating from an orthogonal direction with respect to the camera axes angle bisector.

coincides with a ten wings system with 200 nozzles, employed by [Giaquinta \(2018\)](#).

### 2.1.3. Low-speed and High-speed PIV

During the most recent years, progress in the recording devices has allowed two different systems to emerge in the PIV research: low-speed and high-speed PIV. Some of the differences are drawn in this section to make the reader aware of the typology of expected results with one of the two systems.

The *speed* term refers to the acquisition frequency achievable between the frame couples. In planar, Stereo and Tomographic PIV the most common theoretical principle in the image acquisition corresponds to a Double-Pulses Double-Frame arrangement, in which each of the two recorded frames is accompanied by a laser pulse at the same frequency. As the pulse energy of the lasers decreases with the repetition rate ([Raffael et al., 2007](#)), the division between the two PIV systems has arisen in order to optimise their role for a specific application. In a low-speed system, a Nd:YAG laser is generally employed with a repetition rate of the order of  $10^1 Hz$  and pulse energy for each pulse of the order of  $10^2 mJ$ . Instead, a high-speed system uses Nd:YLF laser to illuminate the flow with a frequency up to the  $10^1 kHz$  order, while each pulse has got an energy of the order of  $10^0 - 10^1 mJ$ . While the former is successfully employed to retrieve statistical data from the flow, the latter can be used to perform time-resolved PIV. As the particle optical exposure, i.e. the energy per unit area, is proportional to the pulse energy ([Adrian, 1991](#)), the same particle would emit one order of magnitude more energy in the same imaging conditions, when illuminated by a low-speed PIV system. On the other hand, this permits larger cross-sections of the illuminated volume with the same particle diameter, with the cross-section  $\Delta Z^2$  being proportional to  $I_0^{2/3}$ , with  $I_0$  the pulse energy, as derived by [Caridi \(2018\)](#) for the HFSB.

Together with the differences in the laser energy and repetition rate, different camera sensors are generally used for a low-speed and a high-speed system. While in the former case a CCD sensor is the most common choice, a CMOS sensor is used in the latter. A quantitative comparison of the two camera sensors is proposed by [Hain et al. \(2007\)](#). Together with the difference in acquisition frequency matching the laser repetition rates, the CCD sensor has pixel size of the order of  $\mu m$  and a larger pixel full-well capacity than the CMOS sensor, characterised by pixel sizes of  $10^1 \mu m$ . The larger full-well capacity can absorb higher energy from the emitted particle photons without saturating and hampering the surrounding pixels information. However, although a smaller pixel size is a potential advantage as it can be more helpful in avoiding peak locking, a larger sensor size is required in low-speed systems to capture the same FOV. Alternatively, a smaller sensor size requires lower magnification factor to increase the FOV area, with the disadvantage of a larger distance between the lens plane and the laser plane. Consequently, this can reduce the low-speed system advantages due to the higher laser pulse energy.

In comparing high-speed system with low-speed system for a turbulent jet, [Falchi and Romano \(2009\)](#) underline that statistical PIV using a high-speed system requires a larger amount of samples to obtain statistical convergence. This is due to the pulse separation to be shorter than the phenomenon integral time scale, so that the number of effective samples is reduced ([Sciacchitano and Wieneke, 2016](#)). However, different treatment of the samples can still obtain statistical results comparable with low-speed systems, for instance by using sliding sum of correlation ([Meinhart et al., 2000](#)). In fact, although [Falchi and Romano \(2009\)](#) highlight a different image quality between the two systems, with brighter and better contrasted particles for low-speed than high-speed, similar signal to noise ratio levels and similar results on the first and second order moments statistics can be achieved. However, a smaller sensor size was used for CCD than for CMOS in the comparison, with the mentioned requirements to capture the same FOV spoiling part of the low-speed higher illumination advantage.

From a practical point of view, it is relevant for this project to state the different operational cost the two systems require. On one hand, capturing the cyclist wake for several meters can require up to 5-10 minutes for image saving with a high-speed system ([Spoelstra, 2017](#)). Instead, low-speed system image saving is on the order of few seconds, due to the smaller amount of data. This is a fact that makes low-speed system more interesting for drag measurements through the Ring of Fire concept, provided that the focus is only on statistical data.

## 2.2. Control volume approach

In this section the principles of the loads determination from PIV are drawn under the Eulerian representation of a control volume. The application of the control volume principle relies on defining the control volume as a portion of a streamtube (Anderson, 2011). In the particular case of an object moving on the ground, one of the streamsurface of the streamtube corresponds to the ground itself.

### 2.2.1. Wind tunnel model reference system

Within a control volume, mass and momentum are conserved and the integral conservation relations can be used to derive loads exchanged between the fluid and the tested object. In aerodynamics, it is common to study the aerodynamic loads in a fixed reference frame integral with the tested model  $\mathcal{R}' = \{x', y', z'\}$  in a wind tunnel. It replicates the reality condition in which the model is moving at a constant velocity and the reference frame is inertial and integral with the object itself. In the wind tunnel, the air is blown with a constant freestream velocity  $U_\infty$  corresponding to the model velocity in the reality case. Therefore, in incompressible flow, the momentum conservation along the streamwise direction can be written (Mohebbian and Rival, 2012) as:

$$D(t) = -\rho \iiint_{CV} \frac{\partial u}{\partial t} dV - \rho \iint_{CS} u (\mathbf{u} \cdot \mathbf{n}) dS - \iint_{CS} (p - p_\infty) n_z dS + \iint_{CS} (\bar{\tau} \cdot \mathbf{n})_z dS \quad (2.1)$$

with  $D(t)$  the instantaneous force along the streamwise direction  $z$ , i.e. the drag force,  $\rho$  the fluid density,  $CV$  the control volume,  $CS$  the boundary surface of the control volume,  $u$  the flow velocity  $z$  component,  $\mathbf{u}$  the flow velocity vector,  $p - p_\infty$  the relative pressure with respect to the ambient pressure,  $\bar{\tau}$  the viscous stress tensor. The first term in equation 2.1 is the unsteady variation of momentum within the control volume. Wu *et al.* (2005) rewrite this term as a surface integral evaluated on the boundary surfaces of the control volume while Rival and van Oudheusden (2017) adds to the derivation an additional force term due to the acceleration of the fluid volume caused by the unsteady tested object movement. However, the latter is null with a constant free stream, such that eq.2.1 becomes:

$$D(t) = -\rho \frac{\partial}{\partial t} \iint_{CS} z (\mathbf{u} \cdot \mathbf{n}) dS - \rho \iint_{CS} u (\mathbf{u} \cdot \mathbf{n}) dS - \iint_{CS} (p - p_\infty) n_z dS + \iint_{CS} (\bar{\tau} \cdot \mathbf{n})_z dS \quad (2.2)$$

with  $z$  coordinate of the control surface measured from a fixed external reference frame  $\mathcal{R} = \{x, y, z\}$ .

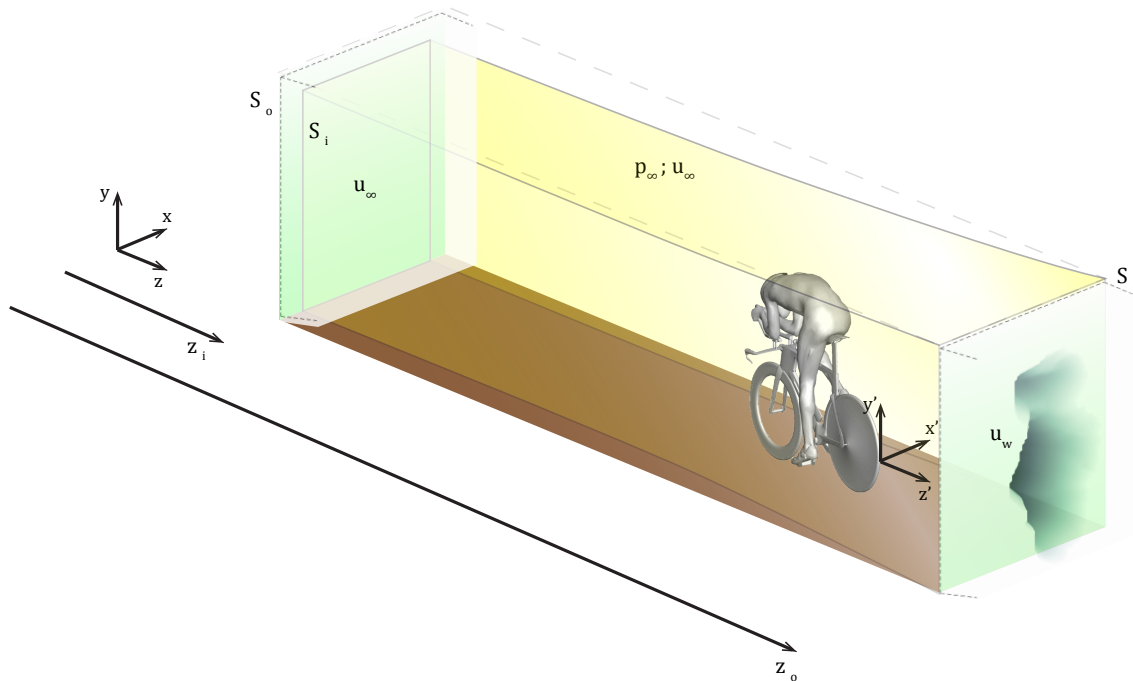


Figure 2.3: Control volume approach in the wind tunnel reference frame

When the control volume is chosen in such a way that the side surfaces correspond to the stream surfaces of a stream tube as the yellow surfaces in Fig.2.3, additional considerations can be drawn:

- With the side surfaces sufficiently far from the body, freestream conditions are recovered. Therefore,  $p - p_\infty = 0$ ,  $\mathbf{u} \cdot \mathbf{n} = 0$  as there is no mass crossing the stream surfaces by definition and the viscous term can be neglected (Kurtulus *et al.*, 2007);
- On the ground surface the velocity is either null for no-slip condition or just horizontal when moving ground is present. Hence, no momentum flux occurs through the ground. As the forces due to pressure apply orthogonally to the ground stream surface, also their contribution to the drag is null;
- The inlet and the outlet of the streamtube are orthogonal planes to the streamwise direction. They are not stream surfaces, thus the integrals in equation 2.2 need to be solely evaluated on the inlet and the outlet planes. Moreover, Kurtulus *et al.* (2007) show that the viscous stresses contribution is negligible when the inlet and outlet planes are sufficiently far from the tested object.

Based on this, eq.2.2 can be written as:

$$D(t) = -\rho \frac{\partial}{\partial t} \left[ -\iint_{S_i} z_i u_\infty dS + \iint_{S_o} z_o u_w dS \right] - \rho \left[ -\iint_{S_i} u_\infty^2 dS + \iint_{S_o} u_w^2 dS \right] + \left[ \iint_{S_i} (p_i - p_\infty) dS - \iint_{S_o} (p_o - p_\infty) dS \right] \quad (2.3)$$

with the index  $i$  referring to the inlet plane and  $o$  to the outlet one, with flow velocity  $u_\infty$  and  $u_w$  respectively. In Fig.2.3,  $u_\infty$  is represented by a constant white contour level, while the velocity deficit  $u_w$  is shown at the outlet plane. Application of conservation of mass in incompressible flows  $\rho \iint_{S_i} u_\infty dS = \rho \iint_{S_o} u_w dS$  retrieves:

$$D(t) = -\rho \frac{\partial}{\partial t} \left[ (z_o - z_i) \iint_{S_i} u_\infty dS \right] - \rho \left[ \iint_{S_o} (u_w - u_\infty) u_w dS \right] - \left[ \iint_{S_o} (p_i - p_o) dS \right] \quad (2.4)$$

$$= \rho \iint_{S_o} (u_\infty - u_w) u_w dS + \iint_{S_o} (p_o - p_i) dS$$

where the unsteady term has been cancelled as there is no time variation of the terms in brackets, provided that the freestream flow exhibits low levels of turbulence. Notice that this relation does not require to assume  $S_i = S_o$ . With the choice of sufficiently far planes upstream and downstream, the pressure reaches the freestream value and the pressure difference between outlet and inlet is null. Finally, the instantaneous drag coefficient can be written as:

$$C_d(t) = \frac{1}{0.5 u_\infty^2 A} \iint_{S_o} (u_\infty - u_w) u_w dS \quad (2.5)$$

with  $A$  the tested object reference area, which is the frontal area for a bluff body. In order to take into account the variations of the frontal area as well, the concept of drag area is often introduced  $C_d A$ , measured in  $m^2$ .

With the measurement of the instantaneous velocity field, it is possible to obtain the drag area of a tested object as a cyclist. The relation in equation 2.5 requires to measure the wake velocity component in the streamwise direction only in the outlet area and to integrate the freestream velocity on the same area. By repeated measurements of the instantaneous drag coefficient, statistical information can be obtained. The requirements for capturing the entire cyclists' wake justify the adoption of Large-Scale PIV to measure the velocity flow field in the outlet plane, as performed in a wind tunnel by Terra *et al.* (2016) and Shah (2017).

### 2.2.2. Ring of Fire reference system: application on transiting objects

In the Ring of Fire concept the control volume is not intuitively easy to be pictured and it requires some abstraction. It represents a case in which the reference system is fixed on the ground with a transiting object. A schematic of this situation is shown in Fig.2.4. In this case the control volume is not fixed but is integral with the cyclist. Instead, the measurement plane is fixed. As the object moves relatively to it, the measured flow field at every time instant refers to a different cyclist position. Hence, each flow field measurement corresponds to a different spatial location with respect to the cyclist as well as a different time evolution of the flow.

As a consequence, one would say that every measured plane corresponds to a different control volume inlet or outlet. However, as shown in Fig.2.3, the inlet and the outlet surfaces  $S_i$  and  $S_o$  are not equal, in order to satisfy conservation of mass and momentum. Therefore, if the measurement plane surface area were considered as large as the control volume outlet plane  $S_o$ , the measured upstream plane<sup>2</sup> would have the same surface area  $S_o$ , larger than the corresponding control volume inlet surface  $S_i$ . In describing the effect of the reference transformation on the application of the control volume approach, the object velocity  $U_c$  will be considered constant.

In the Ring of Fire reference system, the first important differences occur in the measured velocity: as described by Terra *et al.* (2017), passing from the wind tunnel case scenario to the current one does not allow to say that the velocity at the inlet plane  $u_i = u_\infty - u_\infty = 0$ , with  $u_\infty = -U_c$ . In fact, differently from a wind tunnel, the environmental fluctuations can be larger than tunnel turbulence intensity as large scale motions could occur. This is the case of Spoelstra (2017) for instance, who employed the Ring of Fire system in an outdoor environment. This constitutes a striking difference in comparison to apply a control volume approach in the wind tunnel. In fact, the resulting eq.2.4 shows that measurement only at the downstream plane is necessary to obtain the object drag. Instead, in the Ring of Fire approach, also the environmental fluctuations need to be measured to obtain the momentum deficit between outlet and inlet velocity fields.

At the downstream plane the velocity in the wake of the cyclist is measured, and the reference transformation results in the relative momentum deficit with respect to the cyclist's velocity  $u_o = u_w - u_\infty$ , with  $u_\infty = -U_c$ . Therefore, in a fixed reference frame, measuring the flow field through the application of PIV provides the environmental fluctuations  $u_i$  when the plane is upstream of the transiting object, while provides the wake flow field  $u_o$  when the plane is downstream.

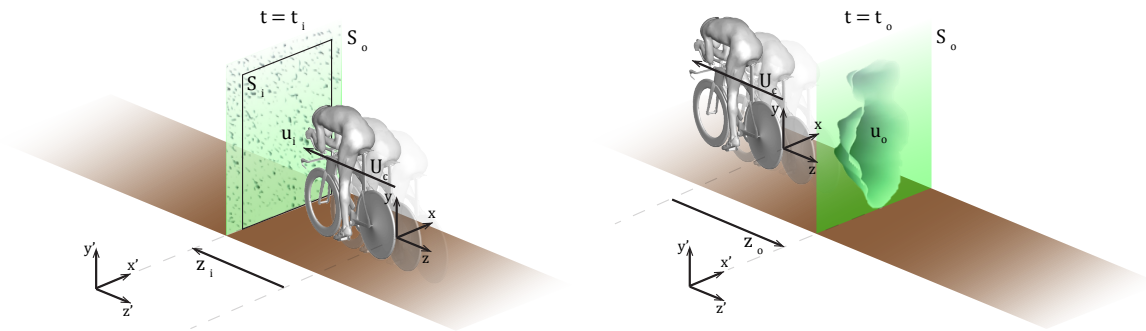


Figure 2.4: Control volume approach in the Ring of Fire: upstream flow measured at  $t_i$ , downstream flow at  $t_o$

Based on this discussion, Terra *et al.* (2017) and Spoelstra (2017) substituted in eq.2.4  $u_\infty = u_i - U_c$  and  $u_w = u_o - U_c$ , obtaining:

$$\begin{aligned}
 D(t) &= \rho \iint_{S_o} (u_i - u_o) (u_o - U_c) dS + \iint_{S_o} (p_o - p_i) dS \\
 &= \rho \iint_{S_o} (u_o - u_i) (U_c - u_o) dS + \iint_{S_o} (p_o - p_i) dS
 \end{aligned} \tag{2.6}$$

<sup>2</sup>An upstream plane is a measured flow field before the passage of the object, while a downstream plane is measured afterwards.

In this derivation two assumptions were made as the starting equation was eq.2.4:

- The unsteady term in the instantaneous drag is neglected: as previously discussed, in a fixed reference frame the relative position between the object and the measurement planes varies with time and the measured flow field is both a space-temporal evolution; however, [Spoelstra \(2017\)](#) mentions that in a quasi-steady scenario this term can be neglected even in the instantaneous drag, based on the work by [Ragni et al. \(2011\)](#). For a pedalling cyclist, typical time-trial reduced frequencies are of the order of 0.115 and the ratio between unsteady phenomena to steady ones has been proven to affect little the qualitative flow field ([Crouch et al., 2016a](#));
- The magnitude of the variations of the environmental velocity is small compared to the cyclist velocity. In fact, the step from eq.2.3 to eq.2.4 requires to say that  $u_\infty \iint_{S_i} u_\infty dS = \iint_{S_i} u_\infty^2 dS$ , so  $(u_i - U_c) \iint_{S_i} (u_i - U_c) dS = \iint_{S_i} (u_i - U_c)^2 dS$  in the Ring of Fire case, which assumes that the spatial variations of  $u_i$  can be neglected.

While the effect of the second assumption may be proved small as discussed in appendix B, the first one could be unnecessary when the momentum conservation is ensemble-averaged. In fact, ensemble-average of eq.2.6 results in the mean drag as:

$$\bar{D} = \rho \overline{\iint_{S_o} (u_o - u_i) (U_c - u_o) dS} + \overline{\iint_{S_o} (p_o - p_i) dS} \quad (2.7)$$

when the pressure term is negligible as in the object far wake, the mean cyclist's drag area can be written as:

$$\overline{C_d A} = \frac{1}{0.5 U_c^2} \overline{\iint_{S_o} (u_o - u_i) (U_c - u_o) dS} \quad (2.8)$$

So far, the tested object velocity has been considered constant. However, in reality this is not the case and the cyclist velocity fluctuation along the same test passage introduces a time variation of the overall momentum within the control volume.





# 3

## Experimental Setup and Procedures

In this chapter, the setup regarding the performed experiment and the associated testing procedures are going to be discussed. In particular, the attention will be drawn towards the setup implementation steps and the associated challenges together with relevant feasibility and time constraints. The intent is to provide the reader with relevant information to perform an indoor Ring of Fire experiment in the future.

Building the overall setup requires cooperation and interface between different equipment and resources as: selecting test facility and building the seeding container (section 3.1); identifying the cyclist and the suitable bike for the experiment (section 3.2); preparing the PIV setup (section 3.3) and synchronising the image acquisition with the cyclist relative position (section 3.4); measuring the cyclist velocity as a function of time (section 3.5). Moreover, a careful testing procedure is required to reduce experiment time and human factor incidence on the final result (section 3.6).

### Contents

---

<b>3.1 The Indoor Facility and the Tunnel</b> . . . . .	<b>30</b>
<b>3.2 The Tested Object</b> . . . . .	<b>31</b>
<b>3.3 PIV Setup</b> . . . . .	<b>33</b>
<b>3.4 Wake synchronisation</b> . . . . .	<b>35</b>
<b>3.5 Cyclist Velocity measurement</b> . . . . .	<b>36</b>
<b>3.6 Testing procedure</b> . . . . .	<b>38</b>

---

### 3.1. The Indoor Facility and the Tunnel

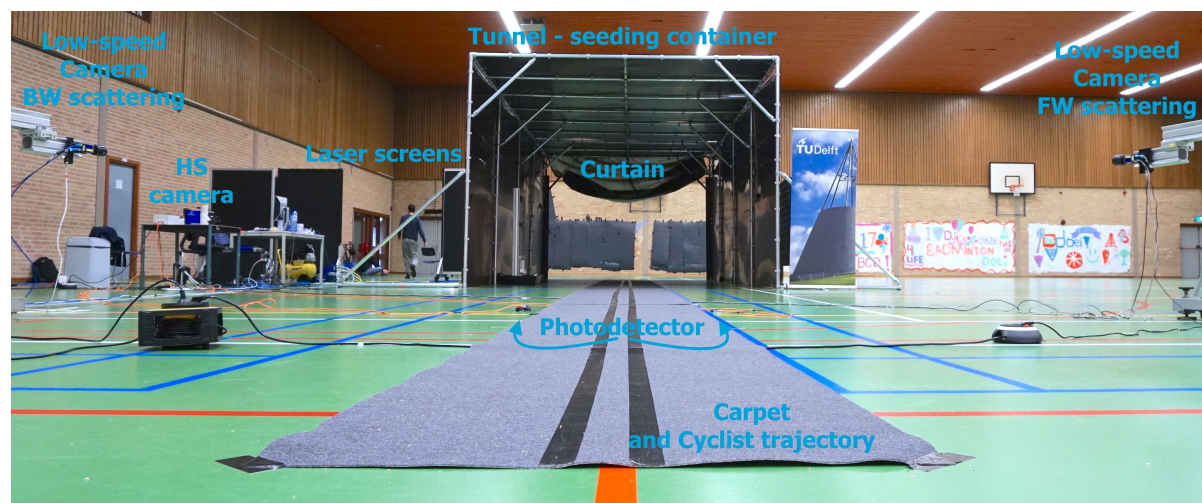
The testing facility was the main indoor sport hall of the sports complex Sporthal Brasserskade, located at Sportring 1, 2616 LK, Delft. It was an empty room 46m long and 32m wide. A ventilation system was installed on the ceiling and there was no compressed air available at the location.

Within the indoor facility, a tunnel was built and placed. It was conceived and designed with the collaboration of the TU Delft Aerodynamics department with the intent of avoiding the PIV seeding to spread in the room. This was not only a concern in terms of safety, as the soap in the seeding could make the floor slippery and dangerous for the cyclist, but as well as for the sake of a successful experiment. In fact, differently from usual wind tunnel experiments, the tunnel served as a seeding container to maintain high seeding density in the measurement domain.

The design of the tunnel took into account several factors. First of all it had to be structurally stable and painted with a dark colour to reduce laser light reflections. Other than these requirements, the tunnel could be modular to permit adjustable length and hydrophobic to avoid soap to spoil integrity of the panels. This was particularly relevant for the designed tunnel, which consisted of wooden panels integrated in an aluminium frame. The frame presented four modules 2.5m long each, so that the overall tunnel length was 10m. A 0.15m wide and 1.75m high vertical cut was present in the structure at 5.12m from the tunnel entrance to allow laser light to pass through. At the exit of the tunnel a curtain was placed to avoid bubbles early escaping from the tunnel. The curtain was not positioned at the tunnel entrance as the predominant direction of environment flow was towards the tunnel exit, due to the room ventilation system. Given this, the laser cut was positioned nearly the centre of the tunnel to minimise the effects of the opening curtain and allow sufficient seeding ahead of the laser. Regarding the other two dimensions, the tunnel was 4m wide and 3m high. Although the cross-section of the tested object had got its primary dimension along the vertical direction, the tunnel was larger in the horizontal direction. This was a consequence of the results of the Ring of Fire experiments of [Spoelstra \(2017\)](#), who showed the cyclist wake to have a spanwise oscillatory movement. Therefore, the tunnel sides were placed far from the cyclist to minimise the wall influence on the wake development. By considering both solid and wake blockage ([Barlow et al., 1999](#)) for an upright configuration, the largest overall blockage in such a tunnel is less than 4% in the current experiment. The tunnel was placed along the room longest dimension: 31m before the laser plane were used as acceleration zone, while the remaining 15m as braking and turning zone.

On the floor, a 20m long carpet was placed with the last 10m inside the tunnel. The purpose was to avoid the floor surface to become excessively slippery for the cyclist because of soap. On the carpet, two parallel lines were placed 0.08m apart from each other through black duck tape, to provide a trajectory guidance to the cyclist.

An overview of the whole setup is presented in the following figures, with a schematic view in Fig.3.1. In the next sections each item is singularly discussed.



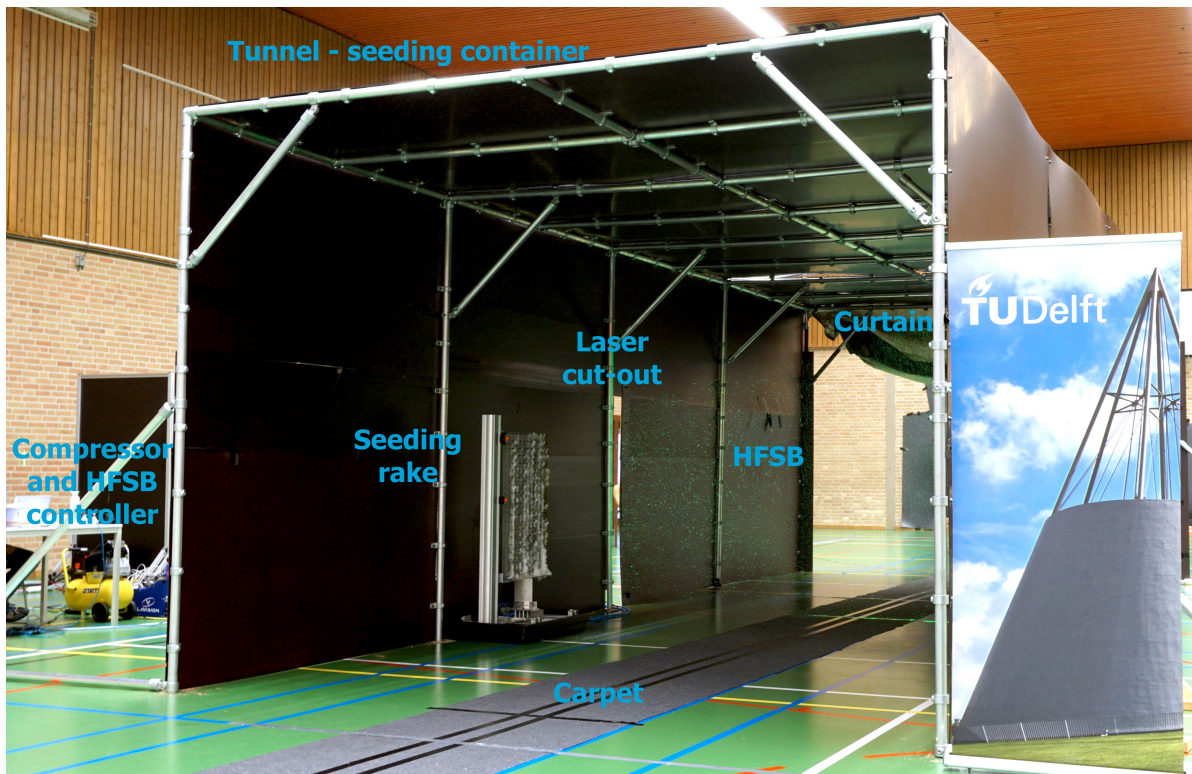
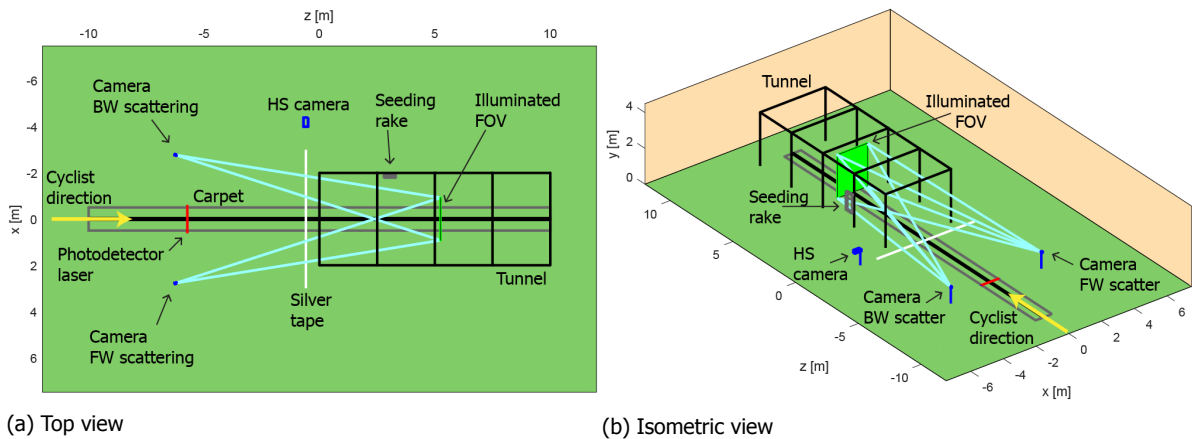


Figure 3.1: Setup overview



### 3.2. The Tested Object

In the current project the tested object was a cyclist riding a time-trial bike. At the moment of testing, the cyclist weighed 68kg and he was 1.89m tall. He wore a short-sleeve time trial suit and helmet provided by Team Sunweb. Due to low temperatures, the rider wore a personal long-sleeve suite underneath. Moreover, for safety reasons, the cyclist wore a pair of laser goggles.

Regarding the bike, it had a 2017 Giant Trinity TT Advanced Pro frame, the same frame Tom Dumoulin used in the last stage of Giro d'Italia 2017 ([Giant-Bicycles, 2017](#)). The frame size *Large* had got a crank length of 0.175m and a wheelbase of 1.018m. It was equipped with a lenticular disc rear wheel and a spoked front wheel, both with an overall diameter of 0.666m. The total bike length was 1.684m and the seat was 1.055m from the ground. The bike was not equipped with the aerodynamically shaped AeroVault water bottle ([Giant-Bicycles, 2017](#)). The bike gears had either 53 or 39 teeth for the crank and a minimum of 11 teeth for the rear hub.



Figure 3.2: 2017 Team Sunweb Bike

As shown in section 1.2.2, the chosen test similarity parameter, the reduced frequency, is linked to the choice of the gear ratio. In order to match the typical time-trial reduced frequency (Crouch *et al.*, 2016a), equal to 0.115, a gear ratio of 53/12 was used ( $k \approx 0.119$ ). With such a gear ratio and wheel diameter, the cyclist travelled for 9.24m each crank revolution. The crank angle is defined based on the convention for the right pedal in Fig.3.2. The positive rotation is in the sense of proceeding and  $\varphi = 0^\circ$  corresponds to the pedals horizontally aligned with the right foot in front.

The cyclist and the bike were tested in four different configurations:

- Static Time-Trial Asymmetric configuration: this corresponds to the cyclist not pedalling at  $\varphi = 75^\circ$ , i.e. the maximum extension for the right leg; the torso and the head are aligned with respect to the ground, the head looks forward and the arms are extended along the handlebars as in Fig.3.4a and the left silhouette in Fig.3.3);
- Static Time-Trial Symmetric configuration: similar as the previous one, in this case  $\varphi = 15^\circ$ , i.e. the thighs are aligned with respect to each other with the right foot lower than the left one (central silhouette in Fig.3.3);
- Dynamic Time-Trial configuration: the cyclist is in the time-trial configuration with torso and head aligned to the ground, head looking forward and arms extended on the handlebars (Fig.3.4a); the cyclist keeps on pedalling;
- Dynamic Upright configuration: the cyclist keeps on pedalling with the hands on the brake hoods, the torso inclined at  $20^\circ$  and the head looking forward (Fig.3.4b). The frontal area of the upright configuration can be distinguished from the time-trial one by comparing the right silhouette with the left one in Fig.3.3, presented at the same crank angle.

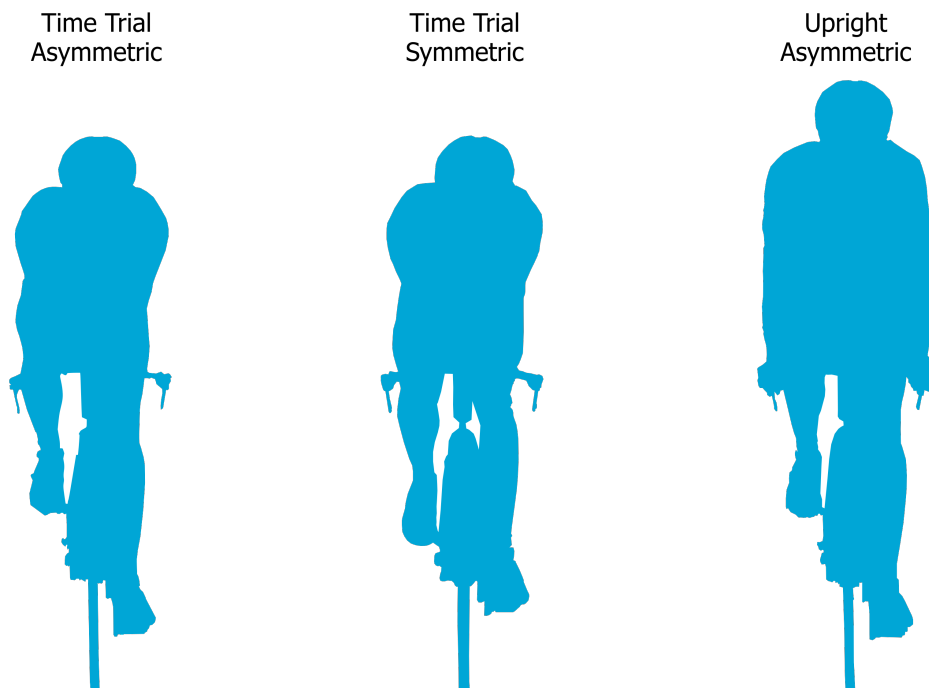
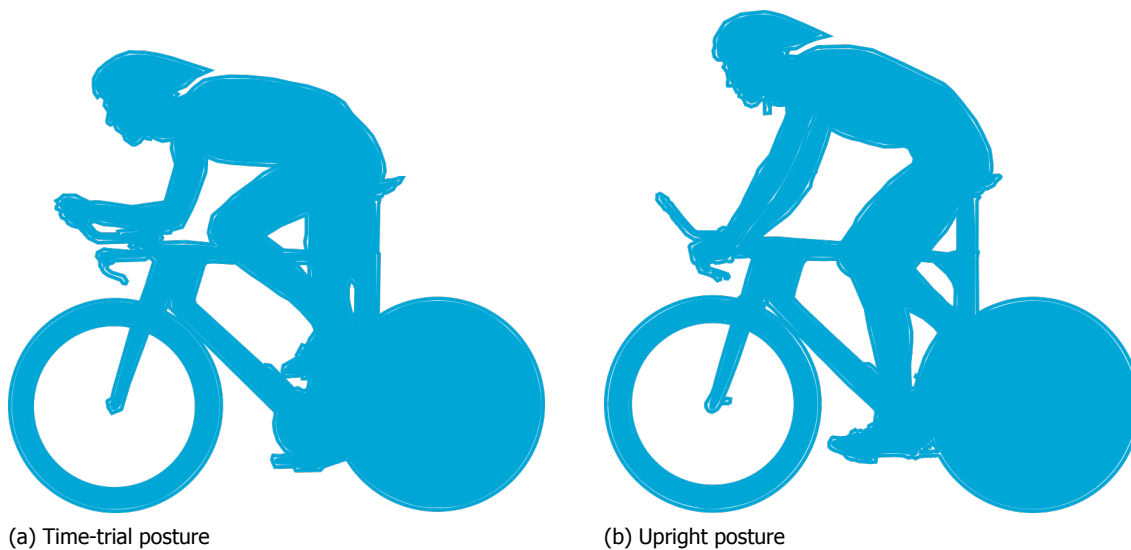


Figure 3.3: Cyclist configurations silhouettes - Front view

Figure 3.4: Cyclist configurations silhouettes - Side view



### 3.3. PIV Setup

The low-speed indoor Ring of Fire finds the heart of its equipment setup in Large Scale Stereoscopic PIV. Its objective consists of reconstructing the velocity field by capturing the full cyclist's wake. A field of view (FOV) with 1.83m width and 2.41m height was used. The highest dimension was chosen as the vertical one so as to capture the wake even in upright position. The dimensions of the Field of View were chosen following the results of the experiment of [Spoelstra \(2017\)](#). As the author noticed a frequent lateral movement of the far wake out of the field of view, its dimensions were chosen in order to reduce this circumstance.

In the Stereo-PIV setup two low-speed cameras were used and they corresponded to a CCD 2Mpx Imperx Bobcat IGV-B1610 model ([Imperx, 2013](#)), rebranded LaVision. Such a camera had a 2Mpx sensor  $1628 \times 1236$ px with each square pixel with a dimension of  $4.4\mu\text{m}$ . The maximum frequency with full sensor was 25Hz. Each camera was equipped with an AF Nikkor lens with focal length  $f=35\text{mm}$  and a bandpass filter for the laser wavelength (Fig.3.5). Scheimpflug adapters were not necessary. Both the cameras were positioned at 0.925m from the ground.

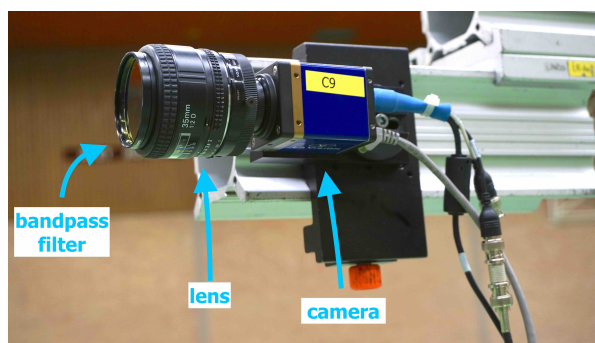


Figure 3.5: Imperx Bobcat IGV-B1610

The experiment light source was a Quantel Evergreen 200 laser, with maximum pulse energy equal to 200mJ and pulse width equal to 7ns at 180mJ. The laser wavelength is equal to 532nm while pulse repetition rate is 15Hz maximum ([Quantel, 2015](#)). The laser was positioned at 5.2m from the tunnel side wall and its beam axis was aligned with the 0.15m cut-out, at 5.245m from the tunnel entrance. The laser beam was expanded through 4 different lenses so that in the middle of the trajectory path, bounded by the black duct tape on the carpet, the laser had a thickness of 0.04m. At 1m distance before the middle trajectory the laser thickness was equal to 0.035m while equal to 0.045m one meter after. The laser sheet thickness was chosen based on the possibility to capture a larger depth of the flow field in order to increase the seeding density. This choice had to be traded with the fact that a thicker laser plane has got lower light intensity per volume and hides the assumption that the flow field has not overcome large variations. Given the dependence of the large scale turbulence phenomenon

on the geometric scales of the tested object, this assumption is valid as the characteristic cyclist length scale (Crouch *et al.*, 2017) is at minimum  $\sqrt{A_c} = 0.56\text{m}$ , with  $A_c$  the cyclist frontal area. Moreover, in order not to lose most of the laser expansion on the ground, the laser was inclined at an angle of  $4^\circ$ . On the sides of the laser head, laser screens were placed for safety reasons. Considering an average thickness of  $0.04\text{m}$ , the illuminated volume relative to the FOV is equal to  $0.173\text{m}^3$ . Laser and camera synchronisation was achieved through a Programmable Timing Unit X (PTU, in short) from LaVision, with the entire system able to perform maximum at  $8.33\text{ Hz}$ . Acquisition software was DaVis 8.1.2, while postprocessing software was DaVis 8.4.0.2.

During the experiment, an image acquisition frequency of  $8\text{ Hz}$  was used. Cameras and laser were used to visualise particles immersed in the flow to retrieve the velocity field. The used particles were helium-filled soap bubbles with an average diameter between  $0.3$  and  $0.4\text{ mm}$ . They were produced by a seeding rake made of  $200$  nozzles distributed over  $10$  parallel wings. Each nozzle is  $0.05\text{m}$  apart from each other so that the seeding rake dimensions are  $1 \times 0.5\text{ m}$ . Despite it being intended to be used in wind tunnels to seed a stream tube with these dimensions, in this experiment the seeding rake was used to seed the in-house built tunnel. Helium soap bubbles were obtained through a supply unit, the LaVision Helium-filled Soap Bubble (HFSB) Generator, providing pressurised air, soap and helium. The supply unit permitted to tune the pressure, given the helium provided by a  $200\text{L}$  helium bottle and the air from a Stanley®DL/250/10/24 compressor. The compressor specifications include a flow rate of  $250\text{L}/\text{min}$ , maximum pressure of  $10\text{bar}$  with an air tank of  $24\text{L}$ . This compressor was capable of providing the air massflow required by a fully operating seeding rake: considering  $200$  nozzles and a flow rate of  $70\text{L}/\text{h}$  per nozzle, this corresponded to  $233\text{L}/\text{min}$ .

Table 3.1: Equipment and setup parameters

Imaging 		Seeding 		Illumination 	
Sensor	1628 x 1236 px	HFSB diameter	0.3 - 0.4 mm	Average laser thickness	0.04 m
Pixel size	4.4 $\mu\text{m}$	Theoretical HFSB image diameter	1.68 px	FOV	2.41 x 1.83 m <sup>2</sup>
Focal length lens	35 mm	Production rate (nominal)	6 M bub/s	Laser energy	200 mJ
Lens aperture	35/5.6 = 6.25 mm	Seeded volume dimensions	10 x 4 x 3 m	Tested object 	
Magnification factor	0.00297	Timing 		Frontal area (Asymmetric)	TT: 0.316 m <sup>2</sup> Upright: 0.402 m <sup>2</sup>
Digital image resolution	1.48 mm/px	Acquisition Frequency	8 Hz	Frontal area (Symmetric)	TT: 0.311 m <sup>2</sup> Upright: 0.397 m <sup>2</sup>
Stereo angle	28.2°	Pulse time interval	3 ms	Bike length	1.684 m

The design of the experiment included the following guidelines to choose the main parameters contributing to the results. The adopted Stereo-PIV configuration corresponded to a cross-scattering one, so that the orthogonal axis of the laser plane is the angle bisector of the two camera axes. Feasibility dictated this choice, given the presence of the tunnel seeding container. As the interested phenomenon corresponds to a bluff-body wake field, this design choice caused the PIV setup to be constrained by the fact that the main velocity component is along the plane orthogonal direction. Therefore the pulse time interval between two subsequent frames was chosen based on the out-of-plane component of the measured velocity field, so that the out-of-plane particles displacement never exceeded one fourth of the laser thickness within such an interval. As the out-of-plane component is dictated by the convection of the wake, its maximum speed is proportional to the cyclist speed. As shown in section 5.1, the cyclist velocity never exceeded  $5.5\text{m}/\text{s}$ , so  $\Delta t = 1800\mu\text{s}$  would be required. In practice, a  $\Delta t = 3000\mu\text{s}$

was adopted without out-of-plane loss of correlation.

Positioning of the cameras is another design choice dictated by the chosen cross-scattering regime. In this case, as shown in Prasad (2000), accuracy on the out-of-plane component is harmed with camera axes angle lower than  $30^\circ$ . The necessity of visualising the mentioned FOV and to avoid the tunnel entrance to be seen by the cameras required that the camera were at 11.445m from the laser plane with an axes angle slightly larger than  $28^\circ$ . This corresponded to a digital image resolution of 1.48mm/px, thus a magnification factor  $M=0.00297$ .

The final design parameter concerns the PIV optics. As described in section 2.1, the image particle diameter should be as large as two pixel in order not to have peak locking. This limits the lens aperture to a maximum of  $D_a = f/6.7$ , considering the HFSB diameter between 0.3 and 0.4mm. However, in order to have higher exposure intensity and considering the lens aperture neighbours of the maximum to be either  $f/5.6$  or  $f/8$ , the larger  $D_a = f/5.6 = 6.25\text{mm}$  was chosen. With this lens aperture, the particle diameter was expected to be about 1.68px. Nevertheless, in practice, the particle diameter was always larger than 2px, avoiding peak locking to impair the measurement accuracy. A summary of the main equipment and setup parameters is presented in the tables in Tab.3.1.

### 3.4. Wake synchronisation

At the relatively low frequency used to acquire subsequent frames for the Stereo-PIV measurements, the synchronisation between the cyclist passage and the image acquisition is of primary importance, differently from the high-speed Ring of Fire. In order to perform such a synchronisation, a through beam photoelectric sensor was used. It was a WS/WE12L-2P410 type branded SICK. It consisted of an emitter and a receiver. A red-light laser class 2 beam is emitted in a range from 0 to 10m, with a light spot diameter of 1mm at 1m distance. The light has a frequency of 2.5 kHz while the photodetector response time is less than 0.2 ms (SICK, 2017). The two components of the photoelectric sensor were placed on the floor at 1.12m far from each other. They were at 5.73m from the tunnel entrance and both connected through a 10m DOL-1204-W10M cable to a interface box designed at the TU Delft Aerodynamics department. The interface box transfers the voltage signal to the Programming Time Unit and it was used by DaVis as an external trigger. Moreover, the same signal triggered the acquisition of cyclist images to obtain his velocity, as described in section 3.5.

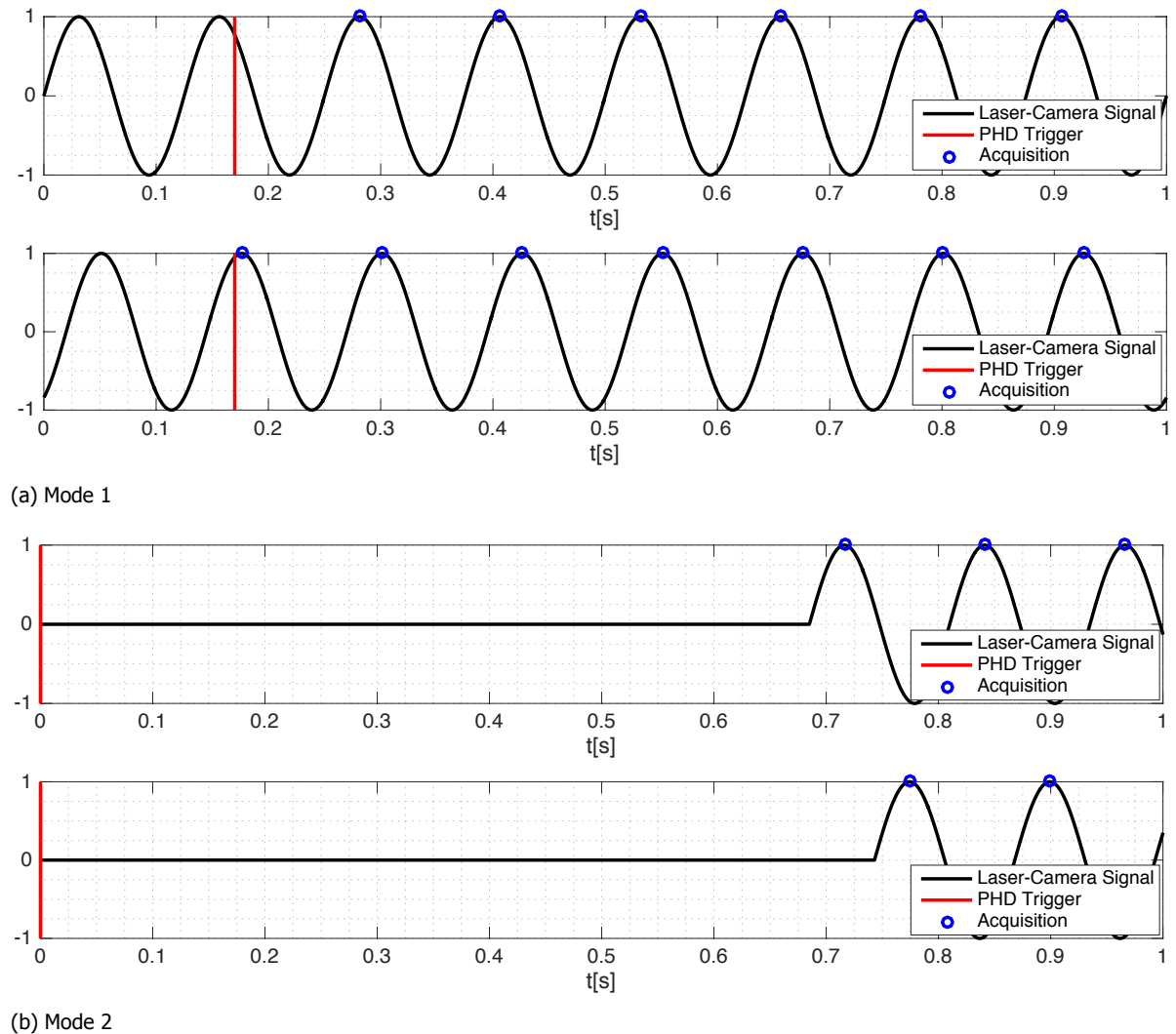
Two different methods were used to trigger the PIV image acquisition during the experimental campaign, hereafter referred as mode 1 and mode 2. The differences are ascribed to the setting of the DaVis software and the hardware connection.

In mode 1, the interface box signal is sent to the Trigger port of the PTU through the cable enabling a single signal to start the image recording. The single signal is transmitted when the red-light laser beam is obscured by the lowest part of the front wheel tyre for the first time. The working principle is illustrated with the comparison of two different test passages in Fig.3.6a. The DaVis recording sequence is enabled by the user, and this time instant varies relatively to the trigger reception (red line). Images are overwritten on the RAM until the external trigger is received and images are stored (blue dot). The relative time difference between two tests for the same wake plane is limited by the chosen acquisition frequency. For this experiment, mode 1 can provide a time error in synchronisation up to  $1/8 = 0.125\text{s}$ , assuming a perfectly constant cyclist velocity among the tests and throughout a single passage. Mode 1 was used for the static experiments.

In mode 2, the interface box signal is sent to the TTL\IO port of the PTU. The image acquisition process in the recording sequence in DaVis is preceded by a flag enabled by the reception of the trigger. The latter is still the same single signal originated by the cyclist passage through the laser beam. In this case, no image acquisition is performed before the received trigger and this should guarantee a synchronisation of the wake planes, if the cyclist velocity is constant as well as the system delay. The delay between the cyclist passage and the effective beginning of the image acquisition was measured with a secondary test in a subsequent campaign, described in the appendix A. If the delay is not constant, the synchronisation between the cyclist passage and the image acquisition is hampered by it.

In the subsequent campaign a mean delay of 0.685s was measured, but with a standard deviation of 0.058s. Two sample tests are shown in Fig.3.6b, the first with the mean delay and the second with an additional one standard deviation. Given the time response of the photoelectric sensor, the delay and its standard deviation had to be ascribed to the ensemble of the hardware setup, electric interference and DaVis software. Mode 2 was used for dynamic experiments.

Figure 3.6: Trigger modes comparison: two sample tests for each mode



The implemented system could not fully resolve the synchronisation problem and an additional manual correction was performed in the data reduction phase, described in section 4.1.

### 3.5. Cyclist Velocity measurement

The cyclist velocity was measured by two different methods, one based on high frequency images acquisition and one based on magnetic field oscillations.

**High-speed camera** Similarly to [Spoelstra \(2017\)](#), a high-speed camera was used to retrieve the cyclist velocity for each single test in a certain streamwise location. The camera was a LaVision Imager Pro HS 4M camera with a 4Mpx sensor with equal dimensions of 2016px.

The camera is placed at 0.59m from the tunnel entrance, with the view axis at 0.83m from the ground and 4m far from the trajectory centreline. Therefore, camera images allow to compute the

cyclist velocity when the rearmost point of the rear wheel is 6.432m from the laser plane. In front of the camera, a silvered line of tape is placed on the floor so as to evaluate the relative cyclist streamwise position.

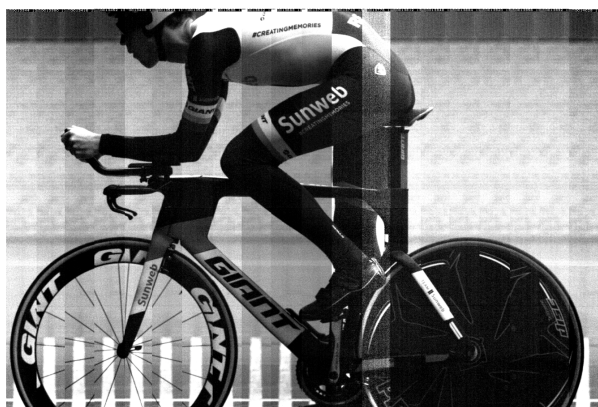


Figure 3.7: HS camera reconstructed cyclist image

Once the camera was positioned, its acquisition was enabled through an external trigger which corresponds to the photodetector system presented in section 3.4. Practically, both the PIV image acquisition and the cyclist velocity image acquisition were triggered together by the first passage of the cyclist through the photodetector laser beam. Then the high speed camera acquired 3000 cropped images at a set frequency of 2kHz, thus for a total time of 1.5s. The sensor was cropped mainly in the width so as to establish the cyclist position relative to the silvered tape line. A reconstructed full cyclist image based upon a sequence of the cropped images is shown in Fig.3.7, acquired through Pco.dimax software. The silhouettes shown in Fig.3.4 were based on these reconstructed images.

As shown in Table 3.2, images storing lasted about one minute and it was the principal time bottleneck in the testing procedure.

**Magnetic sensor** On the chassis frame connecting the crank and the rear hub a magnetic sensor was placed, provided by Team Sunweb. It was secured by two cable ties around black tape, as visible on Fig.3.8.

At the same radius as the sensor, six magnets were placed on the disc of the rear wheel through transparent adhesive pads. Each magnet was placed with an equal angular distance of 60° and had got a diameter of 20mm. Only one out of the six magnets had got a diameter of 10mm. The magnetic sensor consisted of a magnetometer detecting the three components of the surrounding magnetic field (Garmin, 2018). Through the detection of a magnet passage, information regarding distance travelled and velocity were acquired and sent to a bike computer through an ANT+™ protocol (ANT™, 2014).



Figure 3.8: Magnetic speed sensor and magnets on the rear wheel

During the experiment a Garmin Edge ® 810 bike computer was used. On the bike computer the outer arc length spanned between two magnets was set, equivalent to  $0.666\pi/6 = 0.349\text{m}$ . It stored the distance travelled and the cyclist velocity with a frequency of 1Hz for each test, based on the data acquired by the magnetic sensor. The software algorithm reducing the magnetic sensor data was not disclosed. It is worthy to notice that the velocity measurements acquired through this tool allowed to reconstruct the entire cyclist velocity history for each test, providing information as its deceleration in coasting.

Before each single passage, the cyclist started the recording procedure for one lap on the bike computer, so that each test velocity history was separately stored from each other.

### 3.6. Testing procedure

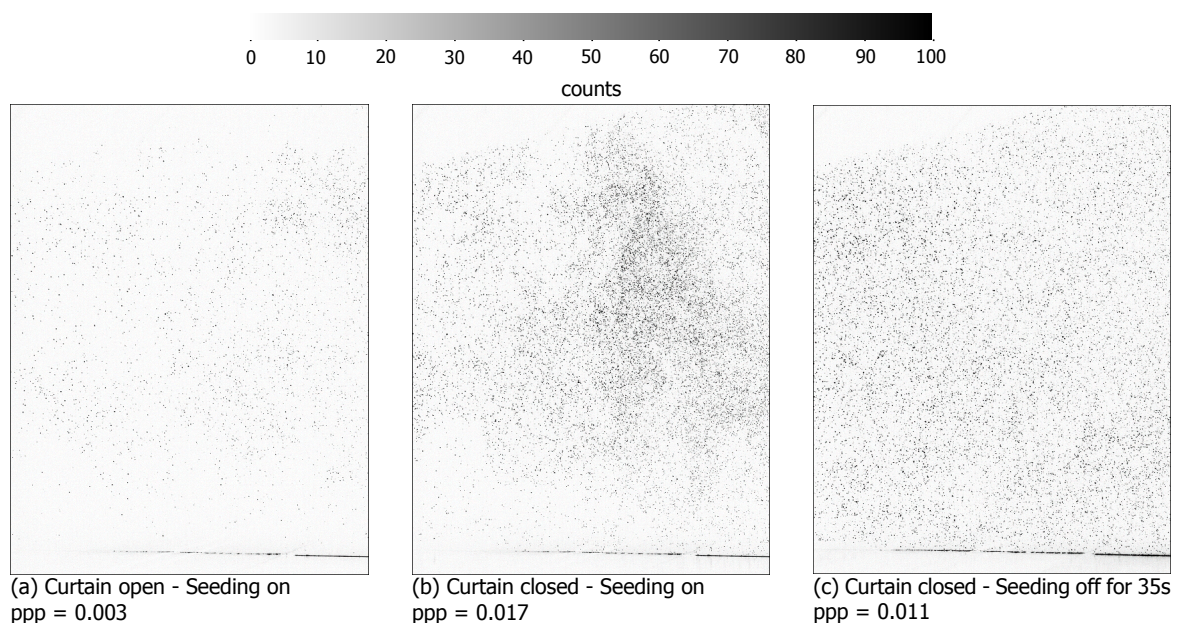
**Seeding rake positioning** As first task of the setup, the optimal seeding rake position had to be iteratively chosen. In order to place the seeding rake within the container, three main considerations had to be regarded:

- The wake convection: because of the induced velocity by the cyclist, the further downstream wake planes present lower seeding density as the bubbles are convected;
- The enviromental flow: in the sport hall, the presence of the ventilation system and the small differences in pressure field exerts a certain predominant direction to the ambient flow;
- The seeding rake momentum: the seeding rake itself releases the HFSB with a certain momentum, so it creates a certain velocity and pressure field when inserted inside the tunnel.

By using a high-intensity discharge lamp to illuminate the tunnel, it was possible to notice that the flow tended to go towards the exit of the tunnel. Moreover, stagnation of the seeding rake momentum on the opposite tunnel wall created two main flow directions: the particles over the stagnation point tended to go along the vertical wall and then recirculate back, seeding the top part of the tunnel; the particles under the stagnation point tended to proceed towards the exit and then recirculate towards the laser cut-out, seeding the bottom part of the tunnel. Therefore, the rake was placed vertically, aligned to the left wall and between 2.5 and 4m ahead of the laser plane.

A comparison of the seeding density is shown for three different cases in Fig.3.9, which help to explain the choices behind the first steps of a test. In Fig.3.9a and Fig.3.9b the particles light intensity is shown with the seeding rake in operation and the curtain open and closed respectively. In the first case,  $ppp = 0.003$ , the particle per pixel index, while in the second one,  $ppp = 0.017$ . Both the two images were acquired while the seeding rake had been fully operating for two minutes. Firstly, it can be noticed that the seeding density is strongly increased with the curtain closed at the exit of the tunnel. Secondly, the seeding distribution is not uniform and momentum is continuously injected in the FOV. During the tests, the solution in Fig.3.9c was adopted. The seeding rake had been switched off for 35s, after which the image acquisition started: there is no momentum due to the seeding rake and the seeding density is more uniform, although  $ppp = 0.011$ . In general the background intensity is between 0 to 15 counts while the particles intensity is on average over 200 counts.

Figure 3.9: Particle density and light intensity comparison



**Calibration** At the beginning of each day of testing, geometrical calibration and self-calibration were performed. The geometrical calibration adopted the camera pin-hole model (Prasad, 2000) and the calibration plate in Fig.3.10 was used. Each dot had a diameter of 8mm. They were distant 90mm from each other and placed on two levels with a step of 20mm. The Cartesian reference system was based on the origin indicated in the circles dot in Fig.3.10, located at the centre of the cyclist trajectory and at 0.9475m from the ground. Positive z-axis is aligned with a vector normal to the calibration plate and pointing outward.

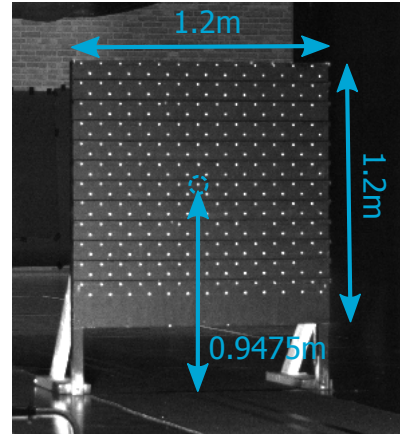


Figure 3.10: Calibration Plate and origin

The self-calibration procedure followed the one introduced in Wieneke (2005). One hundred images of the environmental turbulence level were acquired at 8Hz with the seeding rake switched on. The curtain was kept closed during the image acquisition. The self-calibration was executed in three steps, starting from 256px up to 128px with an overlap of 75%. Final dewarped image had 1215 px width and 1493 px height, with root-mean squared error of the model fitting always below 0.09px.

**Cyclist starting position and crank angle history** In order to obtain the first acquired wake in a similar fashion as Crouch *et al.* (2016a) and to have a comfortable starting position, the cyclist started from a different starting streamwise and crank angle position for each configuration. The starting position and crank angle in the dynamic cases is determined by moving the bike backward from a desired crank angle up to a starting position with a comfortable crank angle. This procedure is crucial to perform a flow-field comparison with Crouch *et al.* (2016a) and it is detailed further in section 4.4. The same starting position from rest is necessary to have a correspondence of crank angle with relative position with respect to the laser plane. If close attention had not been paid to this setup procedure, the subsequent processing could not have retrieved a phase-locked averaged flowfield, as every acquired streamwise plane would have corresponded to a different crank angle.

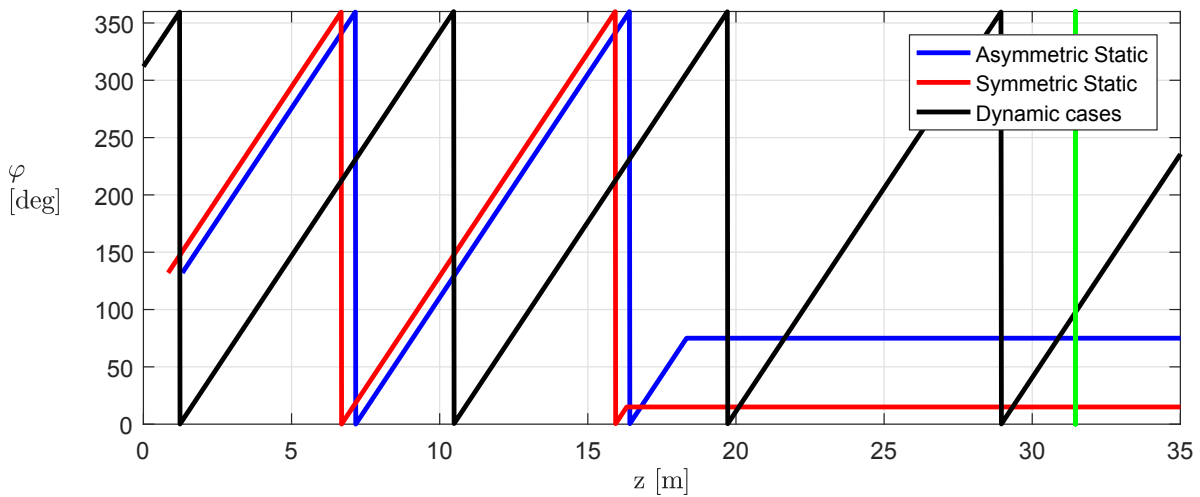


Figure 3.11: Crank angle - streamwise position correspondence for all the tests; fixed laser plane position

For the two static configurations,  $\varphi(z = 0) = -48^\circ$ , which corresponded to the same angle as in Fig.3.8, while for the two dynamic configurations  $\varphi(z = 0) = -48 + 180 = 132^\circ$ , thus with the left leg aligned with the chassis tube. The variation of the crank angle with the streamwise position is presented in Fig.3.11, under the assumption of a straight trajectory and tyre no-slip conditions. The value of z position refers to the location of the rearmost point of the rear wheel. The cyclist started from the same position with respect to the laser in both the dynamic cases. It is worthy to notice that these crank-location correspondences might differ from the reality due to an imperfect straight

trajectory during the early stages of the start.

For the two static cases, the cyclist completed less than 2 full crank cycles before coasting down. In the dynamic cases, less than 4 full crank cycles were necessary to reach the laser location. Differently from the dynamic measurements, the overall measurement time interval is relevant for the static cases. When the cyclist was in static configurations, it has been shown that he rode up to about 15m upstream of the laser plane before coasting down. All the wakes released before that station were affected by the dynamic motion of the cyclist and could not be considered in the static measurements. However, even in a conservative scenario with a wake convection velocity equal to the cyclist velocity, these dynamic wakes did not reach the measurement plane during the overall measurement interval of 5 seconds, with 2 to 3 seconds of measured planes behind the cyclist.

**Frontal area** In order to obtain information regarding the cyclist drag coefficient, the cyclist frontal area needed to be measured. The procedure to compute the cyclist frontal area is described in section 4.8. Three tests per configuration were performed, with both time-trial and upright postures in asymmetric and symmetric conditions. During each test, the cyclist proceeded towards the high-speed camera described in section 3.5, along the camera view axis, while 1000 images at 1kHz were acquired.

Table 3.2: Single test passage - typical timeline

00:00	.....	Cyclist is in starting position; Bike computer lap recording is enabled; Curtain is closed; HFSB controller STOP button just pressed.
00:35	.....	Seeding rake has fully stopped tracers production; Operator 1 gives "GO" signal.
00:36	.....	Cyclist starts pedalling; Curtain is being opened; Operator 1 enables DaVis and Pco.dimax in <i>awaiting for trigger</i> mode.
00:41	.....	Cyclist triggers the photoelectric system and thus the image acquisition; 40 frame pairs recorded at 8Hz on DaVis; 3000 images recorded at 2kHz on Pco.dimax.
00:43	.....	Cyclist has passed laser plane and starts breaking; Operator 2 restarts seeding production.
00:46	.....	Operator 1 starts saving high-speed camera images; Operator 2 stores test number and atmospheric data.
01:06	.....	Curtain is closed again; Cyclist in starting position and new lap recording enabled.
01:21	.....	Operator 2 presses STOP button on the HFSB controller.
01:56	.....	High-speed camera saving process has completed; Tracers production has fully stopped; A new test can be started.

**Test timeline** After the seeding rake is positioned within the tunnel and the calibration is completed, the experiment can be started. Multiple cyclist's passages can be performed in a series between 14 to 16 passages, before the HFSB controller stops the operations as it needs soap to be added from the discharge vessel to the main vessel. Every series starts with the seeding rake to be in operation for two minutes with the curtain closed. A minimum of five people is necessary to run the experiment: the cyclist, two experiment operators and two people responsible for opening the curtain through a string. During a series of tests, the air compressor is in continuous operation. From passage to passage, the time schematic in Table 3.2 was adopted, based on effective time recordings of the test procedure. The time units of measurements are in format [min:s].



# 4

## Data analysis and Reduction techniques

In this chapter, the discussion deals with the techniques adopted to analyse the different sets of data, so as to retrieve valuable information for the results. In particular, most of the reduction techniques allocate efforts to solve the main issue arising from a Ring of Fire implementation in comparison to wind tunnel tests: the repeatability. Repeatability concerns are even emphasised by the loss of interoperability proper of an in-house built system as the Ring of Fire setup shown in chapter 3. Data analysis techniques aim at: correcting the correspondence of plane to plane cyclist position (section 4.1 and 4.2); establishing the cyclist's speed (section 4.3); establishing the link between acquired wake and geometry memory conserved in the flow (section 4.4); processing acquired images to retrieve velocity fields (section 4.5); selecting the sample set of data (section 4.6); establishing the upstream flow influence in the drag evaluation (section 4.7); estimating the cyclist frontal area (section 4.8). Finally, the drag area computation procedure is detailed in section 4.9 together with the used criterion to identify flow structures.

### Contents

---

<b>4.1 Streamwise relocation</b> . . . . .	<b>44</b>
<b>4.2 Spanwise relocation</b> . . . . .	<b>45</b>
<b>4.3 Cyclist's speed measurement</b> . . . . .	<b>47</b>
<b>4.4 Determination of each wake position and crank angle</b> . . . . .	<b>48</b>
<b>4.5 PIV processing</b> . . . . .	<b>49</b>
<b>4.6 Test outlier selection</b> . . . . .	<b>52</b>
<b>4.7 Upstream plane choice</b> . . . . .	<b>54</b>
<b>4.8 Frontal area evaluation</b> . . . . .	<b>56</b>
<b>4.9 Drag area and flow field variables</b> . . . . .	<b>56</b>

---

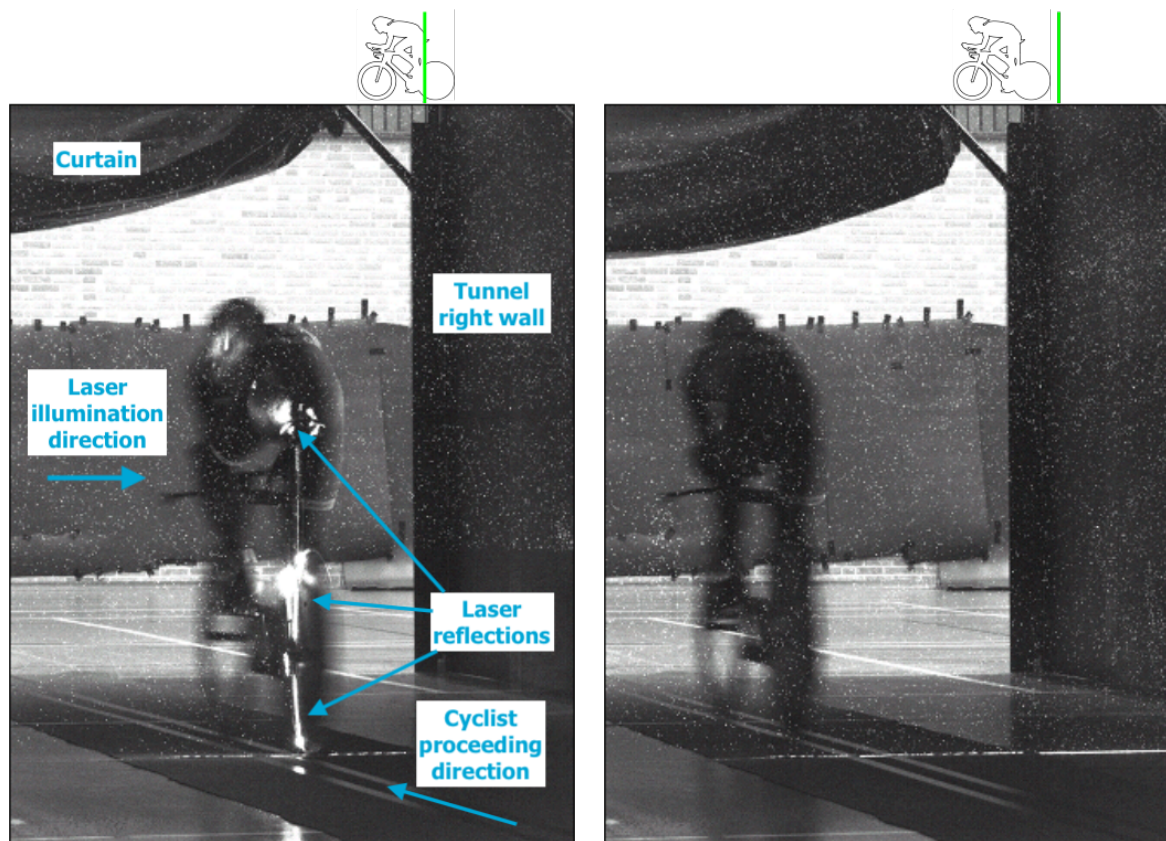
### 4.1. Streamwise relocation

In order to obtain the drag area through a control volume approach, one single downstream plane is namely enough, given that no other forces are applied after the air interaction with the cyclist and so momentum is conserved. However, if there is interest in evaluating the drag trend due to the sole momentum deficit or pressure term in the wake, planes at similar streamwise position need to be averaged across the different test passages. Moreover, this is particularly useful to retrieve information about the averaged cyclist flow field and its downstream evolution. In particular, dynamic cases wakes carry the history of the crank angle the cyclist had, so streamwise ensemble-average of the flow fields corresponds to a phase-locked average process as well.

The introduction of a synchronisation system based on a photoelectric sensor (section 3.4) aimed at reducing the challenges in operating streamwise ensemble-averaging. However, the limitations discussed in the trigger mode 1, the ones concerning the delay in mode 2 (appendix A) and the cyclist velocity fluctuations hamper the averaging process. In fact, it can be concluded that the synchronisation was not successful.

As an example, consider Fig.4.1, in which two raw pictures from the left camera in backward scattering are considered. At the top, a schematic shows the relative position of the cyclist and the laser plane, highlighted in green. Although the two pictures correspond to the same numbered image acquired after reception of the external trigger, it is clear that they are not at the same relative position with respect to the cyclist, along the streamwise direction. As a consequence, it is not possible to ensemble-average them.

Figure 4.1: Same Image number 12 after reception of external trigger; synchronisation mode 2; Time-Trial Dynamic configuration



(a) Test passage RUN047;  $z = -0.52m$

(b) Test passage RUN048;  $z = +0.14m$

Given the relatively low amount of test runs (42 for the static cases and 60 for the dynamic ones), a manual approach has been adopted to relocate the wakes with respect to each other in the streamwise direction. This consists in establishing as reference a test run for each of the four tested configurations. Visual comparison of the reference run with each first wake of the other runs helps to establish the

integer sequence shift to be applied to that specific frame. Then the same integer shift is applied to all the subsequent wakes of that specific run. After this relocation is applied to all the passages, the relative position of the cyclist with respect to the laser is within half of the spatial difference between two consecutive wakes.

As an example, Fig.4.2 shows the out-of-plane normalised velocity contour  $V_z = 0.98$  (eq.5.1), once this procedure is applied. The shown wake contour corresponds to the averaged flowfield in asymmetric static condition for  $z = 0.55m \approx 1\sqrt{A_c}$ , with  $A_c$  the cyclist frontal area. As discussed in chapter 5, the wake streamwise diffusion broadens the out-of-plane velocity contours. Therefore, the streamwise relocation avoids averaging near wakes with far wakes, thus better capturing the effective out-of-plane velocity contour width.

At this point one may question the precision of this approach and its time effort. On one hand, a streamwise interpolation of the velocity data would introduce more error given that each frame is separated by 0.125s, a similar order of magnitude as the cyclist wake characteristic time. Within this interval, not only the wake diffuses and its structures modify their strength and position, but also wakes mix due to variable planar convection and the cyclist changes his shape. On the other hand, one could suggest an automatic approach based on identifying the laser reflections on the cyclist. Nevertheless, this approach would fail in relocating the wakes in streamwise direction as during each test run the cyclist does not follow the same identical centred trajectory. The consequent perspective error would affect the streamwise relocation.

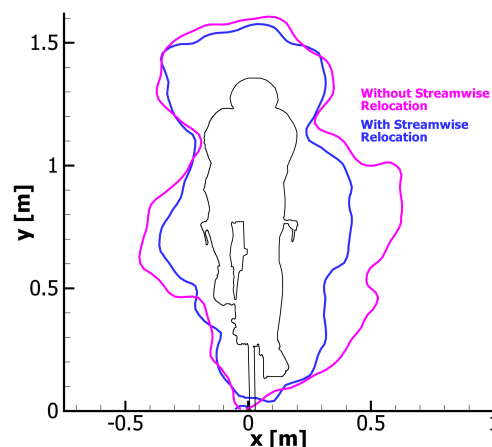


Figure 4.2: Average near wake normalised  $0.98V_z$  - Effect of streamwise relocation

## 4.2. Spanwise relocation

As mentioned, among the repeatability issues proper of a Ring of Fire experiment, one of the most important regards a spanwise variation of the cyclist position. In fact, the cyclist follows the trajectory guideline traced on the carpet within a certain margin. With a different cyclist spanwise position, the acquired wakes are in a different spanwise position as well and the streamwise averaged flow field is affected by that. In particular, this could cause difficulty in recognising the mean flow structures governing the cyclist's wake. For instance, consider Fig.4.4. Two raw images with the cyclist in a similar streamwise position are shown. Despite the little visual difference, there is more than 0.1m difference in the spanwise position of the laser reflection on the rear tyre.

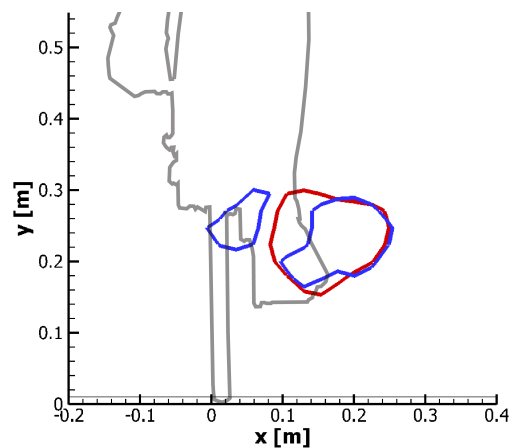
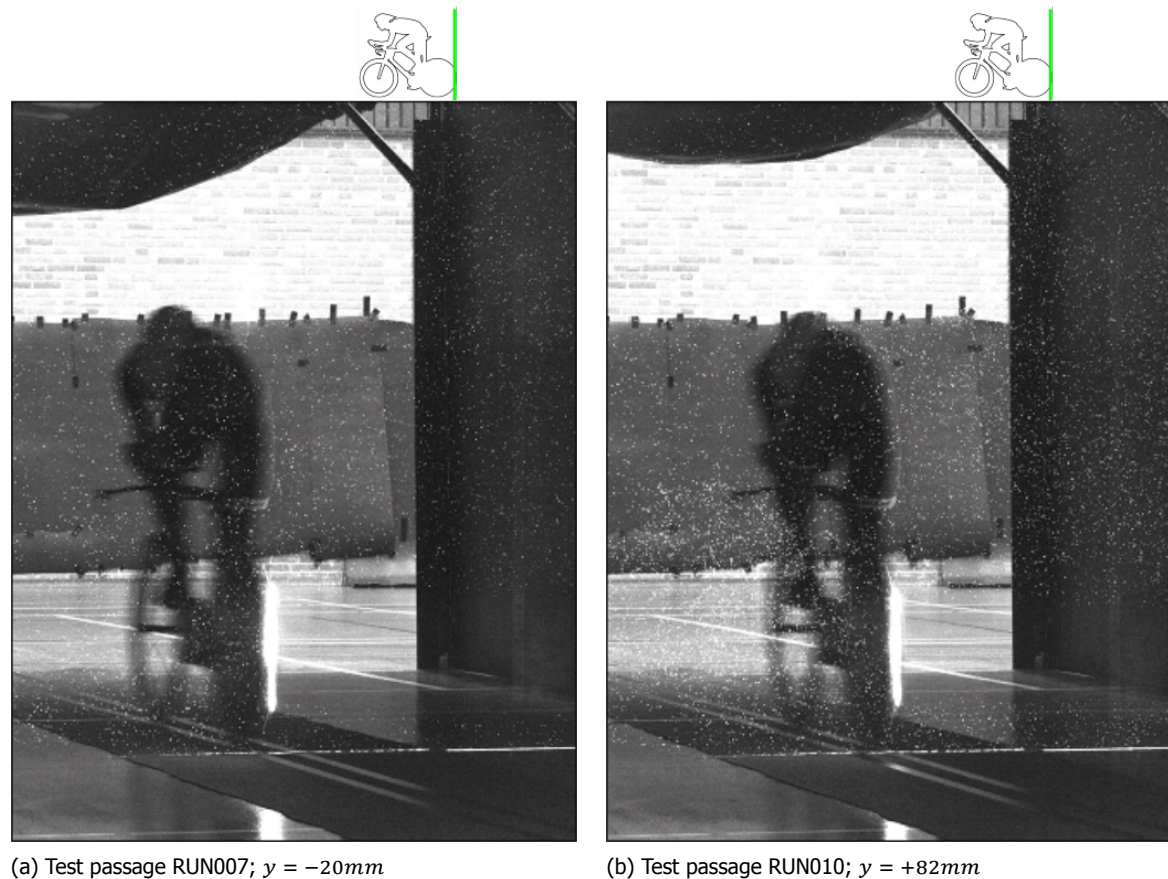


Figure 4.3:  $\bar{\omega} = -4.5Hz$  contour; right foot detail; blue: not relocated; red: spanwise relocated

The spanwise correction is particularly useful as it allows to estimate in a more trustworthy manner the peak vorticity in the flow structures. As an example, consider Fig.4.3, for the asymmetric static condition at  $z = 0.55m \approx 1\sqrt{A_c}$ . Average out-of-plane vorticity in the region of the right foot detects two co-rotating ankle-calf vortices with similar vorticity level, without application of the spanwise relocation procedure (blue lines). However, only one outer ankle-calf vortex is present in the flow topology for the asymmetric leg posture (Crouch et al., 2016a). In practice, these two vortices are the same vortex averaged at two different locations and the spanwise relocation helps obtaining the single structure (red line).

Figure 4.4: Lack of repeatability in spanwise position; Time-Trial Asymmetric Static configuration



The spanwise position of the cyclist is computed with the procedure shown in Fig.4.5. The spanwise relocation consists of the following steps:

- All the images for each test run are corrected based on the camera calibration. In this way the images are mapped on real dimensions, provided that the camera calibration is correctly performed;
- For each test run the image with the laser illuminating a portion of the rear wheel is chosen from the sets of the backward scattering camera frames;
- On that image, the coordinate of the tyre portion illuminated by the laser is stored. The reason why the tyre coordinate is chosen is based on the fact that the lenticular disc wheel has got a concave shape, so its planar coordinate varies with the height. An example of this procedure is shown in Fig.4.5: the figure is a zoomed raw image with an intensity scale inverted with respect to Fig.4.4b, among the others;
- The position is determined with a resolution based on the pixel size, so up to 1.5 mm. On average, the cyclist passes at 1 mm from the trajectory centre with maximum fluctuations  $\pm 150$  mm. Thus, the position resolution is between one and two order of magnitude lower than the spanwise trajectory error;
- The flow field velocity data are shifted with the stored coordinate. In this way all the wakes are within a region such that  $x = 0.00m$  corresponds to the left portion of the rear tyre;
- As the spanwise error is not an integer multiple of the vector pitch, the velocity data are on different grids. Therefore, they are finally linearly interpolated on a common grid, retaining the same vector pitch as the acquired instantaneous wakes.

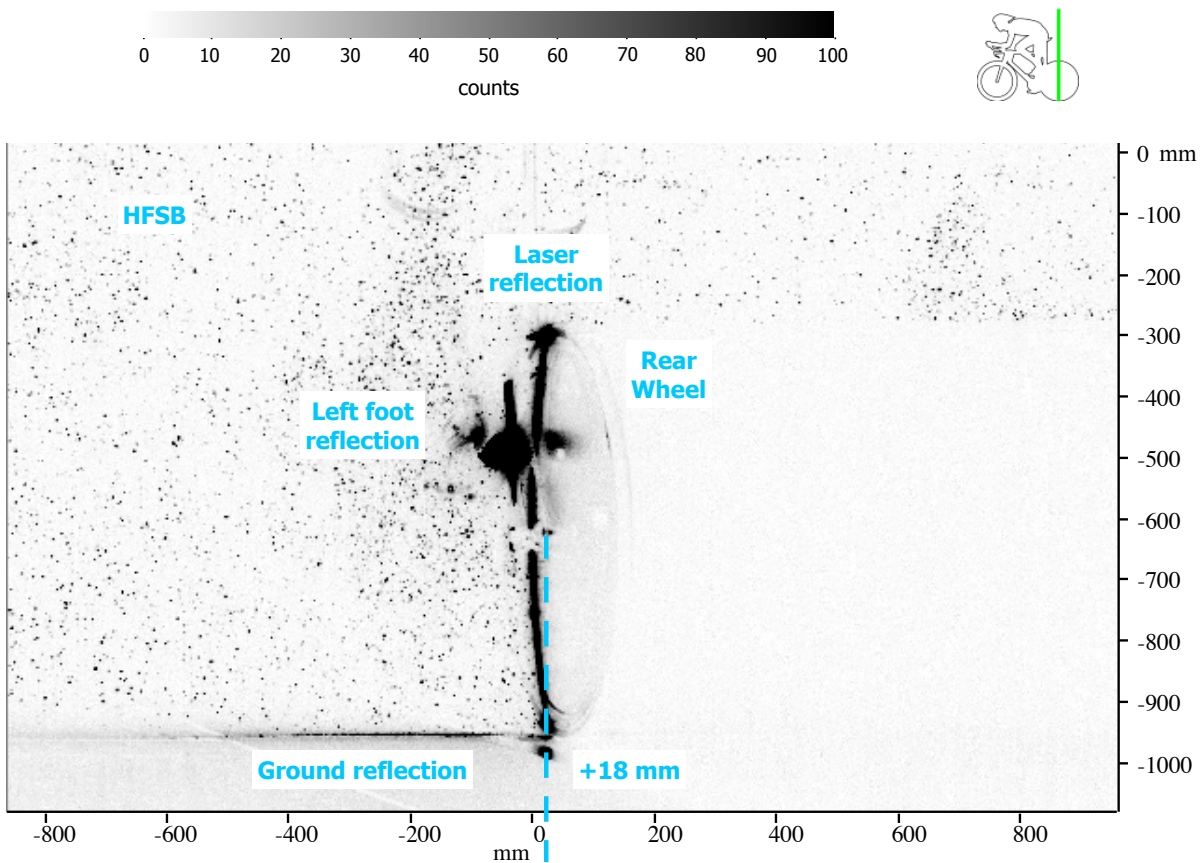


Figure 4.5: Spanwise relocation on corrected image; zoomed rear wheel

### 4.3. Cyclist's speed measurement

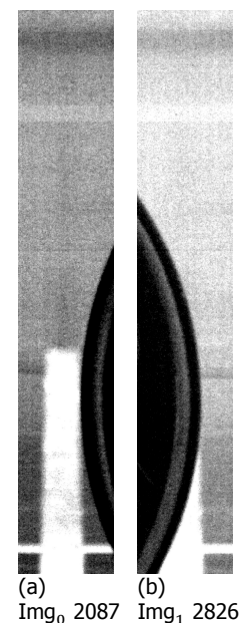
**High-speed camera** With the high-speed camera, only one cyclist speed value is obtained for each test run. The following procedure is adopted:

- The two nearest neighbour figures with the foremost and rearmost bike point closer to the silvered tape on the floor are selected;
- The difference between the two images number is computed and converted in time, given an acquisition frequency of 2kHz;
- The average velocity is then computed based on the known bike length and the obtained elapsed time.

This measurement allows to evaluate the cyclist's speed at a location more than 5m far from the laser plane. For the purpose of drag evaluation, this speed must be assumed constant along the same passage. As a consequence, drag inaccuracy can result from this assumption if the cyclist's speed fluctuations are large. This is particularly important for the static cases, as the cyclist decelerates for more than 12m before the laser plane (Fig.3.11).

Despite this inaccuracy, this method allows for evaluating the cyclist's speed with a maximum inaccuracy equal to 0.006m/s, or 0.1% of the his speed. Moreover, one could argue that a perspective error can harm the results: actually, even if a perspective error occurs, this would be the same for the front and the rear image, without affecting the difference between the images. An example of the velocity analysis is shown in Fig.4.6. In this case, the cyclist velocity is:

Figure 4.6: Sample start and end frames



$$U_c = \frac{L}{\frac{\text{Img}_1 - \text{Img}_0}{f}} = \frac{1.684\text{m}}{\frac{2826 - 2087}{2000\text{Hz}}} = 4.558 \pm 0.006\text{m/s} \quad (4.1)$$

**Magnetic sensor** As discussed in section 3.5, six magnets are placed on the rear wheel of the bike and scanned by a magnetic sensor to retrieve information about displacement and velocity. The Garmin Edge ®810 stores these data with a frequency of 1 Hz through a confidential algorithm. As the velocity is updated every 0.349m, it is clear that the time resolution with the magnets is higher than with the high speed camera, which averages the velocity along the entire bike length, 1.684m. The stored data are downloaded in .fit file format, read through the software GoldenCheetah and converted to .csv format.

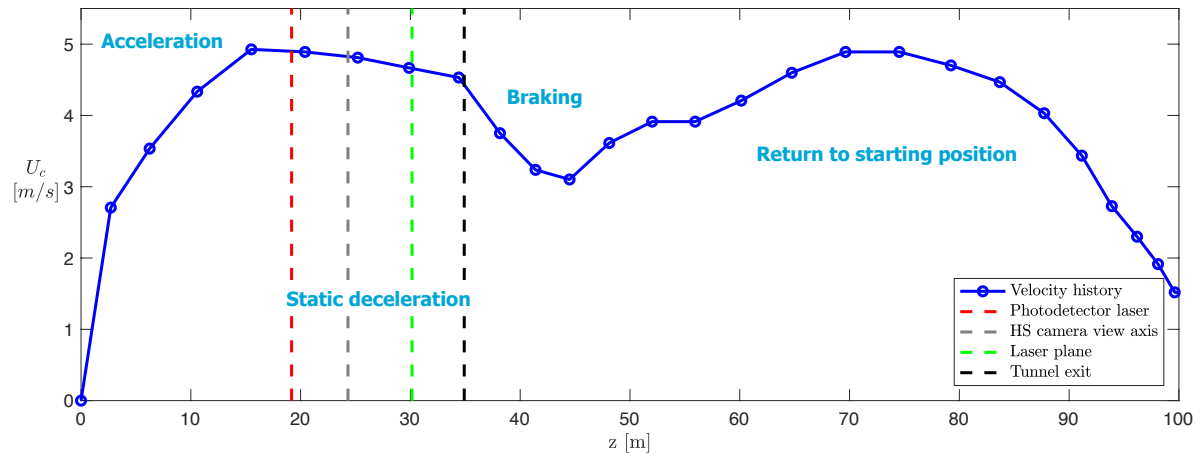


Figure 4.7: Velocity history of a typical static test run

When reading the data, the main challenge is posed in distinguishing which are the data referring to a real test run. In fact, during the lap recording, the cyclist firstly accelerates, then brakes and accelerates again to position himself for a new lap. During static measurements, the cyclist coasts down before breaking. Moreover, before starting a new lap, time is still being recorded on the old lap, resulting in sets of null velocities from lap to lap. This would result in a set of velocity-time curves with two peaks, the first higher than the second one. Between the two peaks, braking can cause a single null velocity recording in some cases: this does not affect the results as braking occurs after the laser sheet is passed. An overview of a typical test velocity trend for one static case lap is shown in Fig.4.7, where the mentioned zones are visible. The  $z$  coordinate refers to the space travelled by the rearmost point of the bike, assuming a straight path. In the dynamic cases, the static deceleration zone is substituted by a nearly constant speed zone.

Every  $60^\circ$ , a magnet is read and the velocity and displacement information updated. As the distance travelled from magnet to magnet is indicated by the user during the setup of the bike computer, a wrong placement of the magnets can cause misreadings on the velocity. With  $60^\circ$ , the nominal displacement is equal to 0.349m. Now suppose that one magnet is placed at  $61^\circ$  from the previous read and so  $59^\circ$  from the next one. This angular misalignment can cause the first displacement to be in reality equal to 0.354m and the second to 0.320m. With  $U_c=5\text{m/s}$ , in the first case the cyclist travels 0.354m in 71ms and in the second 0.343m in 69ms. In the first case a velocity of 4.92m/s would be predicted, while in the second case it would be 5.06m/s, causing a bias on the real velocity of about 1.5%. However, as the speed is stored with 1Hz frequency, with  $U_c=5\text{m/s}$  there would be 14 readings of the magnets between each stored speed and the error would decrease.

#### 4.4. Determination of each wake position and crank angle

In section 4.1 the difficulty in establishing the historical relation between the captured wake and the cyclist's configuration has been mentioned. In section 3.6, it was possible to reconstruct the crank

angle the cyclist had before crossing the laser sheet (Fig.3.11), based on the assumption of wheel non-slipping conditions and straight trajectory. The captured wakes differ streamwise because of two different processes: the streamwise diffusion and turbulent mixing they undergo and the different cyclist's shape history they carry. These effects make cumbersome answering where each wake is relatively to the cyclist and when it was released. The first question could be exactly answered by using an accurate tracking system in the indoor facility, while in the current experiment the streamwise wake position is simply based on the ratio of the average cyclist velocity at the laser location and the acquisition frequency.

The second question is impossible to be answered in an exact manner in the author's opinion. In fact, the relation between the captured wake and the cyclist's shape history is strongly based on the wake convection velocity. Crouch *et al.* (2016a) determine a value of the convection velocity based on identifying the main vortical structures by the swirling strength criterion (Zhou *et al.*, 1999) and averaging their streamwise velocity with a weight based on the relevance of each vortex in the wake overall shape. Based on this, Crouch *et al.* (2016a) identify a convection velocity depending on the crank angle and assume a value of  $0.61U_\infty$  to establish the phase lag between the current cyclist crank angle and the one in the wake. This approach can be used in this current experiment as well. However, its approximation becomes more inaccurate for the later captured wakes, i.e. the first ones released by the cyclist. In fact, given the different convection velocity of each vortex, the more the time the wake had to evolve the more it has mixed with earlier or later released wakes, obscuring the crank angle information.

In this experiment the convection velocity assumption has been used especially for the first wake. During the cyclist's starting position setup, it was decided to locate the bike with  $\phi=75^\circ$  at an upstream position with respect to the laser plane to have as the first acquired wake the one released at that crank angle and at a distance similar to Crouch *et al.* (2016a). By moving the bike backward along a straight trajectory and without braking, it was possible to decide the starting position and crank angle that would have provided a better comparison to Crouch *et al.* (2016a) and to a certain extent to Shah (2017), Spoelstra (2017) and Terra *et al.* (2016).

Moreover, the convection factor is applied to retrieve the cyclist velocity to be used in the evaluation of the drag area. Based on the magnetic sensor data, the cyclist's speed at wake  $n$  is interpolated at the time  $t_l - conv_f \cdot n \cdot \Delta t$ , with  $t_l$  the time instant when the rearmost bike point passes the laser,  $\Delta t$  the inverse of the acquisition frequency and  $conv_f$  the convection factor. The latter is equal to 0.61 for the dynamic case, 0.57 for asymmetric static and 0.69 for symmetric static, based on the results of Crouch *et al.* (2016a) for the reduced frequency  $k = 0.115$ .

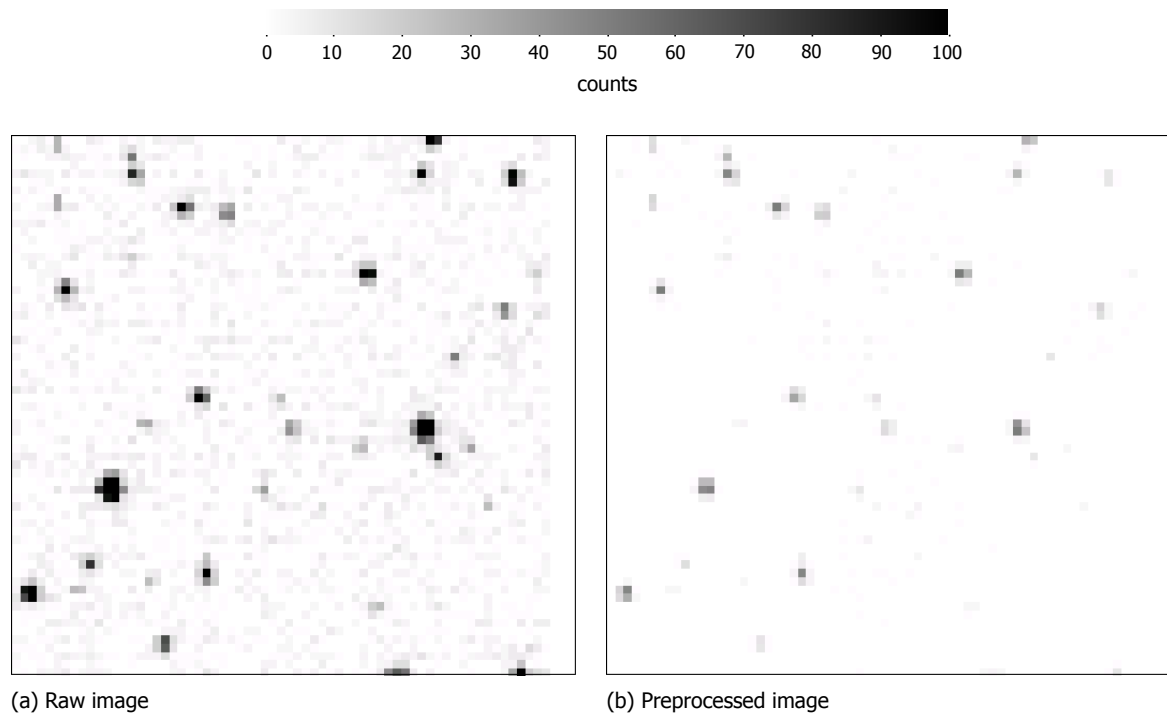
## 4.5. PIV processing

**Image preprocessing** Image preprocessing has got a relatively important value in affecting the final results. On one hand, given the probabilistic nature of the cross-correlation algorithm, PIV processing is generally capable of retrieving velocity fields even without any image preprocessing. On the other hand, Raffael *et al.* (2007, p. 139) mentions that image preprocessing is necessary to bring the particles intensity to a similar level, so that they contribute equally to the correlation signal and do not introduce noise due to non-uniform illumination. Therefore, improvement on the signal-to-noise ratio (SNR) of the measurement technique can be expected, thus its robustness. As larger noise level decreases the relative size of the highest correlation peak with respect to the additional correlation function peaks (Willert and Gharib, 1991), a measurement of the PIV SNR is based upon the ratio of the highest peak with respect to the second highest one.

Raw images are characterised by a certain background intensity level that produces background noise in the pixel light intensity. Although the presence of background noise interferes little with the RMS error of the PIV measurement as shown in Raffael *et al.* (2007), it is good practice to remove the background noise so as to improve the measurement SNR, especially for the second exposure of each camera, where background intensity is closer to particle intensity. Moreover, laser reflections can be diminished. Differently from typical wind tunnel measurements, applications of PIV on transiting objects require to subtract the background noise computed over a limited amount of images to all the images. This is due to a difference of pixel intensity image to image caused by the transiting

object; thus, the minimum is computed over the first images of the environment before the passage of the cyclist. Furthermore, the application of two different trigger modes for the image acquisition synchronisation varies the amount of images used to evaluate the common minimum intensity level: in mode 1 (Fig.3.6a), about 12 images are acquired before the tested object is within the camera's solid angle, while in mode 2 (Fig.3.6b), just three images. After removal of the minimum, two filters are applied to vary the relative intensity of the pixels: a sliding minimum filter and a normalisation filter.

Figure 4.8: Image preprocessing effect on a  $64 \times 64$  px window



Because of the described limitations in the removal of the background, the acquired images are subjected to intensity fluctuations due to the variation of the distribution of light reflections in the background. This is mainly ascribed to the fact that the tested object transits in the background of the FOV and that the room light could not be switched off for safety reasons. The sliding minimum filter tries to remove the remaining background intensity fluctuations by evaluating the minimum in a sliding window of a fixed amount of pixels. If the window were smaller than the tracer, its intensity would be harmed. Therefore the window should be large enough to avoid it. At the same time a too large window would reduce the effect of subtracting the sliding minimum, as it would be closer to repeat the same operation as the background removal. Therefore a 10px window has been chosen, as large as twice the mean particle diameter of the larger tracers.

Together with a sliding minimum, a local normalisation filter is applied based on the suggestions of [Westerweel \(1993\)](#). This filter computes two sliding maximum, the first on a local window and the second over a window ten times larger. The ratio of local to global is then multiplied to each pixel. The intent is to normalise the particles intensity so that the tracers contribute to the PIV processing in a more equal manner. This is particularly necessary with the current experiment. In fact, the in-house built seeding rake has larger fluctuations in the particles diameter. As a consequence, their diameter fluctuation causes intensity fluctuations proportional to  $d^2$  ([Adrian and Yao, 1985](#)), as they lie in the geometric scattering regime. Moreover, the intensity fluctuations are further enhanced by the variable laser intensity over the laser width.

The window dimension has been chosen equal to 10px. The 10px window has been chosen based on the percentile PIV SNR in the cyclist wake, shown in Fig.4.9. The vertical axis SNR value indicates the higher SNR in the corresponding interrogation windows indicated on the horizontal axis. For instance, consider the point at 2% for all the curves: without application of the filter (red curve) 111 interrogation

windows (2% of the overall windows in the FOV) present a SNR lower than 3, while in all the other cases it is above 3.

It can be concluded that the application of the filter has always a positive effect on the SNR, especially considering that almost 100 of the evaluated vectors have got  $\text{SNR} \leq 2$  without the filter. However, the filter performance decreases with the filter length after a length equal to 10px.

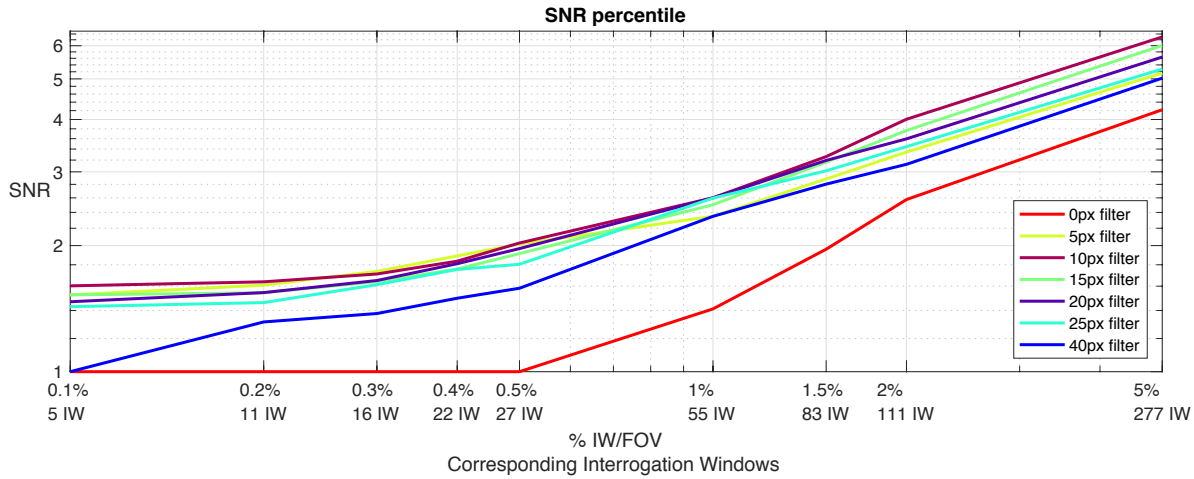


Figure 4.9: Percentile SNR trend with choice of normalisation filter window - logarithmic scaled axes

**Cross-correlation** In order to obtain velocity flow fields from the preprocessed images, classical stereo cross-correlation was adopted. Processing is performed on DaVis software 8.4.0.2. The interrogation process is repeated over three passes for interrogation window size of 96px and decreasing up to 64px. Most of the tests could have been processed with a window size of 48px without excessive resulting noise. However, low level of seeding density in some tests did not allow to apply the same window size, reason why 64px window was kept for consistency. The final window size value of 64px was chosen based on a similar analysis on percentile SNR variation with window choice. The influence of the seeding density on the SNR is due to the contribution of the image density, the in-plane loss-of-pairs factors and out-of-plane loss-of-pairs factor as described by [Keane and Adrian \(1992\)](#).

It must be pointed that the dissimilarity of seeding density is a proper drawback of the Ring of Fire project because of the use of a seeding system not specifically designed for a Ring of Fire application. As a consequence, despite an average particle per pixel ( $ppp$ ) level about 0.01, local regions have been found to have  $ppp \leq 0.004$ , constraining the interrogation window size and thus the experiment Dynamic Spatial Range ([Adrian, 1997](#)). A correlation between the  $ppp$  level and the PIV signal-to-noise ratio is proposed in section 4.6. Moreover, provided that a large number of windows does not have a  $\text{SNR} \leq 2$ , the mean momentum deficit contribution to the drag area was found unaffected by the interrogation window size.

Finally, it is relevant to highlight that the particle per density level does not vary among upstream and downstream planes, but it stays rather constant along the same test passage. This is a consequence

Table 4.1: Stereo cross correlation processing parameters

Processing		
Passes	3 x 96 px $\rightarrow$ 3 x 64 px	
Interrogation window	Image world 64 px	Real world 94.7 mm
Overlap	75%	
Vector pitch	Image world 16 px	Real world 23.7 mm
Particles per window	45 bubbles	
Weighting	Rounded gaussian over 128 px	
Multi-pass processing	Universal Outlier Detection over 5x5	

of a good setup procedure in placing the seeding rake within the tunnel (section 3.6).

In the PIV processing setup, the multi-pass selection permits to perform the cross-correlation over similar window size with a sliding relative movement of the window towards the vector direction computed from the previous pass. This increases the amount of correlated particles and thus the accuracy on the displacement estimation. For the final passes, the pixel light intensity is interpolated through a bi-spline 6 points reconstruction rather than a bilinear one. Moreover, the universal outlier detection median filter from [Westerweel and Scarano \(2005\)](#) is used over a 5x5 region to replace the vectors which are out of three times the region standard deviation.

Regarding the grid size, interrogations window are placed with 75% overlap, so that the spatial resolution of the resolved vectors is increased without a reduction in the seeding density per window. Each window is weighted with a round Gaussian, so that the particle displacement is averaged over a window with a double size than the selected window, and with a Gaussian-shaped weight. This gives predominance to the particles displacement in the local centroid of the Gaussian. A rounded weighting increases the accuracy in the determination of the mean displacement without biasing towards a certain displacement direction. A summary of the processing settings is presented in the table in [Tab.4.1](#).

**PIV postprocessing** After being processed, the vectors in each interrogation window are questioned through a median filter based on the universal outlier detection filter developed by [Westerweel and Scarano \(2005\)](#). The settings are equal to the postprocessing technique used among the passes during the cross-correlation. For each interrogation window, the computed velocity component for each of the three direction is compared with respect to the median over a 5x5 windows region and its standard deviation. In the universal outlier detection version, the median residual of the velocity as defined in [equation 4.2](#) is used to normalise the residual of the postprocessed window vector. Then the vector replacement occurs whether the vector component is out of the interval of median with added two standard deviation but within the range with three standard deviation. The replacement considers either the highest three secondary cross-correlation peaks, repeating this iteratively three times.

$$r_m = \text{median}(|U_i - U_m|) \quad (4.2)$$

The median rather than the mean value of the residual is used, as outliers would strongly affect the value of the mean, while this is not the case with the median.

Considering an overlap of 75%, the choice of a filtered region of 5x5 is large enough that not all the windows in the region are correlated by sharing a certain amount of particles. In fact, such an overlap implies that four window aligned in one direction shares at least one fourth of the particles for the evaluation of the vector displacement. If on one hand a smaller filtered region would reduce the effectiveness of the filter, on the other hand a too large region could replace correctly computed displacements.

No other postprocessing technique is applied apart from filling empty windows through interpolation. As they mostly occur on the edges of the FOV, which are discarded in the drag computation due to their large uncertainty, the windows filling is irrelevant to the final results. In fact, for the drag area evaluation, the images are cropped to an area 1.73m wide and 1.76m high, so as to exclude the ground and the upper part of the curtain. Moreover, a rectangular mask is applied in the bottom left corner. In this region, the seeding density is generally much lower than in the rest of the domain ([Fig.4.11](#)) as it is in the vicinity of the laser cut-out.

## 4.6. Test outlier selection

For the purpose of averaging flow fields and drag area, two different criteria have been applied in order to exclude test runs which were outliers with respect to the ensemble. The first criterion is based upon the seeding density. Given its influence on the image density and loss-of-pairs ([Keane and Adrian, 1992](#)), low seeding tests were excluded based on a comparison of the planes average of 5<sup>th</sup> percentile SNR in the plane, which corresponds to more than 250 vectors. In general, it is extremely simple to identify the seeding outlier as their 5<sup>th</sup> percentile SNR is below 2. Potentially, these outlier tests are

not bad tests per se, but rather they require larger interrogation window and therefore lower spatial resolved wake.

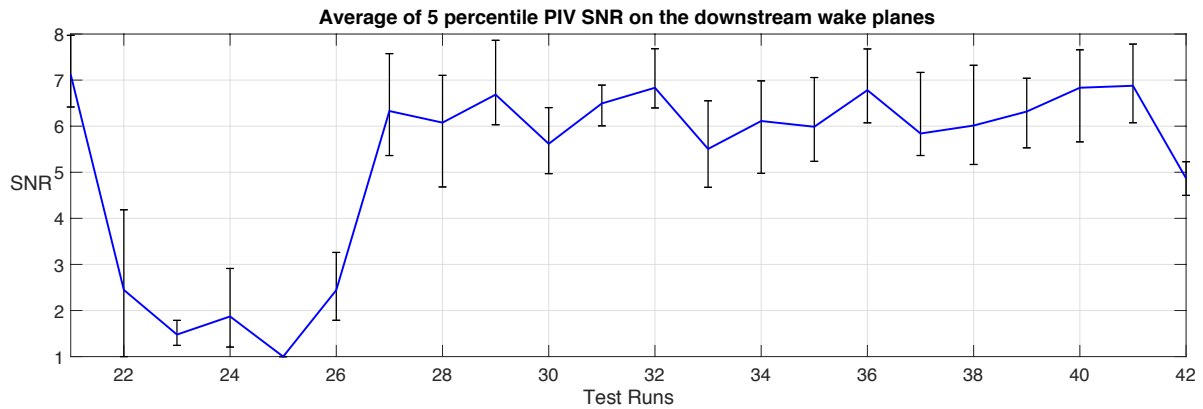
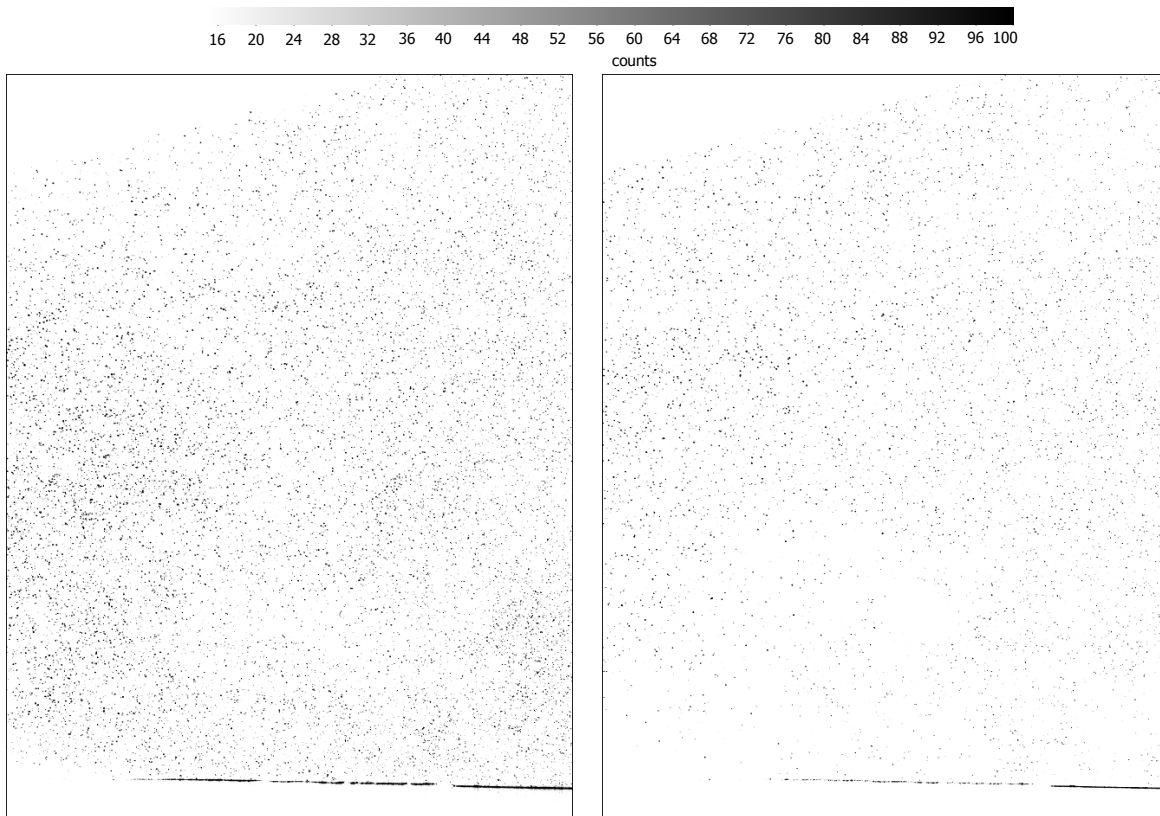


Figure 4.10: Planes average of 5 percentile SNR for each test run in symmetric static configuration; uncertainty bars indicate minimum and maximum

Figure 4.11: Seeding density comparison between a typical *ppp* level and an outlier - Raw images



(a) RUN029;  $p_{Air}/p_{He} = 1.67$ ,  $ppp = 0.011$

(b) RUN023;  $p_{Air}/p_{He} = 1$ ,  $ppp = 0.005$

This has been particularly relevant for five tests (runs 22-26) performed in symmetric static configuration. During those tests the ratio of air pressure to the helium one was equal to 1, rather than equal to 1.67, as indicated on the HFSB controller during all the other tests. The planes average 5<sup>th</sup> percentile SNR in the wake of the cyclist is shown in Fig.4.10 together with bands indicating the upper and the lower values. Moreover, a direct seeding comparison and the relative *ppp* level of the test run 29 and 23 are shown in Fig.4.11a and 4.11b respectively. Notice the relation between the particle per

pixel density and the percentile SNR.

The second criterion was based upon the cyclist velocity, by excluding the tests in which the cyclist had a velocity out of the three times standard deviation range from the mean cyclist velocity value. Although this should not cause large difference in terms of computation of drag area, provided that there are no aerodynamic effects related to a Reynolds number difference, this has got an effect in the averaged wake flowfield shape and its flow structures.

#### 4.7. Upstream plane choice

In order to evaluate the drag area, momentum deficit is computed with respect to the undisturbed flow. As described in section 2.2, in the Ring of Fire measurement this assumes an uttermost importance in comparison to wind tunnel measurements, where the momentum deficit is computed only at the downstream plane. This is a consequence of the assumption that the wind tunnel turbulence intensity is negligible. In the work of Spoelstra (2017), the upstream flow field  $u_i$  used for the drag area evaluation (eq.2.6) consisted of an average of the velocity planes acquired in front of the cyclist. In this section that choice is discussed, justified and compared with the effect of the choice of a single upstream plane.

There are two constraints to be respected in the choice of the upstream plane. Firstly, any part of the bike should not be visible in the image, otherwise it would mask the measurement domain. The 0.400m long bike handlebar is the first to enter the solid angle of one of the two cameras when it is at 3.5m from the laser plane, so when the bike rearmost point of the back wheel is approximately at 4.8m from the laser plane, or the foremost point of the front wheel is at 3.2m. With this constraint, the first 12 planes in static conditions can be considered, while only the first 4 planes in dynamic conditions, given the different triggering mode.

Secondly, the upstream flow should not be influenced by the bike front pressure. Estimating a potential flow analysis based on a cylinder, this phenomenon would have as characteristic length  $\mathcal{L}$  the overall bike length, different from the wake diffusion characteristic length. With such an approach, the last two planes captured before the handlebar is visible would be characterised by a  $C_p > 0.05$  (Fig.4.12), thus it would be debatable to assume no influence from the cyclist pressure field. Given the different triggering mode, this would coincide to have only two upstream planes in the dynamic cases. In Fig.4.13 the sole drag area evaluation based on momentum deficit is presented for a specific downstream plane in asymmetric static configuration. Along the z axis the distance from the front part of the cyclist is increased and so the upstream plane relative to such a distance is used to evaluate the environment momentum. Given the influence of the pressure field in front of the cyclist, a flow component in the cyclist direction is induced and so the closer the captured plane the lower is the drag area. Across the different test runs, the standard deviation of the momentum deficit is evaluated and it is noticeable how the further planes have generally more momentum deficit fluctuations. This could be expected, given that it is more likely that an inlet plane closer to the tested object is less affected by other momentum sinks and sources in the application of the control volume approach. By comparing Fig.4.12 and Fig.4.13, it is worthy to underline that the choice of a potential flow cylinder with the same diameter as the bike length is a reasonable choice in predicting the pressure influence of the cyclist on the upstream planes.

Based on Fig.4.13, additional considerations can be drawn. First of all, evaluation of the sole momentum deficit needs to disregard the upstream planes closer to the cyclist. In the current experiment, the two closer planes have not been taken into account. Secondly, the choice adopted in Spoelstra (2017) is considered. The use of an averaged up front flow field for each of the downstream planes within the same run looked a reasonable choice, especially considering the effect on the drag area standard deviation across the test runs. In fact, with a fixed downstream plane, an averaged up front flow field retrieves a lower drag area standard deviation than a specific chosen upstream plane. Together with that, a physical explanation supports further the choice of an averaged upstream flow: the large scale environment flow structures have very long characteristic times so within a time frame corresponding to ten images (1.25s) they barely evolve.

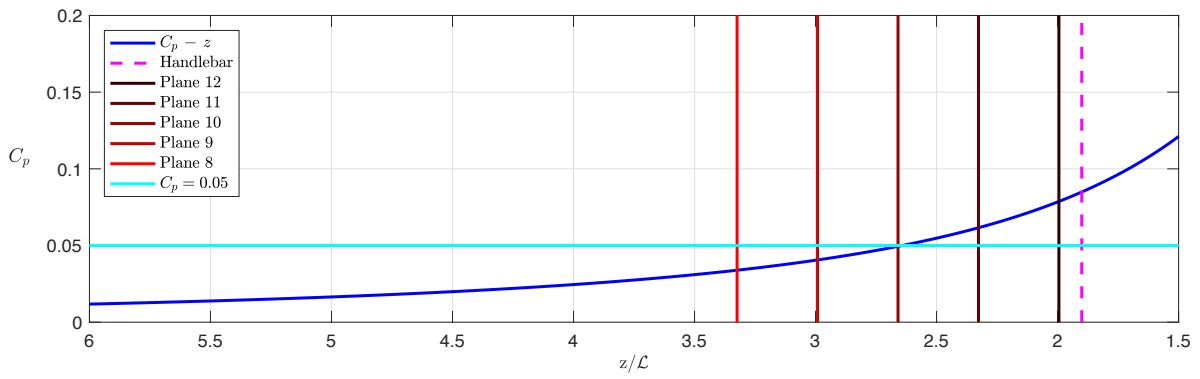


Figure 4.12: Potential flow for a cylinder  $C_p - z/\mathcal{L}$  with  $\mathcal{L} = 1.684\text{m}$

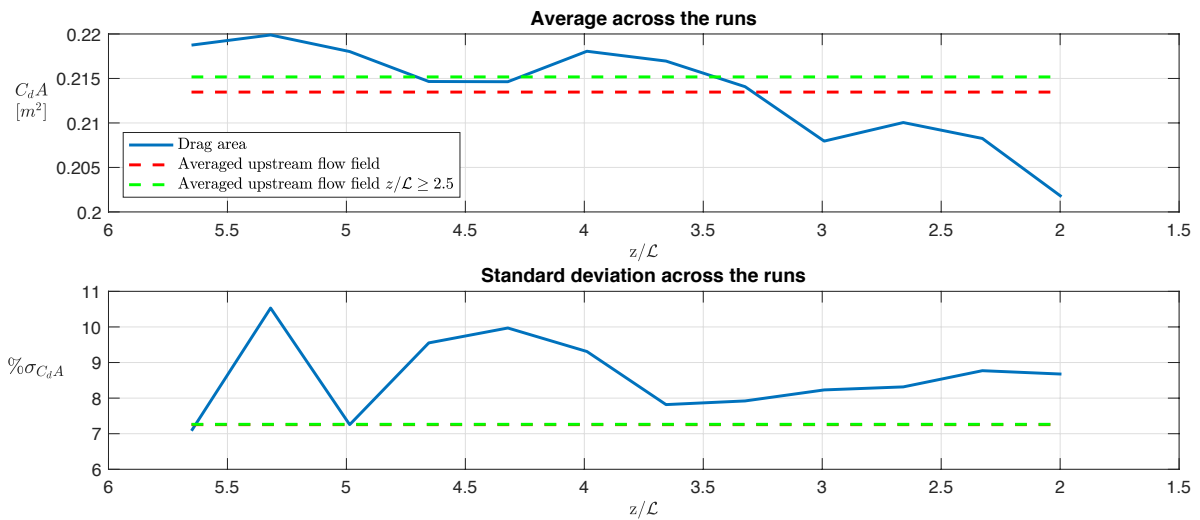
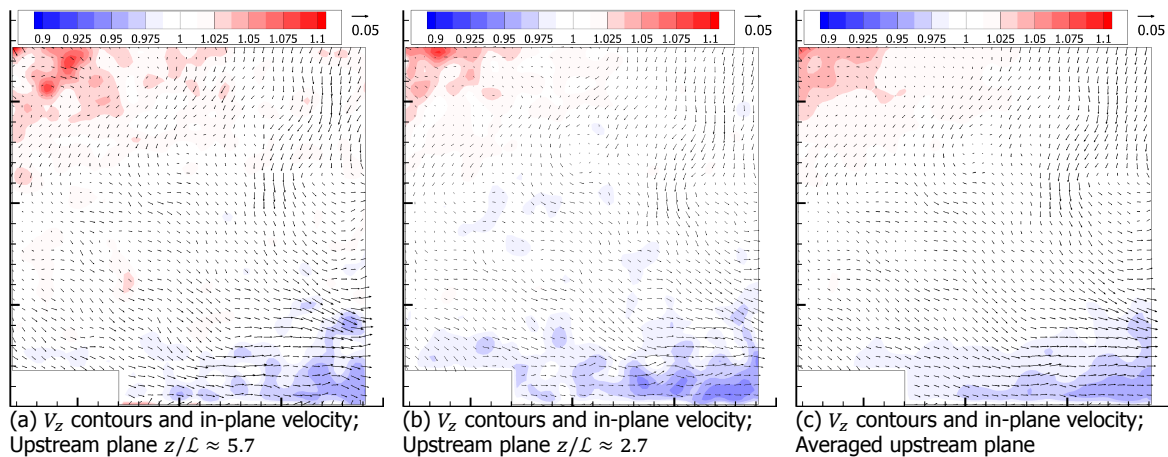


Figure 4.13:  $C_{dA}$  momentum deficit variation with the choice of the upstream plane - asymmetric static configuration

Figure 4.14: Upstream flow field for a single typical test run; axes ticks every 0.1 m



To further support this argument, consider Fig.4.14. A typical environmental flow field is depicted with out-of-plane contours (eq.5.1) and in-plane vectors of normalised velocity. In Fig.4.14a, the plane  $5.7\mathcal{L}$  far from the cyclist front stagnation is shown, while Fig.4.14b presents the flow at  $2.7\mathcal{L}$ . As suspected, both the out-of-plane and the in-plane velocity components barely vary in the 1.25s time

frame. Therefore, the averaged velocity in 4.14c can provide a better representation of the upstream flow and, as noticed, a more precise drag evaluation.

Furthermore, notice that the environmental fluctuations are of the order of 1% of the cyclist speed, with peaks between 5% to 10%. Their effect on the drag evaluation is further discussed in chapter B.

#### 4.8. Frontal area evaluation

Based on the acquired frontal images through the use of the high-speed camera, it is possible to measure the frontal area of the cyclist in order to retrieve his drag coefficient. As described in section 3.6, cyclist's pictures were acquired in both upright and time-trial configurations for symmetric and asymmetric conditions. Debraux *et al.* (2011) propose three different approaches on the evaluation of the cyclist drag area, with the method of weighting photographs and the method based on CAD considered as the most reliable. Because of its simplicity, the latter was used in the current project with the difference that the software used is a professional vector graphics software rather than a CAD one.

Among the 1000 acquired images with the cyclist running along the camera view axis, the one closer to the camera plane and with the straighter trajectory is chosen. The picture is loaded on the vector graphics software and the user manually traces the cyclist's frontal area contour (Fig.4.15). Once the contour is built as a closed single path, the area within the contour is computed. If necessary, additional holes within the main contour are removed from the area computation. The obtained area value is based on the software paper size dimensions. In order to obtain the real frontal area, a horizontal straight line is traced as long as the bike handlebar. By knowing the line dimension and the handlebar width (400mm), the following equation is applied:

$$A_{real} = A_{sof} \cdot \left( \frac{h_{real}}{h_{sof}} \right)^2 \quad (4.3)$$

with  $A_{sof}$  and  $h_{sof}$  the area and the handlebar width dimensions in the graphic software. The process is repeated three times with a different set of photographs for each configuration. Then, the average is used as the cyclist's frontal area.

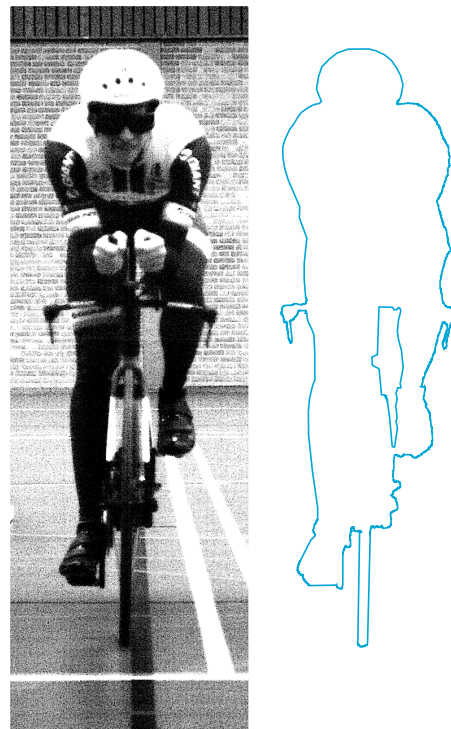


Figure 4.15: Time-Trial Asymmetric Cyclist's frontal area

#### 4.9. Drag area and flow field variables

In this section a summary of the field variables of interest and their contribution to the drag area is presented.

**Momentum deficit term** As discussed in chapter 2, the momentum deficit is the main contributor to the drag area determination. The velocity vectors obtained by the PIV measurements are used to compute the drag area momentum deficit as in equation 2.8. As discussed in section 4.7,  $u_i$  is obtained through average of the flow fields in consecutive upstream planes for each test passage. The influence of the environmental fluctuations on the drag area results is further discussed in appendix B.

The cyclist's speed is based on the measurement through the magnetic sensors. This choice is based on the fact that the magnetic sensor speed was found to have an inaccuracy lower than 3% of the speed measured with the high speed camera for the same location. As an addendum, it allows to compute the cyclist's drag area for each streamwise wake with the speed the cyclist had when the

wake was released, based on the discussion in section 4.4.

Since the cyclist's speed is not constant along the same passage, this has got an important effect on the drag area, as the latter is inversely proportional to the former (provided that the same measured upstream and downstream flow is used). In Fig.4.16 the mean momentum term of the drag area for the dynamic time-trial posture is plotted. The two curves refer to the evaluation of the drag area with the two different methods to estimate the cyclist's speed. The position  $z \approx 12.5\sqrt{A_c}$  corresponds to the cyclist's position at the high-speed camera location. As mentioned in section 4.3, in dynamic conditions the cyclist's speed keeps increasing up to the point when he passes the laser. Therefore, for  $z < 12\sqrt{A_c}$  his speed is higher than the one computed at the high-speed camera location, thus its drag area is lower. Conversely, for  $z > 12\sqrt{A_c}$ , the acquired wakes correspond to the time instants when the cyclist had still not reached the high-speed camera, thus his speed was lower than the one measured with the camera. Coherently, the estimated drag area is higher than with the speed from the high-speed camera.

Notice that the drag area difference for the farthest plane is about 5%, as visible in Fig.4.16 and that the streamwise standard deviation of the drag area is not affected by the chosen speed measurement technique. Therefore, the assumption of a streamwise constant velocity hampers the accuracy of the determination of the mean drag area, but not its precision. However, the farthest wakes should be considered with care even with the speed from the magnetic sensor. In fact, the approach adopted by the current author in assigning a certain cyclist's speed to each wake, as described in section 4.4, is questionable especially for the farthest wakes.

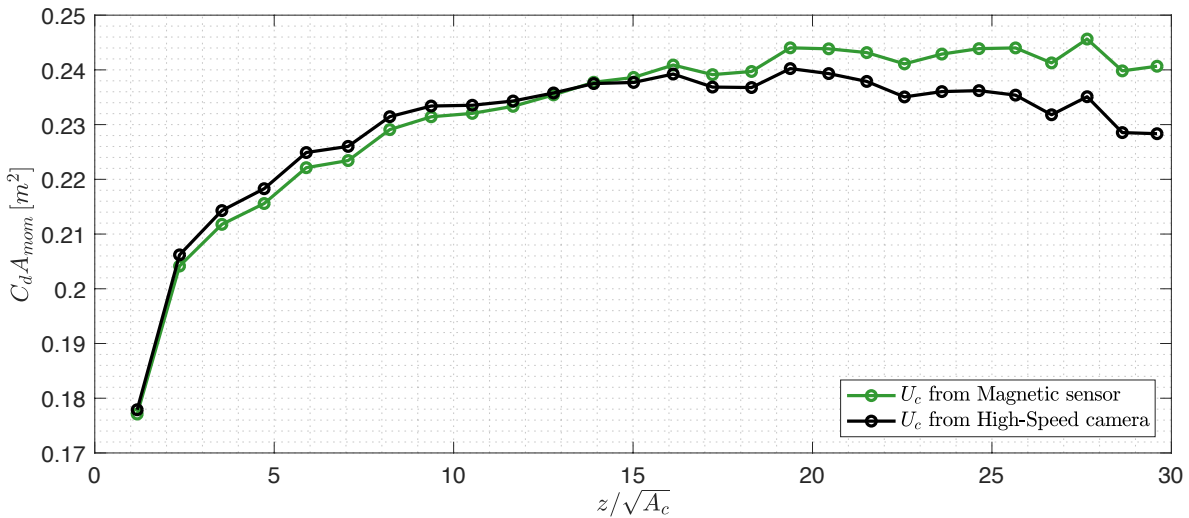


Figure 4.16:  $\overline{C_d A}$  momentum term variation with the method adopted to measure the cyclist's speed - time-trial dynamic configuration

**Pressure term** As well as the momentum term in the drag area, the mean pressure term is evaluated by reconstructing the pressure difference in the wake of the cyclist with respect to the ambient pressure. This reconstruction is based upon the PIV velocity measurements and follows the solution of the Poisson equation for the in-plane velocity components (Van Oudheusden, 2013) with neglected viscous terms (Van Oudheusden et al., 2007). Van Oudheusden (2013) highlights that high temporal resolution is required for appropriate evaluation of the instantaneous pressure fields and a statistical treatment of the flow would allow a simplification in Pressure Poisson Equation such as:

$$\frac{\partial^2 \overline{p}}{\partial x^2} + \frac{\partial^2 \overline{p}}{\partial y^2} = -\rho \left[ \left( \frac{\partial \overline{v_x}}{\partial x} \right)^2 + 2 \frac{\partial \overline{v_x}}{\partial x} \frac{\partial \overline{v_x}}{\partial y} + \left( \frac{\partial \overline{v_y}}{\partial y} \right)^2 \right] - \rho \left[ \frac{\partial^2 \overline{v_x'^2}}{\partial x^2} + 2 \frac{\partial^2 \overline{v_x' v_y'}}{\partial x \partial y} + \frac{\partial^2 \overline{v_y'^2}}{\partial y^2} \right] \quad (4.4)$$

with  $v_x$  the velocity component along the  $x$  axis and  $v_y$  along  $y$ . The fluctuating terms cannot be neglected as they are the main contributors in the wake of a bluff body (Van Oudheusden et al., 2007). When applying eq.4.4, the contribution of the out-of-plane velocity gradient is considered negligible

in affecting the pressure field determination. With Stereoscopic PIV data out-of-plane gradients are unavailable. The Poisson's equation is particularly indicated as an approach to diffuse the local error that can arise because of the two-dimensional flow assumption (Van Oudheusden, 2013).

Eq.4.4 is an elliptic partial differential equation and can be numerically solved by adopting a second-order five points scheme. The equation requires four boundary conditions to be well-posed, one for each of the four domain sides. As assuming a certain pressure on the FOV boundary through Dirichlet boundary conditions strongly affects the final pressure fields, null Neumann boundary conditions have been used. Nevertheless, in this way the equation is solved up to a constant. Hence, the freestream pressure at the top and side boundaries is used to rescale the overall pressure field. This procedure resembles the one applied in (Terra *et al.*, 2017).

**Vortex characterisation** The planar velocity vector and the cyclist's speed are sufficient to evaluate the drag momentum deficit and pressure term. However, in order to perform an aerodynamic analysis of the cyclist's wake, recognising the coherent structures governing the flow is of primary importance, as highlighted in section 1.2.2. The term *coherent structures* refers to "spatial coherent, temporally evolving vortical motions" (Jeong and Hussain, 1995, p.69) that present vortex cores with net circulation and are Galileian invariant. More recently, Haller (2005) has stressed the necessity of *objectivity* as a basic requirement for the identification of a coherent structure.

Because of the planar information that can be retrieved with Stereo-PIV, the vorticity out-of-plane component is the only one that can be computed. As a consequence, it is crucial to underline that only the planar projection of the vortices is gathered with the available data, and the vortices peak vorticity may be underestimated. This holds only to a certain extent, as the convection velocity is mainly in the streamwise direction.

Moreover, availability of 2D data restricts the possibility to distinguish unambiguously coherent structures from shear layers, as methods of vortex identification are based on the three-dimensional velocity gradient tensor. These methods are necessary as in turbulent flows both large-scale coherent structures and shear layers can exhibit high level of vorticity. Therefore, isolines of out-of-plane vorticity may be not sufficient to identify these structures. In this project the swirling strength criterion (Zhou *et al.*, 1999) is adopted to identify coherent structures. The criterion is based on a threshold imposed on the imaginary part of the complex eigenvalue pair of the velocity gradient tensor. Its 2D simplification reads as:

$$\lambda_{ci} = -\frac{\partial v_x}{\partial y} \frac{\partial v_y}{\partial x} + \frac{\partial v_x}{\partial x} \frac{\partial v_y}{\partial y} - 0.25 \left( \frac{\partial v_x}{\partial x} + \frac{\partial v_y}{\partial y} \right)^2 > 0 \quad (4.5)$$

Regions with positive  $\lambda_{ci}$  are coherent structures. In analysing the results it was noticed that a threshold equal to 1% of the maximum detected  $\lambda_{ci}$  has always coincided with the vorticity non-null contours. This means that the vorticity in the cyclist's wake has to be ascribed solely to the presence of coherent structures. For ease of reading, in chapter 5 a threshold  $\lambda_{ci} = 0.1$  is used, which is between 5% and 10% of the maximum detected value.





# 5

## Results and Discussion

In this section the results of the current thesis project are presented. They constitute the basis to answer the project research questions and draw major conclusions.

In the first part (section 5.2), flow field variables are presented for the following four configurations: time-trial static asymmetric, time-trial static symmetric, time-trial dynamic, upright dynamic. Flow-field analysis is drawn in terms of mean streamwise velocity deficit, in-plane velocity components, vorticity as well as velocity fluctuations. Flow field downstream evolution is accompanied with a more detailed analysis of the near wake structures characterising the cyclist’s wake. Qualitative and quantitative comparison among the configurations is presented as well as with the relevant literature, with a particular focus on [Crouch et al. \(2016a\)](#), who investigated three of the four studied configurations, and with the dynamic one at the same reduced frequency.

In the second part (section 5.3) of this chapter the measured drag areas and drag coefficients are compared. As well as the influence of the choice of the downstream plane on the drag estimation, an overall drag area and coefficient value relative to each configuration is provided together with some basic uncertainty results. Finally, a closer look is provided to the comparison with [Spoelstra \(2017\)](#) (section 5.4), i.e. the High-Speed outdoor Ring of Fire.

### Contents

---

<b>5.1 Cyclist’s speed</b>	<b>62</b>
<b>5.2 Flow fields.</b>	<b>62</b>
5.2.1 Time-trial static configurations	62
5.2.2 Time-Trial Comparison between Static and Dynamic.	70
5.2.3 Dynamic Comparison between Time-Trial and Upright	73
<b>5.3 Drag analysis</b>	<b>75</b>
5.3.1 Mean Drag area: Static cases	76
5.3.2 Mean Drag area: Dynamic cases	77
5.3.3 Drag Summary and uncertainty analysis	78
<b>5.4 Low-Speed ROF and High-Speed ROF</b>	<b>81</b>

---

## 5.1. Cyclist's speed

The cyclist's speed  $U_c$  contributes to both the momentum term and pressure term of the drag area. In addition, its time variation is used to determine an approximate relation between the acquired wake and the cyclist speed he had when the wake was released. With the approach based on the magnetic sensor, the difference in the acquired velocity never exceeds 3% of the reference velocity measured with the high-speed camera procedure, at the same cyclist streamwise position.

An idea of the mean cyclist's speed and the relative fluctuation across the runs is provided in Tab.5.1, when the cyclist seat is at the laser sheet location. The results are based on the data obtained from the magnetic sensor. Given the speed fluctuations, it is important to underline the necessity of taking the instantaneous speed into account in estimating the instantaneous drag area. Notice that the static cases have in general lower velocities, given the fact that the cyclist coasts down before.

Table 5.1: Cyclist speed statistics for the first downstream plane

	Mean Speed	% std
Static Asymmetric	4.47 m/s	2.8
Static Symmetric	4.25 m/s	3.1
Dynamic Time-Trial	5.3 m/s	2.1
Dynamic Upright	5.11 m/s	3.9

## 5.2. Flow fields

In this section, the flow field evolution of the cyclist's wakes is shown. Initially, a more detailed description is provided for the asymmetric static time-trial configuration. Secondly, the flow fields for the static cases are compared among themselves. Finally, main differences are highlighted among static and dynamic conditions, as well as between time-trial and upright postures. The flow analysis is always accompanied by a comparison to the most relevant findings in literature.

In showing the flow fields streamwise evolution, the reference coordinate system  $\mathcal{R} = \{x, y, z\}$  as in Fig.2.4 is adopted; thus, the origin corresponds to the rearmost point of the bike and the  $z$  direction is in the same direction as the free stream flow, opposite to the cyclist proceeding direction. Following the notation in eq.2.6, the mean dimensionless velocity deficit  $\overline{V_z}$  is expressed in a wind tunnel reference frame as:

$$\overline{V_z}(x, y) = \frac{u_o(x, y) - u_i(x, y) + U_c}{U_c} \quad (5.1)$$

The additional flow field variables are obvious.

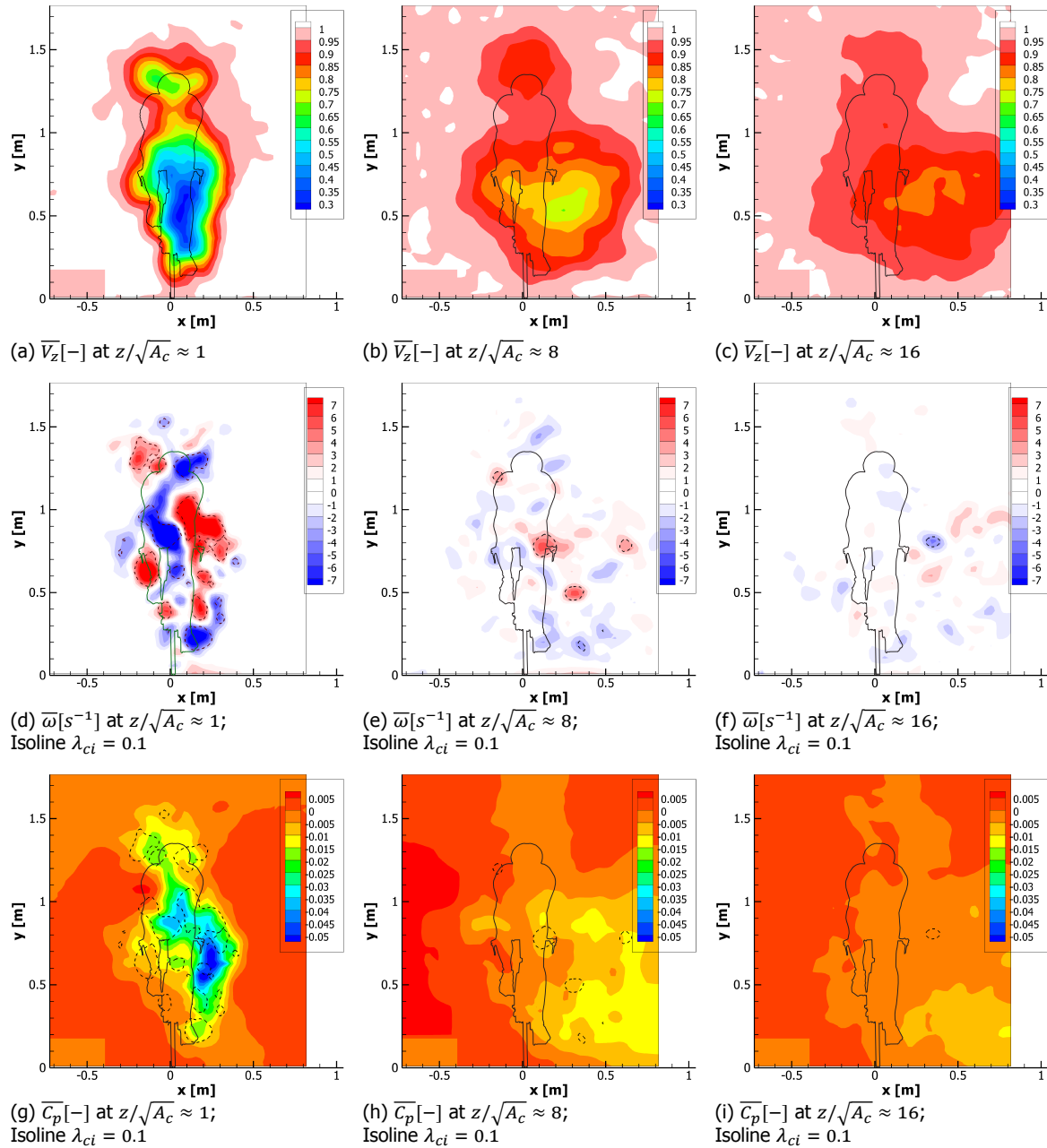
### 5.2.1. Time-trial static configurations

As discussed in section 3.6, the cyclist rides up to 12m downstream of the laser plane before coasting down. During coasting, the cyclist maintains a time-trial posture with right leg crank angle  $\varphi = 75^\circ$ , namely the asymmetric configuration or with right leg crank angle  $\varphi = 15^\circ$ , the symmetric configuration. In the former the right leg is extended, in the latter the thighs are aligned.

**Wake streamwise evolution** In Fig.5.1, three wake planes downstream of the cyclist in asymmetric configuration are shown. In the near wake of the cyclist the separated flow exhibits a momentum deficit up to 70% of the freestream velocity. The wake out-of-plane velocity contour shows the extent of the separated flow from the two legs, the head and the back of the cyclist. The major loss of momentum is in correspondence of the stretched leg, while the minor loss within the wake contour is noticeable at the height of the seat. Several vortex structures are visible in the cyclist's wake, which are later discussed in more details. In order to understand the velocity contour distribution it is important to highlight the presence of the two main vortex structures governing the cyclist's wake, the hip vortices, in agreement with the findings presented in chapter 1. In fact, these two counter-rotating vortices at the saddle height contribute to delay torso and lower back separation, thus reducing the velocity loss in the streamwise direction. Because of this interference, a secondary local minimum in  $\overline{V_z}$  is located in correspondence of the head wake. Moreover, isoline of positive swirling strength criterion

(Zhou *et al.*, 1999) marks the same regions as the vortex structures: this means that the cyclist's wake is mostly characterised by streamwise coherent circulation and planar vorticity contours are sufficient to distinguish large scale structures from shear layers. The threshold  $\lambda_{ci} = 0.1$  corresponds to 5% of the maximum  $\lambda_{ci}$  in the near wake.

Figure 5.1: Wake mean flow in Time-Trial Static Asymmetric configuration



Along the streamwise direction the wake evolves under a turbulent diffusion process as visible in Fig.5.1b and Fig.5.1c: flow entrainment smoothes out the planar gradient of streamwise velocity, so that a larger area presents momentum deficit but the lowest velocity value increases. After a certain streamwise range, the wake is at equilibrium and the integrated momentum deficit is constant along the streamwise direction, as shown in section 5.3.

It is interesting to analyse in a more quantitative fashion the growth rate of the cyclist's wake momentum deficit area. In Fig.5.2, the wake area is defined with the velocity contour area at  $0.95\overline{V_z}$  and its

growth is depicted for both the asymmetric and symmetric configurations. Its ratio with the cyclist's area grows with the square root of the dimensionless streamwise location up to  $(z/\sqrt{A_c})^{0.5} = \sqrt{8}$ , shown in Fig.5.1b. From this point onwards, the growth of the area for the asymmetric leg posture is not linear anymore, as the  $0.95\bar{V}_z$  contour exceeds the measurement plane area. Despite the three-dimensional character of the flow, this linear trend is in agreement with the evolution of a turbulent plane wake, as reported by White (2011).

Understandably, one could question if the linear character is maintained with the variation of the arbitrary  $\bar{V}_z$  contour level. In a restricted range  $0.9 \leq \bar{V}_z \leq 0.97$  the linearity holds but the slope of the linear fit varies with the chosen contour level. Fig.5.3 shows that the slope of the linear fit, thus  $\frac{\partial A_w}{\partial z}$ , grows linearly with  $\bar{V}_z$ , with a similar slope for both the two configurations.

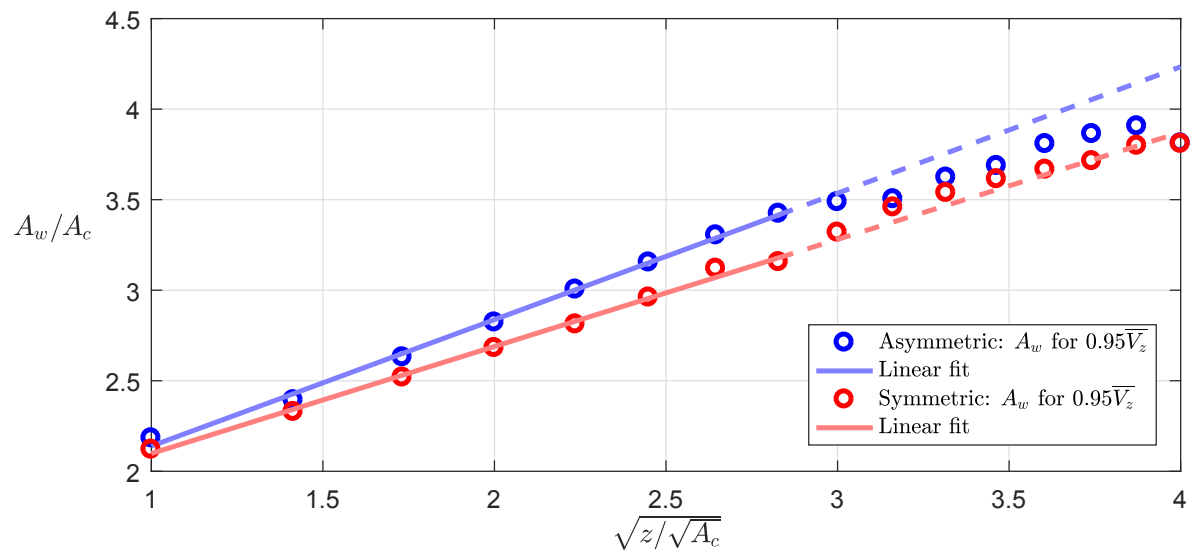


Figure 5.2: Wake growth for Time-Trial Static Configurations

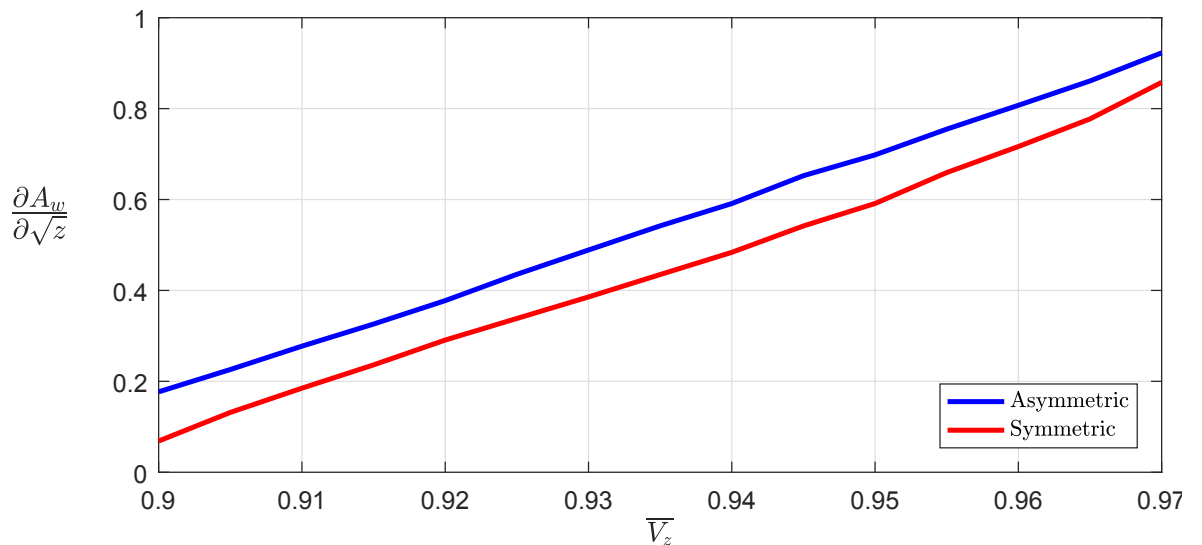


Figure 5.3: Wake growth rate as a function of the chosen  $\bar{V}_z$  contour level

Due to the turbulent diffusive processes in the wake, the in-plane gradient of the out-of-plane

velocity component decreases and the same holds for the in-plane velocity components: the large-scale vortex structures characterising the cyclist's wake decay in smaller scales (Fig.5.1d to Fig.5.1f) and Large-Scale PIV becomes unsuitable to detect them. Coherently, the reduced planar gradients bring the wake flow back to ambient pressure conditions (Fig.5.1g to Fig.5.1i). Notice that the imposed Neumann boundary conditions could negatively influence the evaluation of the pressure coefficient for the far wakes: in fact, as they go out of the measurement domain, the assumption of null normal pressure gradient at the walls can produce unreliable data. When considering both the pressure and the streamwise velocity deficit, it is noticeable that the variation with respect to the free stream conditions is more pronounced for the former rather than for the latter. As a consequence, it may be expected that the momentum contribution to the cyclist drag is more relevant than the pressure term, as shown in section 5.3.

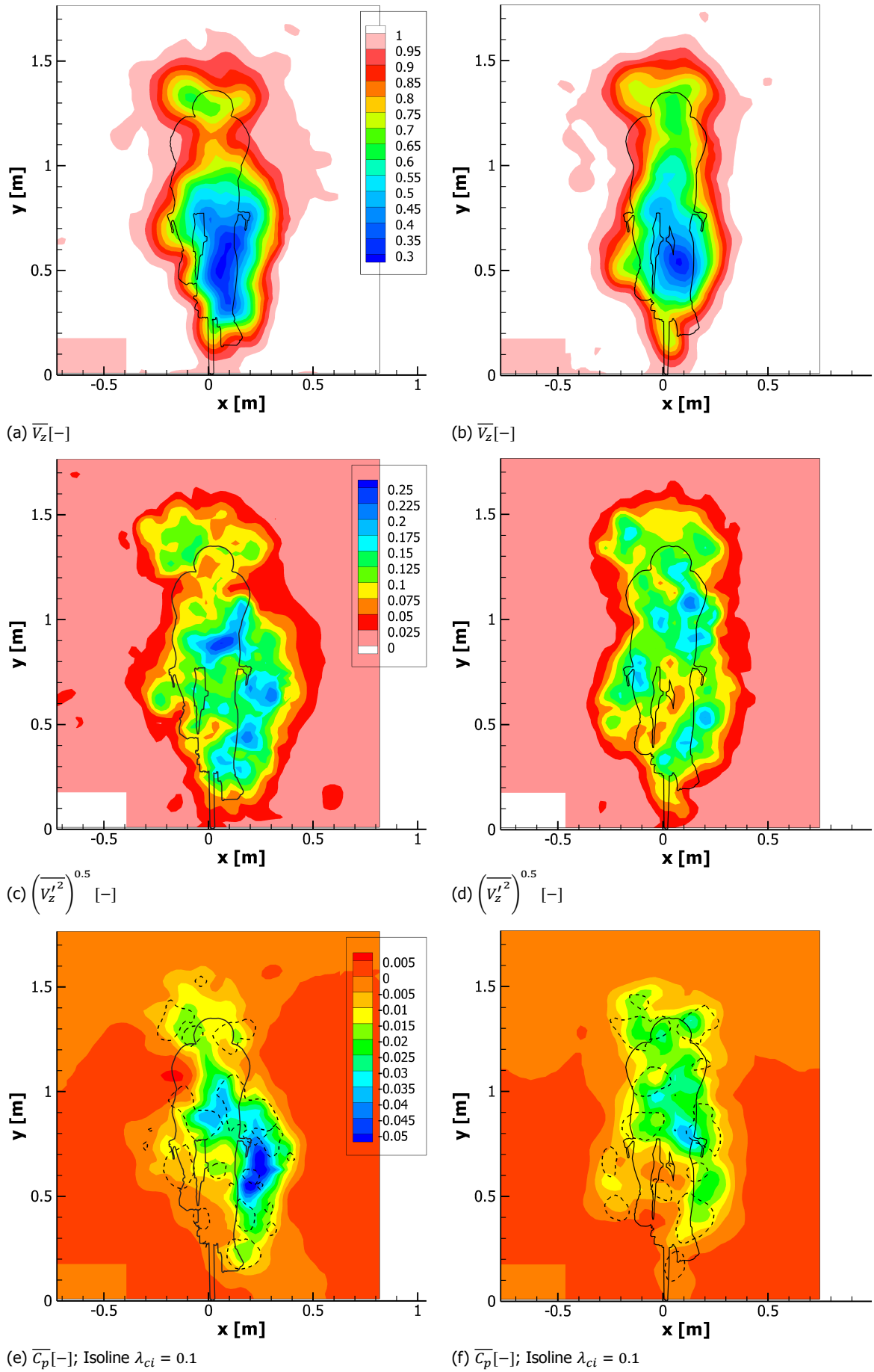
**Flow fields comparison between Asymmetric and Symmetric condition** In Fig.5.4 and Fig.5.5 the asymmetric and symmetric conditions are compared by considering the ensemble-average data for the near wake at  $z/\sqrt{A_c} \approx 1$ . In the first figure the streamwise velocity deficit and pressure fields are compared, while the in-plane velocity components are compared in the second one.

Considering the out-of-plane velocity contours, despite similar peak momentum deficit level, the symmetric case (Fig.5.4b) is affected by a smaller area of low  $\bar{V}_z$ . As in the asymmetric case (Fig.5.4a), the largest velocity deficit occurs in correspondence of the right leg, even in the case with the aligned thighs. In the symmetric configuration the right leg is slightly more stretched than the left one, as with  $\varphi = 15^\circ$  the right foot is at a lower height than the left one. Moreover, despite a smaller overall region of high streamwise velocity deficit, the two static cases have similar wake maximum width. In fact, the maximum width is similar in both size and  $y$  location, in correspondence of the left leg shin. Differently from the asymmetric case, the velocity deficit at the height between the cyclist back and the seat ( $1m \leq y \leq 1.2m$ ) is higher.

In Fig.5.4c and Fig.5.4d the root-mean-square fluctuations of  $V_z$  are shown for the asymmetric and symmetric conditions respectively. The maximum fluctuations are up to 25% of the freestream velocity while environmental turbulence is lower than 2.5%. The wake velocity fluctuations are similarly distributed between the two cases, with local maxima in correspondence of the vortex cores shown in Fig.5.5a and Fig.5.5b. As for the mean streamwise velocity deficit, the fluctuations are symmetric with respect to the cyclist for the symmetric case while more shifted towards the stretched leg in the asymmetric case. Notice that the flow fluctuations are affected by inaccuracy in the spanwise relocation of the instantaneous measurements, possibly leading to broader fluctuations distribution than in the reality.

Finally, mean pressure coefficient fields are shown in Fig.5.4e and Fig.5.4f. Pressure is lower than freestream within the wake while it is slightly higher in the vicinity of the wake outer contour. In both the cases the lowest pressure levels are in correspondence of the more stretched leg, due to the larger separation. However, the asymmetric configuration is characterised by lower local pressure than the symmetric one. Moreover, local pressure minima are located in correspondence of the vortical structures, highlighted by the dashed isocontour swirling strength criterion, even though this is not always the case. This is because in the vicinity of the back and the stretched leg the flow separation is the main aerodynamic feature characterising the low pressure levels. Instead, when large scale are dominants as for the head and the feet, local maxima correspond to the vortex cores.

In Fig.5.5 the asymmetric and symmetric leg postures are compared in terms of in-plane normalised velocities and the associated streamwise circulation. As shown in chapter 1, the cyclist's wake is strongly characterised by pairs of counter-rotating structures which have a role in the local flow angle of attack and the extent of body separation. Shah (2017) proposed an interesting approach to evaluate the vortices sense of rotation and correlate them to the orientation of infinite cylinders with respect to the free-stream. When suitable, this method is used to discuss the flow features characterising the cyclist's wake.

Figure 5.4: Near wake at  $z/\sqrt{A_c} \approx 1$  in Time-Trial Static configurations: Asymmetric (left), Symmetric (right)

The vortex structures are distinguished in the three following categories:

- Lift-induced vortices or horseshoe vortices, as the ones originated in fulfilment of the Helmholtz' vorticity conservation theorems;
- 3D Separation induced vortices, i.e. streamwise circulation caused by lateral flow entrainment due to lower back pressure in highly separated flows, as for three-dimensional bodies with a slant angle (Morel and Sovran, 1978) or very low aspect ratio wings (Crouch *et al.*, 2014);
- Quasi-2D Separation induced vortices, as the ones originated by a Von Karman vortex street in a cylinder; when the cylinder has got a non-null sweep angle, the vortices projection along the streamwise direction is measured.

Table 5.2: Main and secondary structures in the two static configurations

	Nature	Asymmetric	Symmetric
Head vortices	Lift induced	Stronger right	Stronger left
Hip Vortices	3D Separation induced	Main structures, asymmetric, the strongest couple	Similar strength as thigh vortices for lower hip
Inner Thigh vortices	2D Separation induced	Merged with the hip vortices	Main structures, symmetric
Ankle-Calf and Feet vortices	Lift induced	Stronger ankle-calf, especially for raised leg	Similar strength of the four vortices
Knee vortices	2D Separation induced	Similar	
Shin vortices	3D Separation induced	Similar	

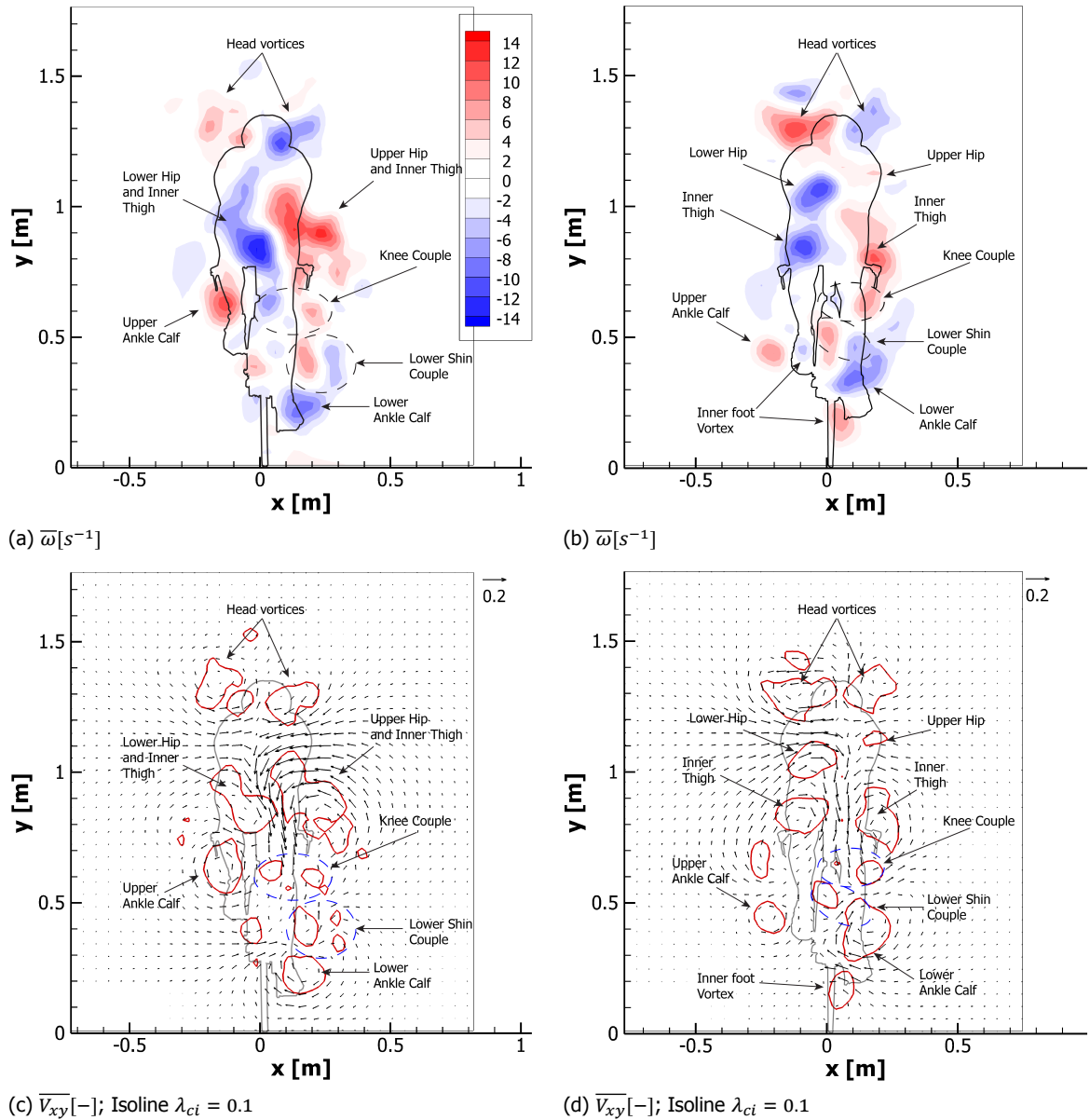
The nature of the vortices is summarised in Tab.5.2. In Fig.5.5a and Fig.5.5b the wake structures are compared. Positive vorticity relates to counter-clockwise rotating vortices, while negative vorticity to clockwise ones. The differences in the local angle of attack of the body and the surface pressure induced by the leg positions affect the dynamics of the following structures:

- Head/Helmet vortices: these vortices are due to the elongated time-trial helmet (Fig.3.7). Given their sense of rotation, it may be speculated that they are originated by a lift-induced mechanism. This could be caused by a low pressure on the lower side of the helmet due to the neck separation. On the upper side, the helmet resembles an airfoil shape and the flow recovers near the tail to a pressure higher than the one at the neck separation. With similar relative strength, the vortex pair induces upwash in both the configurations (Fig.5.5c and Fig.5.5d), but the symmetric one presents higher vorticity.
- Hip vortices: these are the most important vortices in the cyclist's wake. They are due to the lower back separation entraining side flow and form along the slanted back (Fig.1.5). They are the primary cause for the strong downwash after the cyclist's back (Fig.5.5c and Fig.5.5d). Moreover, their asymmetric and symmetric position is at the origin of the configuration name. In the former, their higher vorticity reduces back separation compared to the latter, as discussed in the wake velocity contour analysis. In the symmetric case they have similar strength as the inner thigh vortices, while it is likely that in the asymmetric case they merge with the thigh ones as two single vortices. Moreover, as well as in-plane downwash, their asymmetric position induces a net sidewash towards the right, at the origin of the wake lateral displacement. In general, the hip vortices are the structures the longer lasting downstream before vortex bursting phenomena occur: this is due to their unique generation mechanism, with the vorticity vector mostly parallel to the free-stream.
- Inner thigh vortices: these vortices are co-rotating with the hip vortices and are due to the separation of the thighs. Their role varies with the slant angle of the cyclist torso, as discussed in

the following literature comparison. In the symmetric case, the left thigh has got similar strength as the right thigh and lower hip vortices. This vorticity equilibrium keeps the wake narrower than in the asymmetric case. This finding is similar to the conclusions of [Crouch et al. \(2014\)](#), although in the current study the right hip has lower contribution than the quadrupole in the reference.

- Ankle-Calf vortices: high pressure in the vicinity of the ankle compared to the foot sole causes a pair of counter-rotating vortices per foot. While the lower ankle-calf has got similar strength and relative position in the two cases, the upper one is stronger in the asymmetric case, given its vicinity to the front torso higher pressure field.

Figure 5.5: Near wake at  $z/\sqrt{A_c} \approx 1$  in Time-Trial Static configurations: Asymmetric (left), Symmetric (right)

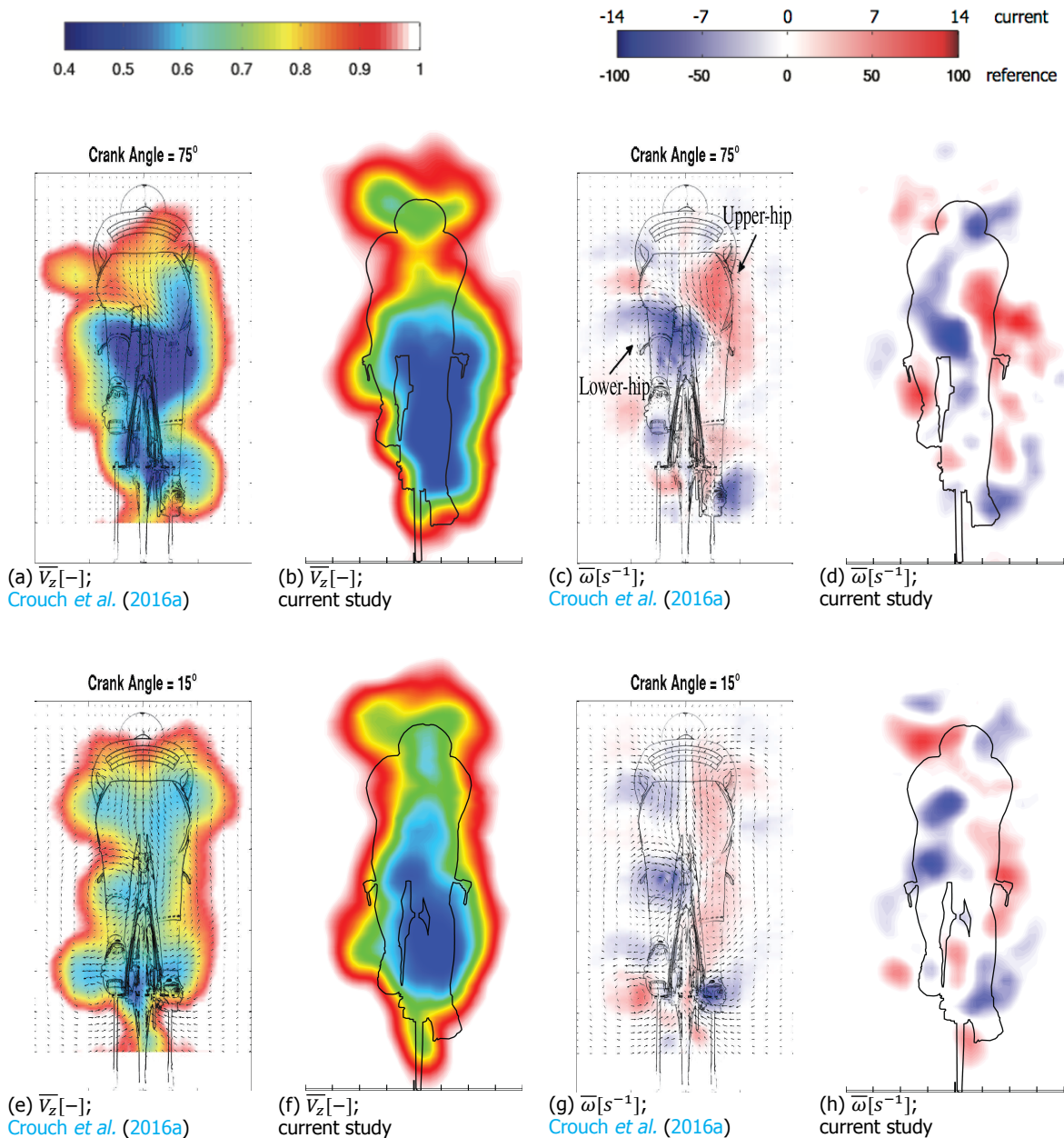


Apart from these main flow features highlighted in [Crouch et al. \(2014\)](#); [Terra et al. \(2016\)](#), hypotheses can be made on the presence of secondary flow structures, discussed in [Shah \(2017\)](#) as well:

- Inner Foot vortices: these two vortices are the twins of the ankle-calf ones. While barely visible in the asymmetric case, they have more relevant vorticity levels in the symmetric one.

- Knee vortices: they are generated by the alignment of the upper part of the shin with the free-stream and are typical of the more stretched leg.
- Lower Shin vortices: in this case the mechanism is mostly due to separation in the knee pit together with the orientation of the shin towards the free stream. The counter-rotating couple induces local upwash and works against the knee couple.

Figure 5.6: Near wake at  $z/\sqrt{A_c} \approx 1$  in Time-Trial Static configurations: Asymmetric (top), Symmetric (bottom)



A similar static test has been performed by Crouch *et al.* (2014) on the upper part of the wake and repeated by Crouch *et al.* (2016a) for the full wake. In both cases pressure probes are used to scan the cyclist's wake. The results are reproduced in Fig.5.6 and compared to the current experiment. As the experiments were performed on a fixed ground test section, the ground boundary layers is present in the reference results and has been masked by the author.

Firstly, it is important to underline the difference in vorticity magnitude for the two cases, which can be mostly linked to the torso based Reynolds number to be four times larger than in the current case,  $1.8 \cdot 10^5$  against  $6.9 \cdot 10^5$ . In fact, a comparison of dimensionless vorticity ( $\omega T/U_c$ ), with  $T$  the torso length, would result in a more similar quantitative comparison. Despite the Reynolds number difference, the momentum deficit shape and spatial distribution is similar between the two asymmetric cases, with the peak momentum deficit in correspondence of the right leg knee pit. Despite a similar cyclist height, the two wakes differ on the upper part: vorticity plots show that the head vortices are negligible in the case of the reference and so the in-plane motion is mostly dictated by the downwash induced by the two hip vortices. However, the reference presents a larger wake width at the height of the upper back, possibly due to the head vortices interacting with the hip vortices, differently from the current experiment. Apart from the head structures, hip, ankle-calf, thigh, knee and shin vortices are present in similar position and with similar relative strength. Unfortunately, the peak momentum deficits are not comparable as in the current experiment this is equal to  $0.3V_z$ , while in the reference experiment the results are provided with a saturated streamwise velocity scale at  $0.4V_z$ .

In the symmetric case the differences with the reference are less negligible. Still the velocity contours of the two wakes are symmetric and both present the largest asymmetry due in correspondence of the left foot. However, the peak momentum deficit is considerably higher in the current experiment. Again, a larger wake width is noticed in correspondence of the upper back, retaining a similar symmetry as the upper part of the current experiment wake. This confirms the hypothesis of a different interaction of the head vortices with the hip ones, to a certain extent.

Vorticity fields in the symmetric case helps to explain one of the two possible reasons for a higher momentum deficit in the current experiment. The reference hips and thighs have similar magnitude and they annihilate each other (Crouch *et al.*, 2014). Instead, the lower upper hip vorticity in this case makes them lasting longer. The higher difficulty in repeatability of the symmetric leg posture is claimed as the source of this difference: in fact, it is intuitively easier to stretch a leg than keeping the thighs aligned and this difference has been noticed as well during the experiment. For instance, consider the flow field obtained in time-trial static posture at  $\varphi = 0^\circ$  by Crouch *et al.* (2014) in Fig.5.7. Given this result, it may be supposed that the vortices for this leg posture have been averaged in the symmetric leg posture ( $\varphi = 15^\circ$ ), during the multiple tests.

The second reason is due to the difference in the Reynolds numbers. The estimated torso Reynolds number ( $1.8 \cdot 10^5$ ) in the current experiment is in the range before  $Re_{cr}$  for a cylinder, while the reference experiment is in the drag crisis regime. Therefore, it is understandable to record a larger velocity deficit in the current experiment.

Finally, it is worthy to mention the results of Shah (2017) and Jux (2017). In their wind tunnel experiment with the cyclist in asymmetric condition, the authors claimed that the main source of asymmetry in the wake is due to the inner thighs vortices rather than to the hip vortices, as they were barely noted in both the experiments. Their result differs from the current findings and the findings of Crouch *et al.* (2014, 2016a,b). In the current author's opinion, the differences are ascribed to the tested object: while the cyclist in this experiment and the Crouch *et al.* (2014)'s model had a torso inclination, Jux (2017); Shah (2017)'s model had a torso aligned with the ground as in the proper time-trial position. As the hip vortices generation mechanism is linked to the torso inclination (or body slant angle in analogy with the Ahmed body (Morel and Sovran, 1978)), it is understandable that they could have been negligible in the case of Shah (2017).

### 5.2.2. Time-Trial Comparison between Static and Dynamic

In this section the static measurements are compared with the dynamic ones.

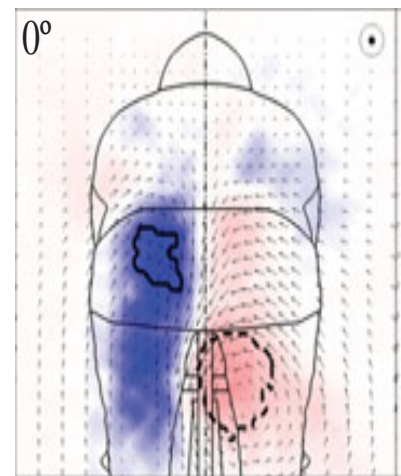
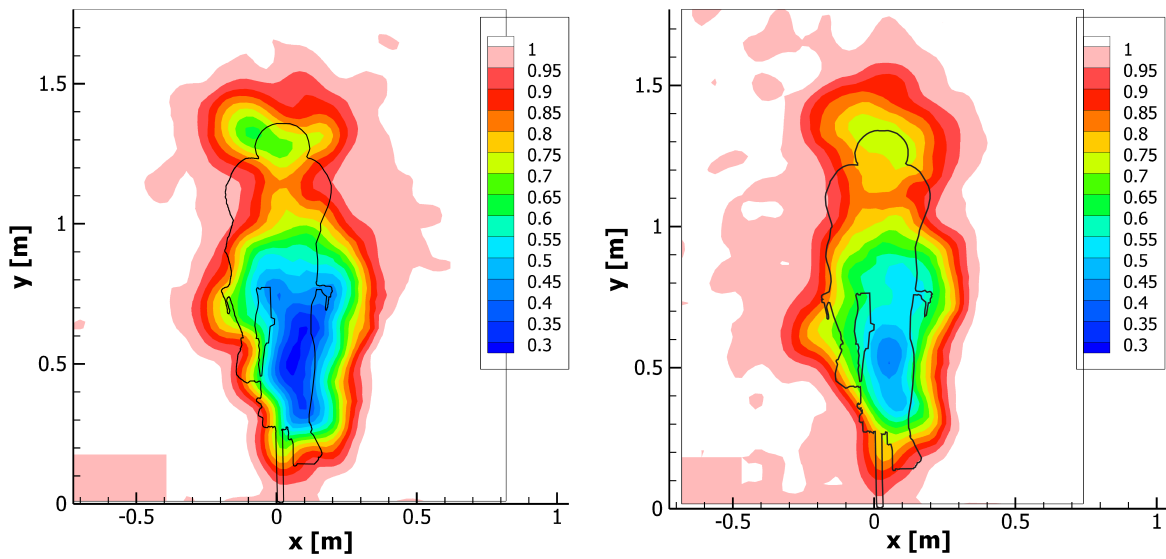


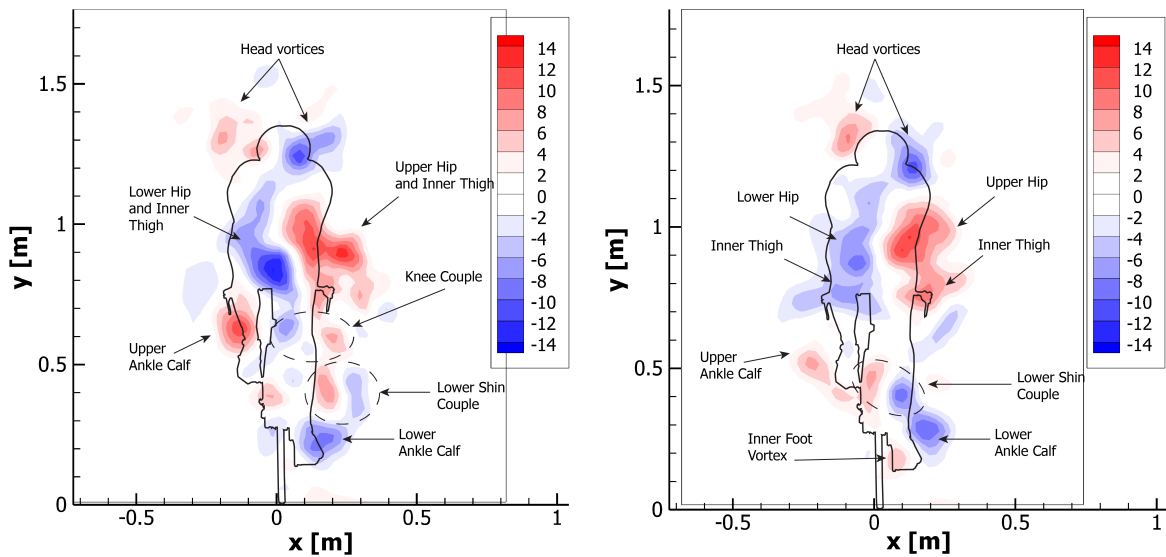
Figure 5.7:  $\bar{\omega}[s^{-1}]$ ; Time-Trial Static at  $\varphi = 0^\circ$ ; colour scale as in Fig.5.6; reproduced from Crouch *et al.* (2014)

Figure 5.8: Near wake at  $z/\sqrt{A_c} \approx 1$  in Time-Trial Asymmetric configurations: Static (left), Dynamic (right)



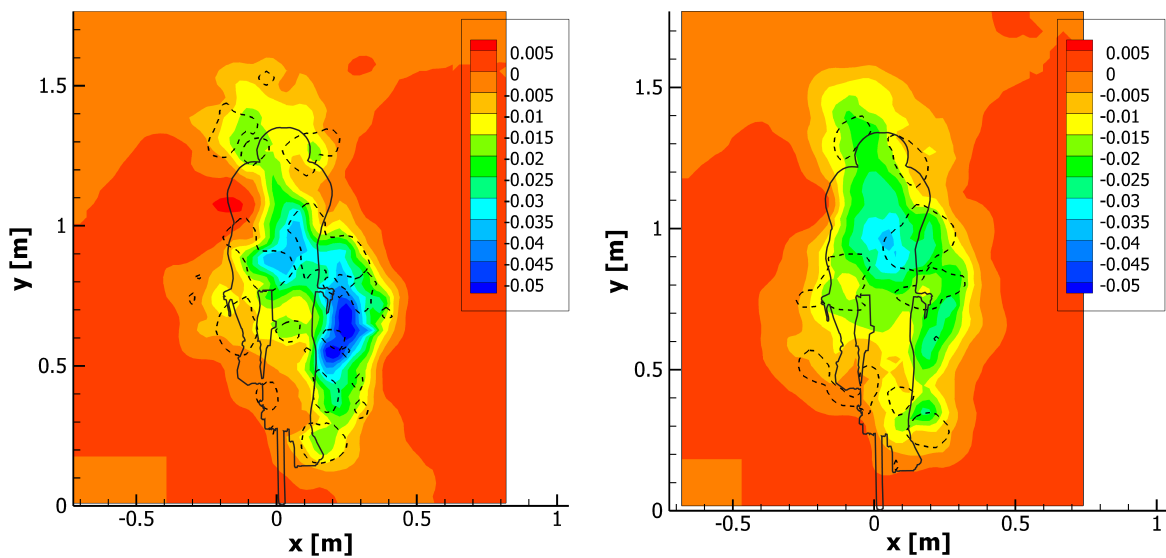
(a)  $\overline{V_z}[-]$

(b)  $\overline{V_z}[-]$



(c)  $\overline{\omega}[s^{-1}]$

(d)  $\overline{\omega}[s^{-1}]$



(e)  $\overline{C_p}[-]$ ; Isoline  $\lambda_{ci} = 0.1$

(f)  $\overline{C_p}[-]$ ; Isoline  $\lambda_{ci} = 0.1$

Some preliminary differences need to be highlighted. As discussed in chapter 3, the dynamic experiments are set so that the first acquired wake corresponds to the wake shed when the cyclist is in asymmetric condition with  $\varphi = 75^\circ$ . This was done to compare the current experiment to [Crouch et al. \(2016a\)](#). Moreover, given the assumed mean wake convection factor and the reduced frequency  $k = 0.119$ , the wake acquired at  $z/\sqrt{A_c} \approx 5$  carries the history of the symmetric configuration for  $\varphi = 15^\circ$ . Finally, a small torso-based Reynolds number difference is present in the current experiment, given the necessity to coast down in the static cases:  $Re_T = 2.3 \cdot 10^5$  for the dynamic ones and  $Re_T = 1.8 \cdot 10^5$  for the static ones.

The near wake for the asymmetric configuration is compared in Fig. 5.8. From a qualitative point of view the two velocity deficit contours are similar in shape, proving a successful design of the experiment for the dynamic scenario. However, in general the dynamic condition shows a lower momentum deficit in both the two minima, in correspondence of the stretched leg and the head. In fact, Fig. 5.8f shows that lower momentum deficit is accompanied by higher pressure as well. Because of this difference, the dynamic wake has the lowest pressure in correspondence of the cyclist back, rather than in correspondence of the stretched leg as in the static case. Both Fig. 5.8b and Fig. 5.8f show that the region between the head and the seat has got higher momentum deficit and lower pressure than in the static case: to a certain extent this aspect is more similar to the symmetric case, possibly due to the mixing effect of the wake unsteadiness.

In terms of wake structures, most of them are common in terms of position and strength and it can be said that the dynamic effect on the wake induces little variation from a qualitative point of view. The hip vortices are more distinguishable from the thigh vortices in the dynamic case (Fig. 5.8d), while their asymmetry is still clearly visible. However, their strength is lower than the static case (Fig. 5.8c), possibly due to a combination of the flow unsteadiness as well as the missing merging phenomenon with the thigh vortices. In terms of secondary structures, the knee couple is missing when the legs rotate while the upper ankle calf strength is decreased.

Furthermore, it is worthy to consider the wake velocity contours for the symmetric configuration in Fig. 5.9, for  $z/\sqrt{A_c} \approx 5$ . As for the asymmetric configuration the steady tested object induces higher peak momentum deficit than in the dynamic scenario. However, Fig. 5.9b presents a more symmetric velocity contour as it could be expected as well as similar maximum wake width. This shows a substantial agreement with the convection factor assumption and proves to a certain extent the success of the phase-locked average procedure.

Figure 5.9: Wake at  $z/\sqrt{A_c} \approx 5$  in Time-Trial Symmetric configurations

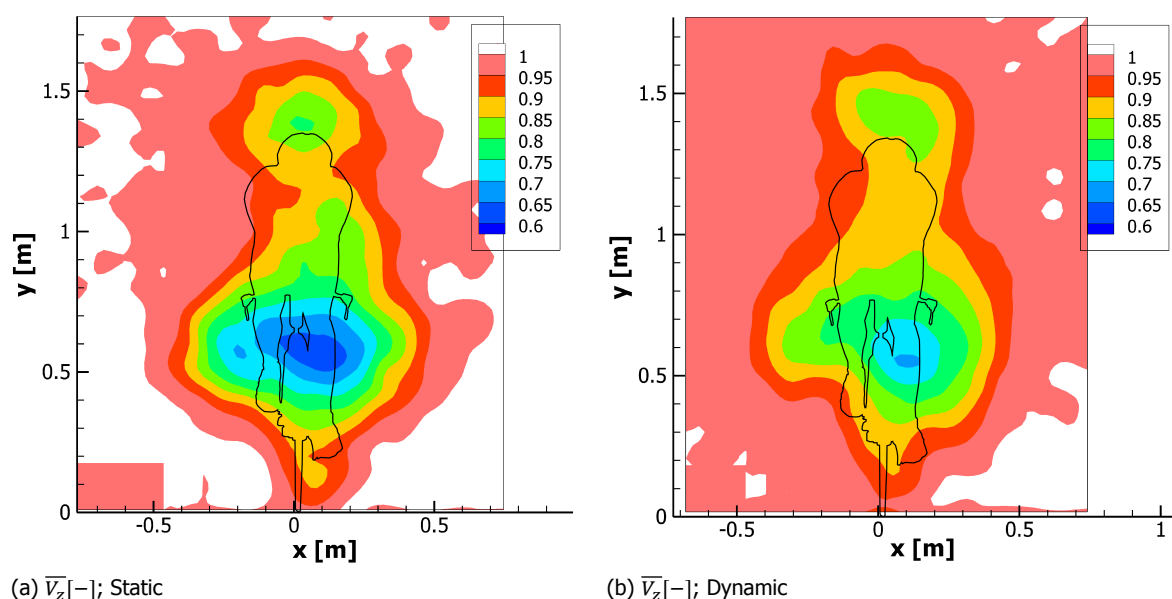
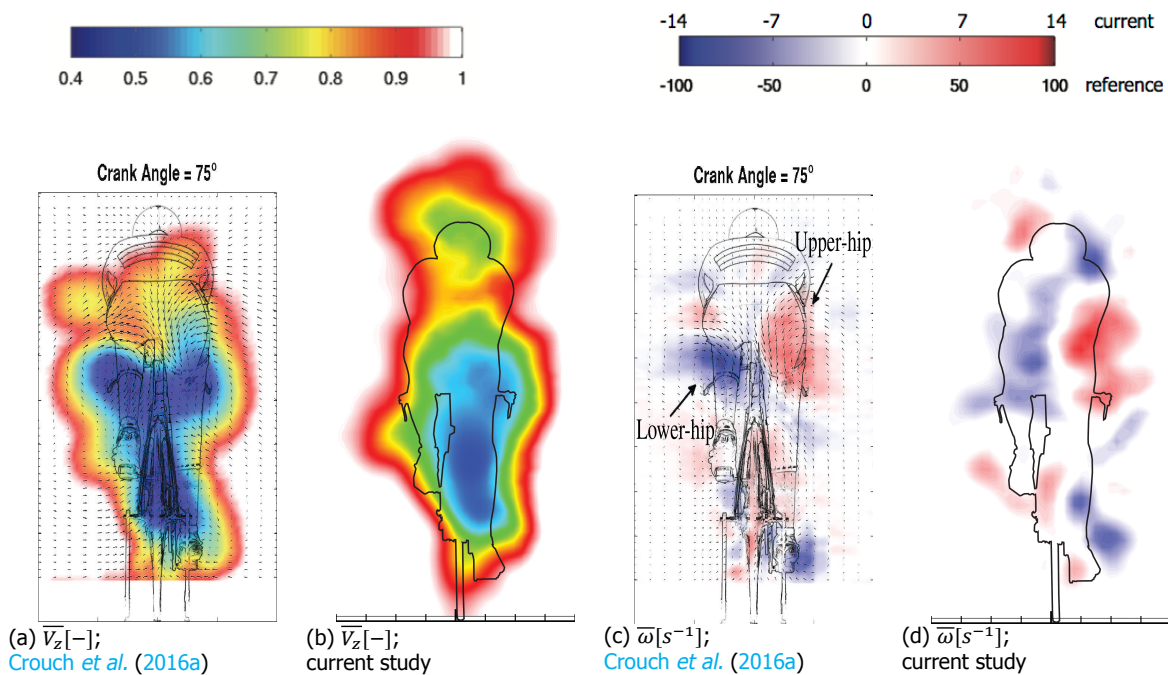


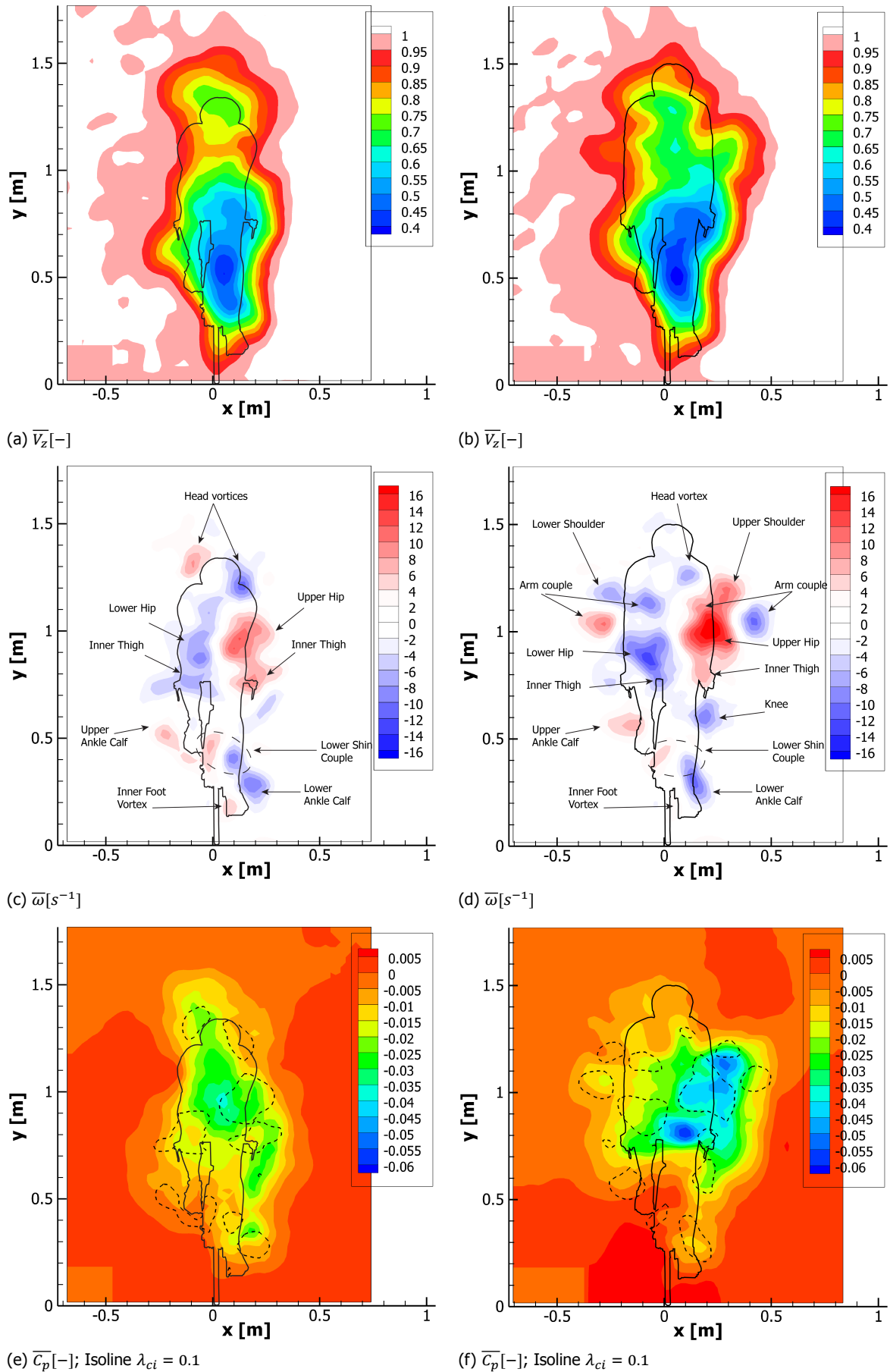
Figure 5.10: Near wake at  $z/\sqrt{A_c} \approx 1$  in Time-Trial Dynamic configuration

In Fig. 5.10 the flow fields comparison with the reference literature [Crouch et al. \(2016a\)](#) is shown for the near wake in dynamic conditions. In both the cases, the experiment was designed to take into account the wake convection so that the wake at  $z \approx 1\sqrt{A_c}$  represents the scenario with  $\varphi = 75^\circ$ . Moreover, the two experiments were conducted at the same reduced frequency, as main similarity parameter of the encountered real conditions for a time-trial cyclist, while the torso based Reynolds number is three times larger in the reference case,  $2.3 \cdot 10^5$  against  $6.9 \cdot 10^5$ . Apart from the differences in the head wake affecting the static cases as well, there is no major difference to be underlined from a qualitative aspect. In fact, the wake contour separation in correspondence of the legs, the hip and thigh vortices, the ankle-calf vortices, the knee vortex, are similar in location and relative strength. Notice that, from a quantitative aspect, the wake momentum deficit in correspondence of the hip vortices is higher in the reference case.

### 5.2.3. Dynamic Comparison between Time-Trial and Upright

Finally, the two dynamic cases are hereby discussed, thus in time-trial and upright (brake-hoods) posture. In both, the cyclist started from the same position and at the same crank angle so that the phase-locked average was comparable. Moreover, their torso-based Reynolds number is the same. In the current section, the flow phenomena for the first wake are compared, i.e. the one at  $\varphi = 75^\circ$ , in Fig. 5.11.

From the comparison between the time-trial posture (Fig. 5.11a) and the upright one (Fig. 5.11b), it can be stated that the streamwise velocity contours are comparable in the wake for  $y < 0.9m$ , apart from a higher momentum deficit at the height of the right knee pit ( $y = 0.65m$ ) and of the seat ( $y = 0.8m$ ). On the upper part, larger wake width and higher momentum deficit can be noticed for  $y > 0.9m$ : in fact, the upright position has got a larger torso inclination angle and so the body is further away from a streamlined shape. Interestingly, the  $0.95\overline{V_z}$  contour is as high as for the time-trial position, despite a higher cyclist's height (1.5m instead of 1.35m). The larger momentum deficit, and so larger momentum term in the drag evaluation (section 5.3), is accompanied by lower pressure coefficient as well. In fact, Fig. 5.11f shows considerably higher peaks of low pressure than Fig. 5.11e, almost double, in particular in the entire upper part of the wake, including both the torso and arm separations.

Figure 5.11: Near wake at  $z/\sqrt{A_c} \approx 1$  in Dynamic Asymmetric configurations: Time-Trial (left), Upright (right)

Finally, the flow structures characterising the two wakes are compared in Fig.5.11c and Fig.5.11d. There is substantial equivalence in the vortex structure strength and position, with the exception of the hip-thighs and the head vortices. In the former, while retaining the characteristic asymmetry, the upright position shows higher vorticity on both sides. In the latter, the upright helmet vortices are negligible structures. This is the primary reason for the similarity in the wake velocity contours despite the difference in height: in the time-trial position the head vortices are not negligible structures as their core is accelerated along the aligned torso, while the upper back separation is the dominant flow feature in the upright case. To a certain extent, one might suppose that a vortex-stretching mechanism is increasing the head vortices in the time-trial position because of the surface pressure distribution on the torso. Furthermore, the head is further away from the measurement plane in the time-trial position than in the upright one: the head couple induced upwash increases the wake size so that at a similar characteristic length from the cyclist wheel the out-of-plane velocity contours of the two dynamic cases have similar height.

Moreover, the new posture shows new large scale structures. Their origin is hereafter hypothesised:

- The Shoulder vortex: for each shoulder one outer vortex is shed. Its generation mechanism is proper of what has been called as a 3D separation. In fact, on both sides they are co-rotating with the hip vortices. This structure arises as a consequence of the low pressure in the upper back of the cyclist, as shown in Fig.5.11f. It could be supposed that it is related to the more exterior part of the shoulder, closer to the arm.
- The Arm couple: this vortex couple consists of an outer counter-rotating vortex with respect to the shoulder one and an inner co-rotating one. In this case the generation mechanism is different. In fact, as the arms are extended forward towards the brake hoods, their cylinder model upper surface is swept away from the incoming flow. Their rotation sense is coherent with this analysis and therefore they are the resulting planar projection of the laminar 2D separation of the arms. These two vortices have similar strength as the arm pressure fields are slightly influenced by the legs asymmetry. Moreover, the inner right arm vortex merges with the upper hip vortex.

The most relevant comparison for the upright position flow field is the High-Speed ROF of Spoelstra (2017), with the vorticity field shown in Fig.5.12. Notice that the overlaid cyclist silhouette is not representative of the real case scenario, as it was obtained from the wind tunnel time-trial model used by Shah (2017) and Terra *et al.* (2016) and unnaturally enlarged.

The vorticity field shows the same main and secondary vortices, despite the indications in the figure, both in location and strength as in Fig.5.11d. However, the head vortices are clearly present in the case of Spoelstra (2017). Therefore, they might have an influence on the wake vertical development together with the shoulder vortices, given the upwash effect they induced as seen in Fig.5.5c. The more relevant vorticity of the head vortices may be due to a different torso inclination with respect to the free stream. Notice the large resemblance in the hip vortices strength and position asymmetry as well as the clear appearance of the outer arm vortices.

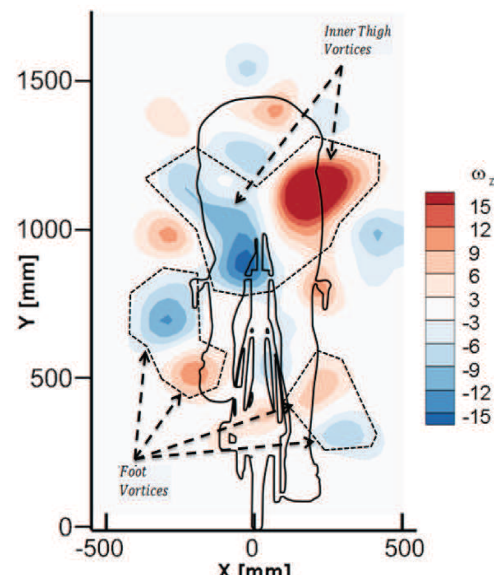


Figure 5.12: Vorticity field in Upright configuration, reproduced and rescaled from Spoelstra (2017); cyclist silhouette unreal

### 5.3. Drag analysis

In this section the results of the drag area evaluation based on the control volume approach are presented in terms of mean values. In addition, based on the computed cyclist's frontal areas, his drag

coefficient is estimated. The attention is focussed on the Low-Speed Ring of Fire performances for instantaneous drag measurements in the comparative section 5.4 with the High-Speed Ring of Fire.

### 5.3.1. Mean Drag area: Static cases

The two static configurations are compared in Fig.5.13, where the mean  $C_d A$  streamwise variation is plotted. The uncertainty bars refer to the uncertainty on the mean computed with a coverage factor of 2. Therefore, there is 95% confidence that the mean drag area lies within the plotted uncertainty bar. While 18 test runs are available for the asymmetric configuration, 17 are for the symmetric one. In both the cases the drag area increases along the streamwise direction up to a point where it reaches a plateau for  $z > 6\sqrt{A_c}$ . The mean drag area for the asymmetric condition is always higher than the one for the symmetric one. Moreover, in the far wake the drag area has larger fluctuations for the asymmetric case than for the symmetric one: this is due to the intrinsic nature of the two wakes. In fact, the hip vortices asymmetry induces a lateral outwash that brings part of the wake out of the FOV, while the symmetric configuration has been found to retain its symmetry up to the farthest plane, and so to reduce the out of plane motion.

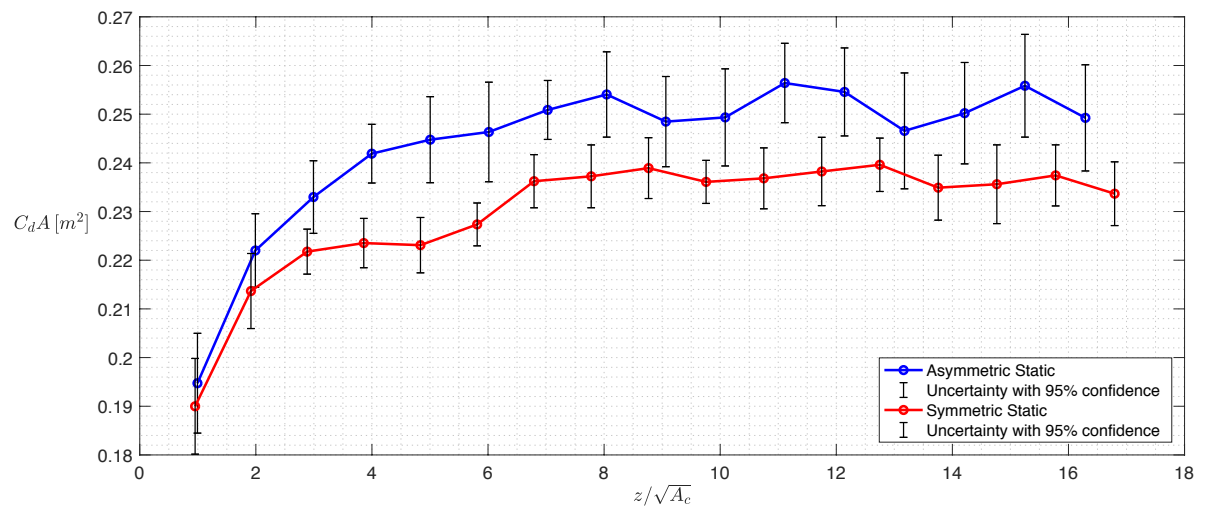


Figure 5.13: Streamwise variation of the drag area for Static configurations

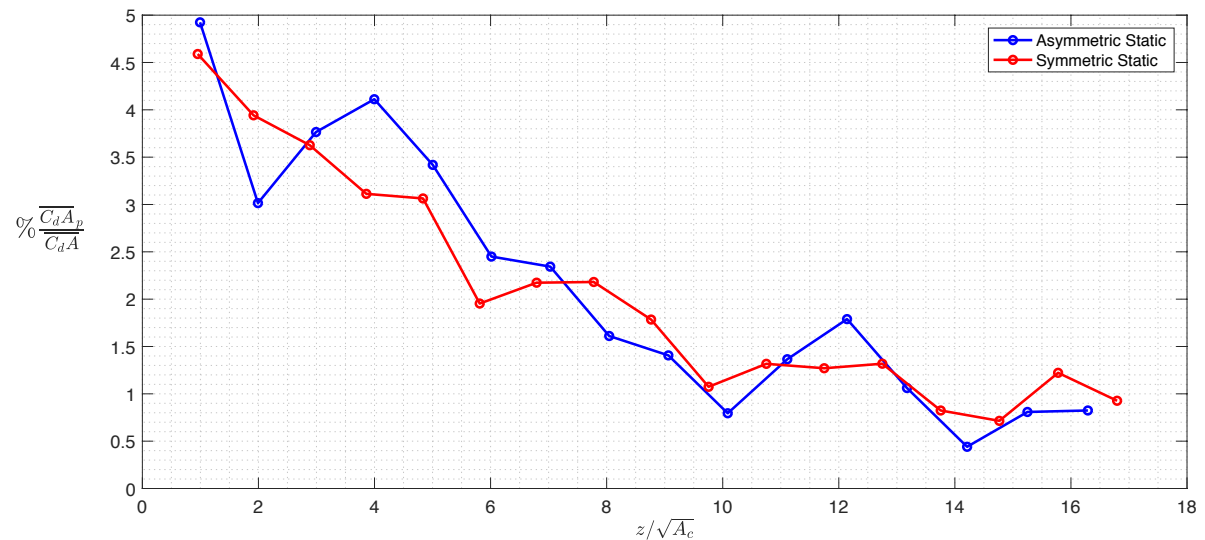


Figure 5.14: Streamwise variation of the mean pressure term of the drag area for Static configurations

The streamwise trend in the mean drag area is coherent with the findings of Terra *et al.* (2017)

for the momentum term of the mean sphere drag, where the pressure term was negligible after five sphere diameters. Nevertheless, the results in Fig.5.13 include the pressure term. Its percentage contribution over the overall drag area is shown in Fig.5.14. As expected, the pressure term has its largest contribution on the first planes and decays to about 1% downstream. This result is in agreement with the wind tunnel Tomo-PIV experiment of Terra *et al.* (2016), while differs from the findings of Shah (2017), who concluded that the pressure term is always negligible after  $1\sqrt{A_c}$ . Therefore, one might question the current results since the drag area is not constant over the streamwise plane, as it would be expected by the application of the control volume approach. Among the factors that might contribute to that, apart from the limitations of the control volume derivation for the Ring of Fire as described in chapter 2, one might be ascribed to the pressure term evaluation. In fact, the procedure to evaluate the pressure fields could lack in accuracy as the streamwise velocity gradients are considered negligible with the approach presented in section 4.9. Another factor may be ascribed to the Reynolds number difference, as this experiment was conducted at a cyclist speed closer to Terra *et al.* (2016) than Shah (2017).

### 5.3.2. Mean Drag area: Dynamic cases

The two dynamic cases are compared in Fig.5.15. In this case the number of runs is 28 for both the upright and time-trial cases. Notice that a larger amount of planes is acquired downstream of the cyclist, as there is no concern in distinguishing the dynamic from the static wakes, as for the previous configurations. Similarly to the static cases, the same streamwise trend for the drag area is observed and a plateau in the drag area is reached for  $z > 6\sqrt{A_c}$ . Moreover, it is interesting to notice that the effect of the crank angle variation is somewhat hidden in the mixing process caused by the unsteadiness introduced by the cyclist. Similarly, Spoelstra (2017) did not identify a clear crank angle trend as in the fixed plane measurements of Crouch *et al.* (2014). Again, the mixing process observed in the flow field analysis can be considered as the primary cause of indistinguishable crank angle trend on the phase-locked average data. Therefore, it is more correct to say that the wake diffusion process is the dominant effect in the streamwise evolution of the wake. As a consequence, it is correct to define the wake time scale based on the characteristic length of the bluff body rather than based on a proportional time to the inverse of its cadence. In addition, this result is coherent with the observations of Crouch *et al.* (2016a), who highlighted a small influence in the drag evaluation for the current reduced frequency.

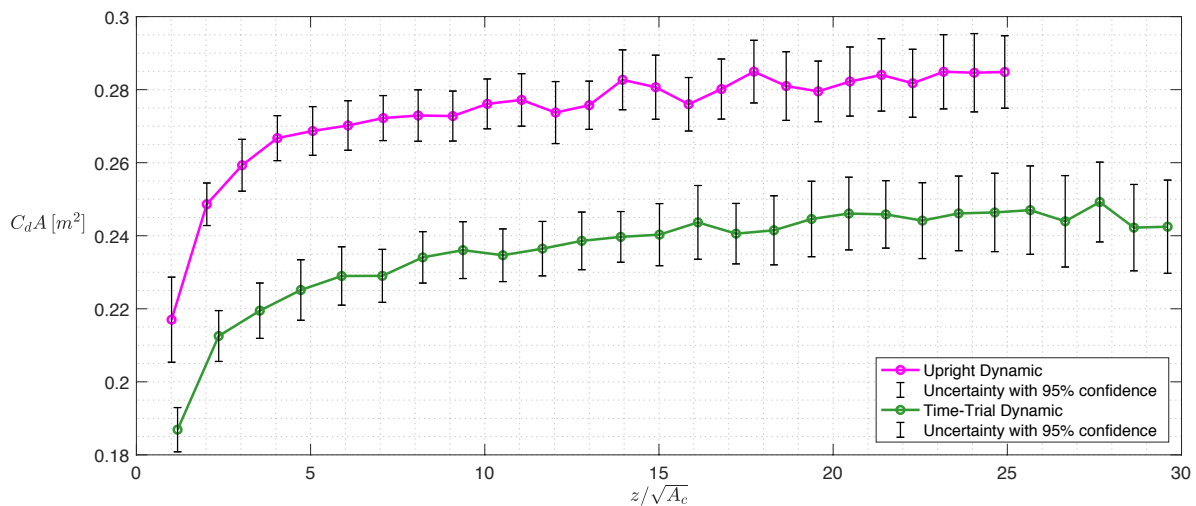


Figure 5.15: Streamwise variation of the drag area for Dynamic configurations

The observations on the flow fields in the comparison of the two dynamic cases (Fig.5.11) showed that the upright posture has got a clearly higher momentum deficit, as well as larger contribution of the pressure term to the drag area. As a consequence, the upright drag area is constantly higher than in time-trial position and there is no intersection between the uncertainty bars as it occurred in the static cases comparison. Moreover, the momentum deficit is the determinant factor in the drag difference as the pressure term percentage contribution is always lower than in the time-trial posture

for the far wakes (Fig.5.16). Finally, as a general remark among the four configurations, the pressure term percentage contribution is about 5% for the near wake and decays with similar trend at about 1% in the far wake.

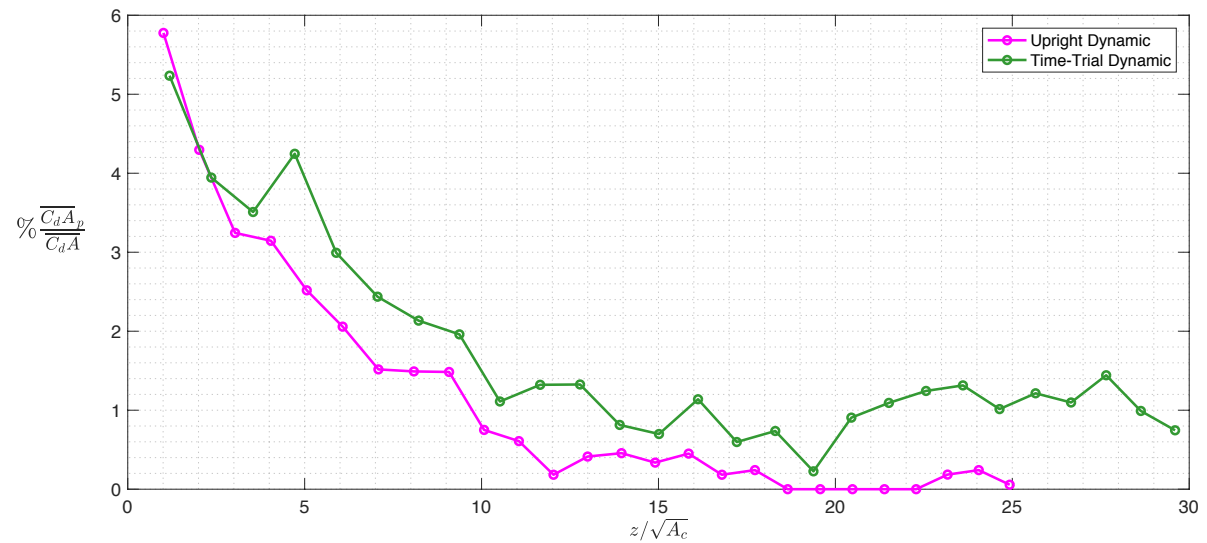


Figure 5.16: Streamwise variation of the mean pressure term of the drag area for Dynamic configurations

### 5.3.3. Drag Summary and uncertainty analysis

With the aim of defining an overall drag area for each of the configuration, the ensemble average is taken across the uncorrelated different test runs and across the correlated streamwise planes. However, only the measurements for  $z > 6\sqrt{A_c}$  are regarded, following the previous observations in the streamwise drag area trend. The results for the four configurations are shown in Fig.5.17 while an overview of the measurement standard deviation and mean drag area, frontal area and drag coefficient is shown in Tab.5.3. In order to evaluate the mean uncertainty, similarly to the mean, the standard deviation of the drag area measurement is computed across all the runs and the selected range of samples. Then the uncertainty is evaluated with a coverage factor 2 with respect to the number of uncorrelated samples. While the runs are uncorrelated, the planes have a certain amount of correlation. The number of effective planes can be estimated using the Nyquist criterion (Sciacchitano and Wieneke, 2016), with the integral time scale estimated based on the characteristic length  $\sqrt{A_c}$  of the diffusion wake phenomenon. It must be remarked that this approach is rather conservative, especially for the dynamic cases. In fact, differently from a typical wind tunnel scenario, the acquired images are at different streamwise positions as well as different time instants, so different seeding levels, laser illumination, environmental fluctuations and cyclist position itself decrease the extent of the correlations among the streamwise samples. Of course this holds true especially for the dynamic cases.

The asymmetric leg position and the symmetric one have a mean drag area of  $0.252m^2$  and  $0.237m^2$  respectively, so there is a 6% difference in drag area. With the different leg positions, the cyclist's area differ of 1.5%, therefore the drag coefficient is the primal responsible for the drag area differences. As it was discussed in the flow field analysis in Fig.5.5, this does not come as a surprise, because the different crank angle is responsible of two different flow regimes. In addition, this result is coherent with the balance measurements of Crouch *et al.* (2014) discussed in chapter 1, despite a 15% maximum variation in drag area while a 2% difference between the two crank angle postures. The main reason for this difference has already been highlighted in the literature comparison with the flow fields. Crouch *et al.* (2014) underline a cross-annihilation diffusive phenomenon due to an equally balanced vortex quadrupole in the symmetric case. Instead, the position repeatability difficulty proper of the Ring of Fire has not allowed to replicate  $\varphi = 15^\circ$ , which is the only case for which this phenomenon occurs. Therefore, the smaller strength of the upper hip vortex (Fig.5.5b) is hereby clarified. Differently from the static symmetric posture, the cyclist has less trouble in maintaining a stretched leg position and the drag area results for the asymmetric case is more comparable to the relevant literature (compare Tab.1.1).

It is crucial to notice that the 6% difference between the two positions is highlighted with less than 20 cyclist passages and their uncertainty bars do not intersect. There is 95% confidence that the two configurations are actually different from each other, thus the Low-Speed Ring of Fire is suitable for detecting small drag area differences.

Table 5.3: Configurations drag summary

	Static Asymmetric	Static Symmetric	Dynamic Time-Trial	Dynamic Upright
$A_c$ [m <sup>2</sup> ]	0.316	0.311	0.314	0.4
Mean $C_dA$ [m <sup>2</sup> ]	0.252	0.237	0.242	0.28
$C_d$	0.796	0.761	0.771	0.699
Std $C_dA$ [m <sup>2</sup> ]	0.020	0.013	0.026	0.022
Std $C_dA$ [%]	8.0	5.4	10.6	8.0
Uncertainty $C_dA$ [%]	1.7	1.2	1.2	1.0
N runs	18	17	28	28
N effective planes	5	5	12	9

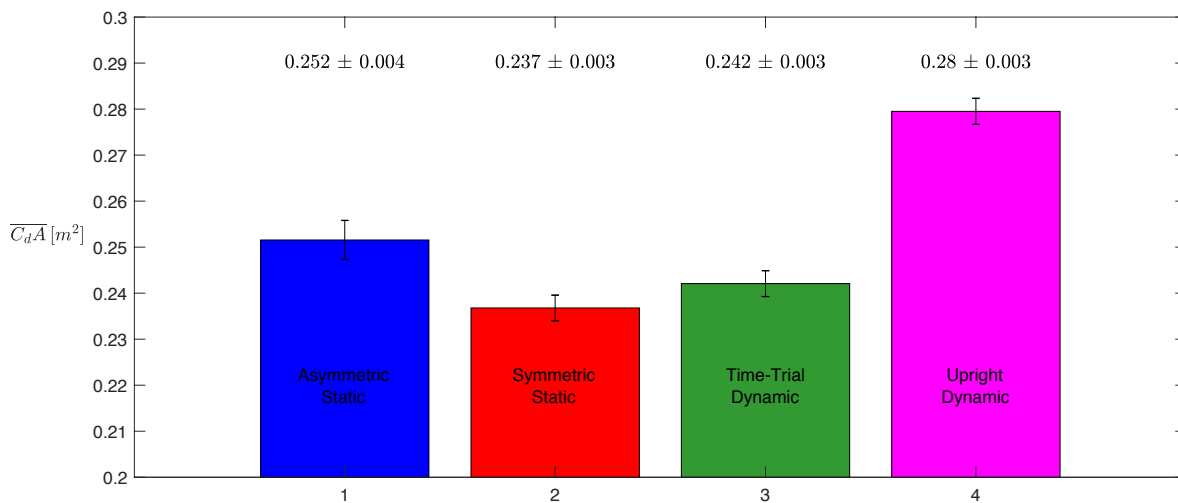
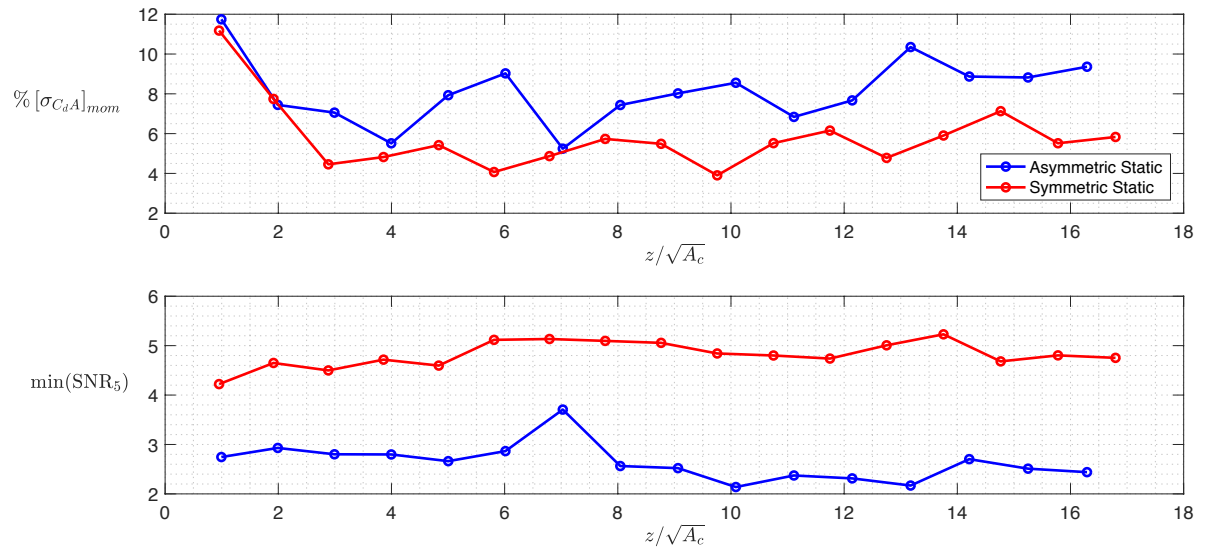


Figure 5.17: Overall drag area comparison

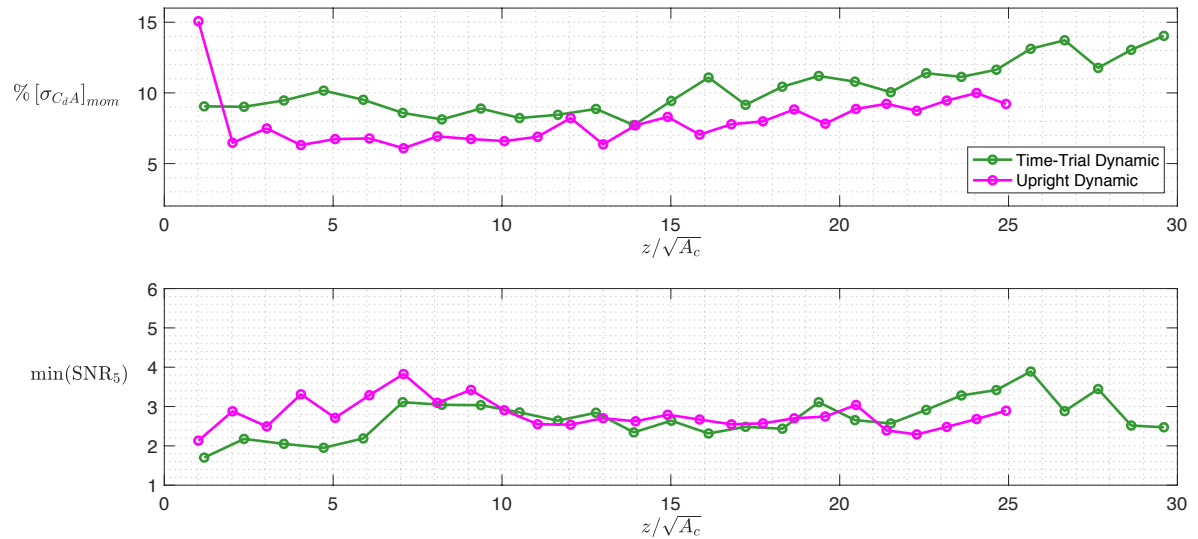
By taking into account the time-trial dynamic drag, it is noticeable how it lies between the two static cases (Fig.5.17), which are the two drag area extrema during the crank angle (Crouch *et al.*, 2014). During a crank cycle, the drag areas tend more towards the asymmetric one as shown in chapter 1, so it might be expected that the mean over different crank angles would be more biased towards the asymmetric static one. In this experiment, this is not the case, and this is due to the discussed overestimation of the symmetric drag area, because of the repeatability issues in maintaining the thighs aligned for the cyclist. Moreover, it is interesting to underline the differences in standard deviation between the three time-trial cases as shown in Tab.5.3. The dynamic case has got higher standard deviation than both the static cases: therefore, despite there is not a clear phase-locked average trend

in the streamwise drag area, the standard deviation is still affected by the cyclic leg position variation of the cyclist.

Figure 5.18: Standard deviation in the momentum term of the drag area across the runs for each downstream plane and relation to the minimum five percentile SNR in the PIV measurement



(a) Static cases



(b) Dynamic cases

This phenomenon is absent in the two static cases instead, and the drag area standard deviation is of the order of 8.0% and 5.4% for the asymmetric and symmetric posture respectively. This difference is related to two different contributions: the wake turbulent fluctuation and the measurement error. On one hand, the discussion pertaining the flow fields in Fig. 5.5a and Fig. 5.5b highlighted the presence of higher vorticity structures in the asymmetric condition. This can be linked to a higher amplitude of the unsteady phenomenon characterising a bluff body wake and therefore higher amplitude of the drag variations among the runs. On the other hand, the asymmetric measurements suffer a lower signal to noise ratio in the PIV visualisations. In fact, by considering the five percentile SNR on the wake plane as done in section 4.6, and taking its minimum across the runs for each downstream plane, it is noticeable in the lower part of Fig. 5.18a how the asymmetric posture has got half of the  $\min(\text{SNR}_5)$ . Moreover, Fig. 5.18a provides relevant information between the PIV measurement and the standard deviation of the drag area across the runs: in fact, a lower  $\min(\text{SNR}_5)$  is associated with a higher

$[\sigma_{C_d A}]_{mom}$  and viceversa. This occurs as well in relation to single downstream location, for instance consider the respective trends at  $z = 7\sqrt{A_c}$ .

In analysing the downstream trend of the momentum term standard deviation, the near wake and far wake trends are more affected by the following two additional considerations. In the near wake, the streamwise velocity gradient is higher than in the far wake and the limitations of the current phase-locked average, i.e. the photo detector delay synchronisation (appendix A) and the streamwise relocation procedure (section 4.1), are the primary sources in the drag area standard deviation. In fact, consider that in the nearest cyclist's wakes even negative momentum deficits are noticed as in cylinder flows. Instead, in the far wake, the standard deviation tends to increase towards the longest distances and this is attributed to the wake going out of the FOV, as shown in Fig.5.1c.

Finally, the comparison between the dynamic conditions is discussed. The mean upright drag area is 15% higher than the time-trial drag with a similar uncertainty on the mean. This difference is lower than the High-Speed Ring of Fire measurements of Spoelstra (2017), who found a difference of 25% and an upright drag area about  $0.3m^2$ , in a similar definition of the upright position. This difference can be related to the larger upper part of the wake due to the head vortices interaction, as underlined in the discussion of Fig.5.12. Defraeye et al. (2010b) obtained an upright drag area of  $0.27m^2$  in their wind tunnel balance measurements with 25% difference with respect to the time-trial position. However, their upright position was characterised by the hands in the handlebar centre rather than on the brake hoods. Instead, Grappe et al. (1997) report a drag difference slightly lower than 15%, obtained with a powermeter linear regression analysis.

Moreover, notice that the drag coefficient in the upright posture is lower than in the time-trial posture. This result draws a different conclusion with respect to the analysis of the static positions as the variation in the drag area for the upright posture is mostly due to the frontal area difference, rather than for aerodynamic characteristics. However, this result should not come as a surprise as flow field analysis strengthens this outcome, given similar aerodynamic phenomena between the time-trial and upright posture. Barry et al. (2015) report the same effect in comparing nine different postures: in their upright case, with the hands on the brake hoods as in this experiment, the drag area is equal to  $0.343m^2$  with  $C_d = 0.69$ , while in the time-trial position  $C_d A = 0.283m^2$  and  $C_d = 0.73$ .

With regards to the upright drag area standard deviation, the absolute value is similar to the one for the time trial dynamic case, as similar structures are present. Furthermore, one might argue that the larger number of structures and their associated higher vorticity should lead to a slightly higher fluctuation in the drag area, even with the considerations about the missing head vortices. Another hypothesis may account for a difference due to the PIV measurement error. Nevertheless, based on the considerations for the static cases, Fig.5.18b shows a similar signal to noise minimum five percentile after the near wake, while the reduced fluctuations for the upright case are clearly visible in each downstream plane. In conclusion, the most reasonable hypothesis is linked to the experiment condition: the reduced acceleration length and the low velocities are source of lateral instability for the cyclist, as he aims at keeping the time-trial position. Instead, the upright position is somewhat more natural for the cyclist and it may be speculated that he is more able to repeat it from run to run.

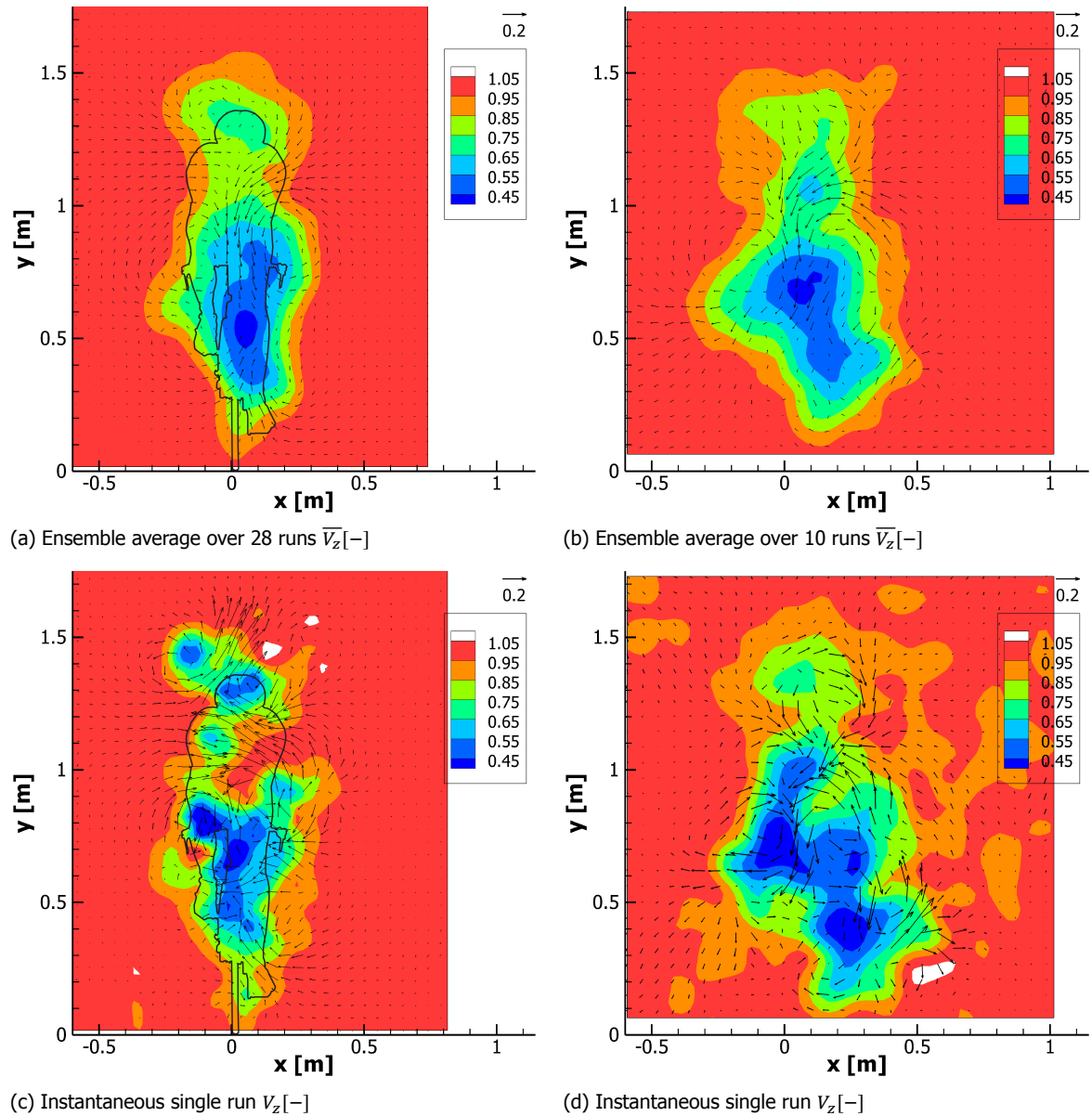
## 5.4. Low-Speed ROF and High-Speed ROF

In section 2.1, main differences between a high-speed and a low-speed PIV system have been highlighted. When comparing the current experiment to the one conducted by Spoelstra (2017), one has to notice that the two Rings of Fire were placed indoor and outdoor respectively. Moreover, similar sensor size was used for the cameras and it has already been pointed out that the advantage of higher laser power and smaller pixel size of the low-speed system is somewhat reduced because of the necessity of higher image plane - laser plane distances.

In Fig.5.19 the flow field velocity for the two Rings of Fire is compared. On the top row the ensemble average flow fields are shown, while an instantaneous case is visible on the bottom row. On the left, the results of the Low-Speed ROF, i.e. the current experiment, are shown, while on the right the results of Spoelstra (2017) are reproduced on similar contour levels. The vectors are shown with a

vector pitch twice as the measured one. The mean flow fields are similar in terms of wake shape and momentum deficit, with both the head wake and the two legs wake contours noticeable as well as the back downwash and main hip structures. However, in general the High-speed ROF exhibits a larger wake width. Two causes could be ascribed for this difference: an almost doubled reduced frequency in the High-speed ROF ( $k = 0.23$  against  $k = 0.12$ ), causing larger wake mixing because of higher wake unsteadiness as well as larger effects of the environmental fluctuations. The larger extent of the environmental fluctuations is visible in the comparison between the instantaneous flow fields (Fig. 5.19c and Fig. 5.19d).

Figure 5.19: Near wake at  $z/\sqrt{A_c} \approx 1$  in Time-Trial configuration: Low-Speed ROF (left), High-Speed ROF (right); right figures reproduced from Spoelstra (2017)



In both the cases the environmental fluctuations have been averaged over a set of upstream planes and subtracted from the specific downstream plane, based on how  $V_z$  has been defined in equation 5.1. Therefore, the larger in-plane and out-plane motions of the environmental fluctuation in the High-Speed ROF are ascribed to the variable outdoor conditions within the few seconds between the upstream plane acquisition and the downstream plane one. To give an idea, the indoor environment has got a tempo-

ral root-mean-squared of the streamwise velocity component  $\left(\overline{u_i'^2}\right)^{0.5}$  between  $0.03\text{m/s}$  and  $0.05\text{m/s}$ . This means that the turbulence intensity was around 1%. The outdoor environment has got a velocity fluctuation from two to three times the indoor environment one.

The instantaneous flow fields are comparable with the mean flow fields in terms of out-of-plane velocity distribution and wake width. The main differences occur in the in-plane motion, as the analysed flow structures have their own shedding frequency and they are intermittent on an instantaneous plane at a fixed downstream location.

As noticeable from the figures, the vector pitch is slightly higher for the High-speed ROF, with 24mm in the Low-Speed case and 29mm in the High-Speed case. As discussed in chapter 4, most of the runs in the current experiment could have been correctly solved with a 48px interrogation window, so leading to 18mm vector pitch. However, similar considerations could be drawn for the High-Speed ROF as well, since in both the cases the limiting factor is due to the seeding uniformity throughout the experimental campaign and across the FOV. In addition, the outdoor environment is the primary source for instantaneous and mean flow fields differences, as well as limiting factor in the uniformity of seeding density.

Another relevant way to compare the two systems can be by the typical PIV performance parameters: the Dynamic Velocity Range (DVR) and the Dynamic Spatial Range (DSR). The first is defined as the ratio of the highest measured velocity with respect to the smallest one (Adrian, 1997), while the second can be defined as the ratio of the FOV and the interrogation window size. As the smallest measured velocity gives information regarding the uncertainty on the measurement, the standard deviation of the velocity on an upstream plane is considered, as long as the environmental velocity is negligible. Instead, the maximum measured velocity is evaluated at the downstream plane closest to the cyclist. The latter is of the order of  $0.01\text{m/s}$  for the in-plane components and  $0.02\text{m/s}$  for the out-of-plane component. This leads to  $DVR \approx 250$  for the out-of-plane component and  $DVR \approx 160$  for the in-plane components. Regarding the DSR, with  $IW = 64\text{px}$  and  $FOV_y = 1628$ ,  $DSR = 25$ . Instead, for the High speed ROF,  $DVR \approx 100$  and  $DSR = 16$  (Spoelstra, 2017).

In Fig.5.20 five randomly sampled runs for the time-trial dynamic case are considered between the two experiments. The occurrence of outliers in some planes (Fig.5.20b) affects instantaneous drag measurements for near wakes in Spoelstra (2017). Moreover, the outdoor ambient could anticipate the movement of the far wake out of the field of view. In the current experiment this happens only for larger distances, and in particular for the static asymmetric condition, because of its described flow physics.

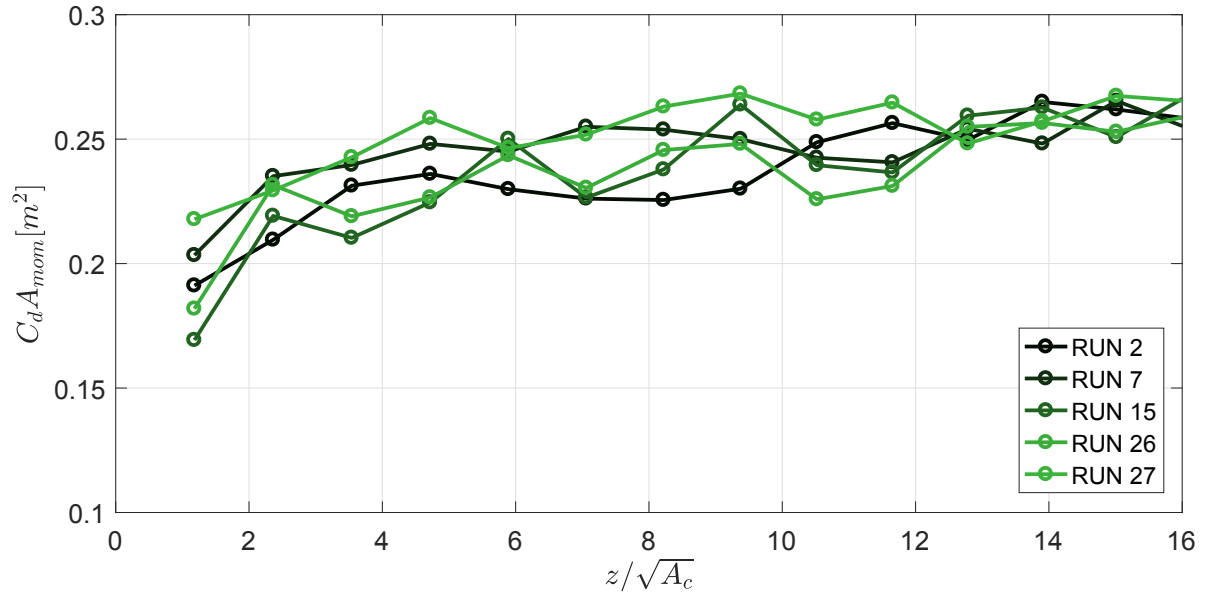
Even in the instantaneous runs, the streamwise trend in the momentum term of the drag area is noticeable, in particular for the current experiment and to a certain extent for the High Speed ROF.

To give a more quantitative idea regarding the fluctuation on the drag measurement, consider Fig.5.21. The streamwise variation of the standard deviation of the drag area across the test passages is plotted for the experiment of Spoelstra (2017). This figure is comparable with Fig.5.18b, for the same dynamic configurations. Notice that the streamwise wake evolution was evaluated up to  $z \approx 16\sqrt{A_c}$  in Spoelstra (2017)'s experiment, while there is information up to  $z \approx 26\sqrt{A_c}$  in this project.

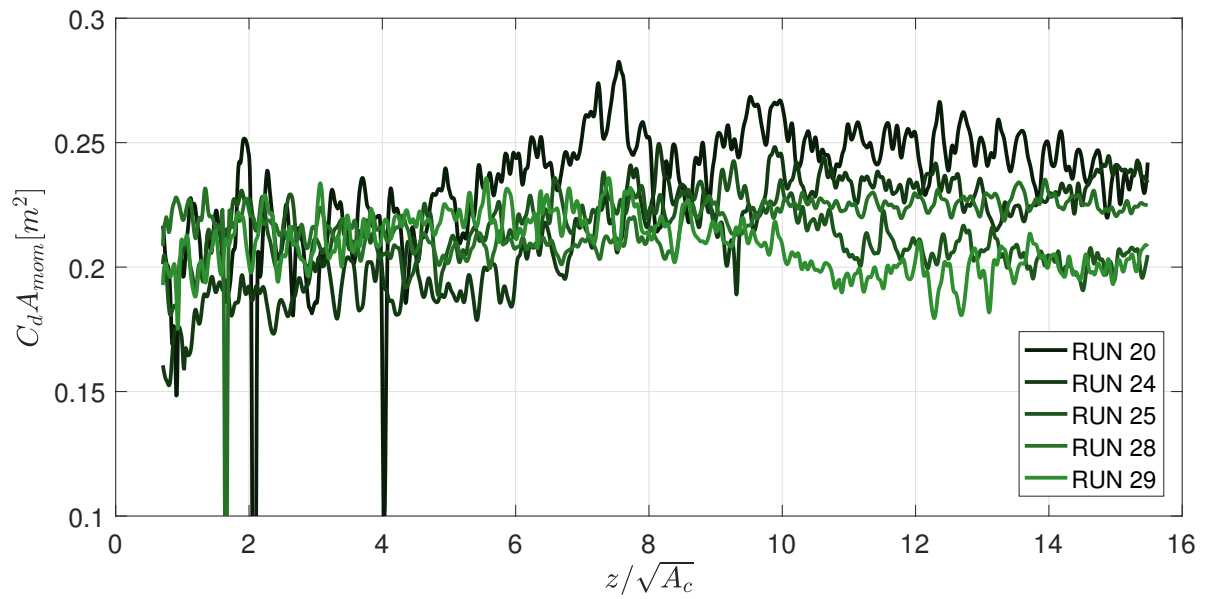
In the High-Speed ROF, the streamwise median of the standard deviation is about 9% of the mean drag area, thus it is comparable with the value for the experiment with the Low-Speed ROF in dynamic conditions (9% for time-trial and 7% for upright). However, in Spoelstra (2017) some planes have a drag standard deviation much higher than 20% of the mean drag area, especially for the first planes, while it is never above 15% for the current experiment. Although this is relevant to obtain near wake information on the cyclist's flow field, it does not have a large effect on the evaluation of the overall drag area for a certain configuration. In fact, one would take wake planes for  $z > 6\sqrt{A_c}$  in order to

avoid the drag area underestimation due to the incorrect evaluation of the pressure term contribution.

Figure 5.20: Momentum term of drag area for five instantaneous randomly sampled runs; Time-Trial Dynamic



(a) Low-Speed ROF, current experiment;  $f = 8\text{Hz}$



(b) High-Speed ROF [Spoelstra \(2017\)](#);  $f = 2\text{kHz}$

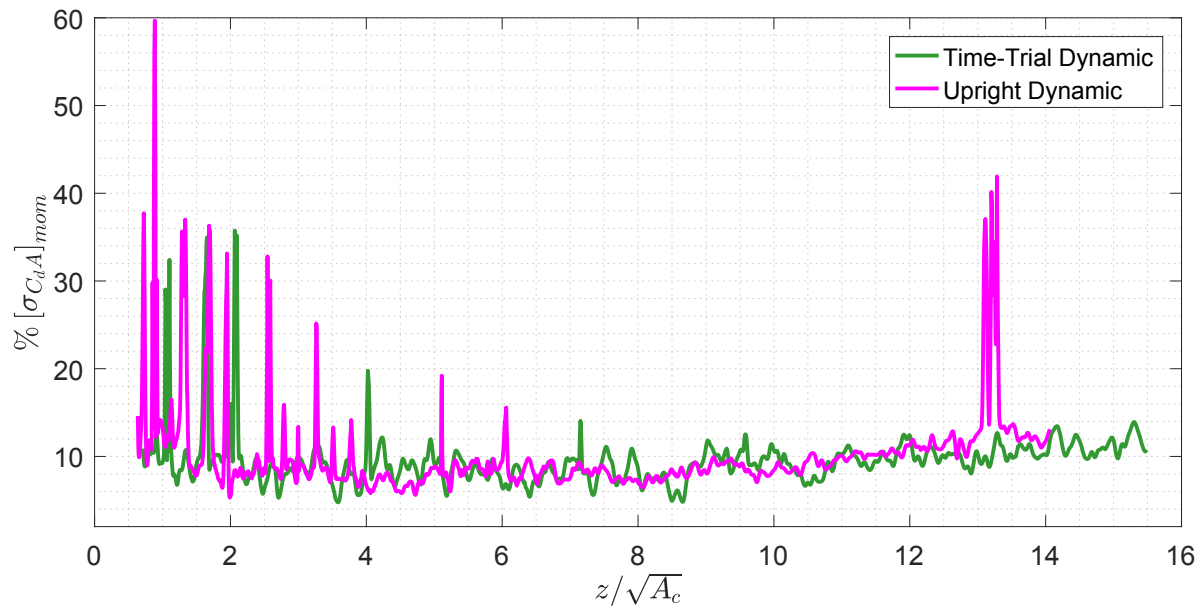


Figure 5.21: Standard deviation of drag area across the runs in the High-Speed ROF (Spoelstra, 2017)



# 6

## Conclusions and Recommendations

### 6.1. Conclusions

This project is initiated by the hypothesis that an indoor implementation of the Ring of Fire with a Low Speed PIV system can provide a more accurate drag determination than in the case of [Spoelstra \(2017\)](#). In order to assess the outcome of the project, the following main research question has been formulated:

*Which drag area precision and time per passage has an indoor Ring of Fire got by using a low-speed Stereo-PIV system and which factors contribute to its precision in comparison to a high-speed system?*

To answer this question, an amateur cyclist has been tested in four configurations: static time-trial posture with asymmetric legs, static time-trial posture with symmetric legs, dynamic time-trial posture and dynamic upright posture. The mean drag area for the four configurations is respectively  $0.252m^2$ ,  $0.237m^2$ ,  $0.242m^2$ ,  $0.280m^2$  and the drag coefficient is 0.796, 0.761, 0.771, 0.699. The uncertainty on the mean drag area is well below 2% in all the three cases, with 95% confidence level. The standard deviation of the streamwise drag area is between 4% and 9%, depending on the tested configuration, and never above 15%. In the experiment of [Spoelstra \(2017\)](#), the standard deviation of the streamwise drag area is about 9% and never above 60%. Furthermore, the Low-Speed ROF measured a difference in drag area equal to 6% between two configurations.

In this experiment each cyclist's passage is performed in a time frame between one to two minutes, while a High-speed PIV system as in [Spoelstra \(2017\)](#) requires a time frame between five to ten minutes.

The mean drag area for the four studied configurations falls within the values of the reported literature. Moreover, the main flow structures and wake dynamics are identified, as the presence of hip, inner thighs and ankle-calf vortices reported by [Crouch et al. \(2014, 2016a\)](#). The static cases exhibit flow asymmetry and symmetry for the  $\varphi = 75^\circ$  and  $\varphi = 15^\circ$  respectively, as in [Crouch et al. \(2014, 2016a\)](#). Additional vortex structures for the upright posture are recognised, with comparable strength and position to [Spoelstra \(2017\)](#).

Differently from [Terra et al. \(2016\)](#), [Shah \(2017\)](#), [Jux \(2017\)](#), [Spoelstra \(2017\)](#), an upper pair of vortices is noticed as main contributor to the wake dynamics, possibly originated by a higher position of the cyclist's head. Moreover, a balanced vortex quadrupole consisting of the hip and inner thigh vortices is not noticed in the symmetric case: the repeatability in this posture during the campaign is ascribed as the cause. As a consequence, it is believed that its corresponding drag area has been overestimated.

Reduced vorticity in the wake for the symmetric leg posture reduces the standard deviation of the streamwise drag area up to 4%. The asymmetric static configuration has got a standard deviation on the drag area evaluated across the planes and the passages equal to  $0.02m^2$ . The dynamic configurations for  $k = 0.119$  have the corresponding standard deviation 10% to 30% higher than the asymmetric

static one. However, when comparing the percentage standard deviation over the mean drag area, the asymmetric static one is 8%, and the the dynamic one is between 8% and 11%. Therefore, the fluctuations due to the unsteady pedalling motion play a limited role in the drag standard deviation.

The current Low-Speed PIV system permits a  $DSR = 25$  and a  $DVR = 250$ , both higher than the High-Speed PIV system used by Spoelstra (2017), who estimated a  $DSR = 16$  and  $DVR \approx 100$ . Conducting the experiment in an indoor facility reduces by a factor two to three the environmental turbulence intensity with respect to an outdoor experiment, with a mean streamwise velocity component of the order of 1% of the cyclist's speed. This low environment velocity in the indoor experiment, the high measured  $DVR$  and the fact that a constant variation of  $u_i = 0.025\text{m/s}$  can offset  $C_d A$  by 10% (appendix B) highlight that the PIV measurement error has got the same order of magnitude as the environment flow in the indoor experiment. Therefore, this experiment has been limited in the accuracy of the velocity of the upstream flow.

Both the low-speed PIV system and the execution of the experiment indoor contribute at improving the PIV particle per pixel level in terms of average value and uniformity. This is linked to the cross-correlation SNR, which has been found to have an influence on the drag area standard deviation. Despite these improvements, the  $DSR$  for the current experiment is still limited by the lack of uniformity in seeding distribution within the same plane and among different tests.

The mean drag area is found to vary streamwise with a typical trend featuring two zones: an initial steep growth with quickly decreasing rate for  $z < 6\sqrt{A_c}$  and a barely constant plateau for  $z > 6\sqrt{A_c}$ . No phase-dependent trend is recognisable in the dynamic cases, as in Spoelstra (2017). The trend is ascribed to the limitations in evaluating the pressure term contribution on the mean drag area. The latter decreases from 5% to 1% in the near wake. An exception to this trend occurs only when the cyclist's wake exceeds the measurement area. This phenomenon mostly occurs for the asymmetric static condition and it is attributed to the sidewash induced by the vortex asymmetry. The growth of the wake area is linearly proportional to  $(z/\sqrt{A_c})^{0.5}$ .

The evaluation of the drag area depends on the chosen upstream plane. Closer upstream planes are affected by the stagnation pressure of the cyclist and can lead to an underestimated drag. Time-averaged upstream flow permits to obtain reduced noise on the flow velocity and reduced drag area standard deviation.

The cyclist's speed is measured by both a magnetic sensor and a set of images acquired by a high-speed camera. For the same streamwise location the cyclist's speed from the magnetic sensor never exceeds 3% of the speed measured with the high-speed camera. In addition, it provides time information on the cyclist's speed, allowing for a more accurate evaluation of the cyclist's drag area. From a practical point of view, it is less expensive and requires less storing and processing time than a high-speed camera.

The implementation of a synchronisation system between the cyclist's passage and the image acquisition offers limited improvements in the phase-locked averaging procedure, given the presence of a delay with a standard deviation of the order of  $60\text{ms}$ . An additional manual correction is necessary to mitigate its limitations but an error on it has an effect in particular on the flow field analysis of the near wakes.

As a major conclusion, it can be summarised that the Low-Speed Indoor Ring of Fire has got higher  $DVR$ ,  $DSR$ ,  $ppp$ ,  $SNR$ , lower peak-locking, more precise drag area, more accurate instantaneous flow fields, lower measurement time and postprocessing time than the High-Speed Outdoor Ring of Fire.

## 6.2. Recommendations

Based on the drawn conclusions, it is recommended to employ a Low-Speed PIV system for future Ring of Fire experiments. The only exception to prefer a High-Speed system regards the studies aiming at obtaining volumetric data for the cyclist's wake. Moreover, as it has been noticed that the median of the

streamwise standard deviation of the drag area is of similar order of magnitude as for the High-Speed ROF, it is suggested to perform further evaluation of the Low-Speed PIV system with cameras with a sensor size as large as the ones used in [Spoelstra \(2017\)](#). In fact, the benefits of the current Low-Speed PIV system are limited by the small magnification factor used to acquire the full cyclist's wake: better contrasted and brighter particles as well as larger particle image diameters can be obtained with larger sensor size for low-speed cameras with similar pixel size.

The accuracy of the speed evaluation of a magnetic sensor has been verified with respect to the high-speed camera procedure and the current author recommends that future experiments do not need a high-speed camera for this purpose, with the aforementioned advantages in cost and time.

An improvement of the synchronisation system is advised to obtain more accurate phase-locked flow fields. This especially concerns the software side.

From the experiment timeline the necessity of five people was highlighted to conduct the campaign. Therefore, it is strongly recommended to implement an automatic system to open remotely the curtains of the seeding container, to reduce the employees' cost by two. The automatic system can permit the use of a curtain at the entrance of the tunnel, thus further increasing seeding density.

Given the absent effect of the crank angle variation on the streamwise drag area, it is advised to perform continuous test passages without excessive care in the procedure concerning a starting crank angle from rest. This only holds when there is interest in drag area measurements rather than flow field data for a specific crank angle and it can lead to further reduced experiment times.

### 6.2.1. Further works

Finally, some following future investigations are advised in both short and long term.

In general, bias errors of the system have not been evaluated yet in the same on-site conditions. Deceleration methods or linear regression analysis based on powermeters could be a possible choice. In the first case, a magnetic sensor software providing higher time resolved data is required; in the second case, longer riding distances are required to obtain valuable measurements.

Based on the results of this Low-Speed PIV system, the light source for PIV illumination could be changed. As already imagined by [Sciacchitano \*et al.\* \(2015\)](#), the Low-Speed ROF with a larger sensor camera could potentially not require the use of a laser light but a LED could be afforded, with the advantages of lower cost and safety issues.

Improvements on the accurate estimation of instantaneous drag area require to derive the unsteady term contribution in eq.2.2 for a transiting object in the Ring of Fire reference frame. An unsuccessful effort was made by the current author in this respect, leading to strong overestimation in the drag area. Furthermore, the control volume derivation can progress further with a verification of the effect of the spatially variable environmental fluctuations, as discussed in appendix B.

As a long-term improvement, the author foresees the integration of the measurement system with an optical tracking one. Accurate corrections on the cyclist's posture can be provided to the user and taken into account to optimise performance and to correct the repeatability issues in the measurement. Understandably, this requires higher accuracy in measuring the instantaneous drag area.



# Bibliography

- A. Sciacchitano, G. Caridi, and F. Scarano, *A quantitative flow visualization technique for on-site sport aerodynamics optimization*, *Procedia Engineering* **112**, 412 (2015).
- A. Spoelstra, *Aerodynamics of transiting objects via large-scale PIV - the Ring of Fire Concept*, Master's thesis, Technische Universiteit Delft (2017).
- T. Crouch, D. Burton, N. Brown, M. Thompson, and J. Sheridan, *Flow topology in the wake of a cyclist and its effect on aerodynamic drag*, *Journal of Fluid Mechanics* **748**, 5 (2014).
- T. Crouch, D. Burton, M. Thompson, N. Brown, and J. Sheridan, *Dynamic leg-motion and its effect on the aerodynamic performance of cyclists*, *Journal of Fluid and Structures* **65**, 121 (2016a).
- R. Lukes, S. Chin, and S. Haake, *The understanding and development of cycling aerodynamics*, *Sports Engineering* **8**, 59 (2005).
- T. Crouch, D. Burton, Z. LaBry, and K. Blair, *Riding against the wind: a review of competition cycling aerodynamics*, *Sports Engineering* **20**, 81 (2017).
- C. Jux, *Robotic volumetric particle tracking velocimetry by coaxial imaging and illumination*, Master's thesis, Technische Universiteit Delft (2017).
- T. Defraeye, B. Blocken, E. Koninckx, P. Hespel, and J. Carmeliet, *Computational fluid dynamics analysis of cyclist aerodynamics: Performance of different turbulence-modelling and boundary-layer modelling approaches*, *Journal of Biomechanics* **43**, 2281 (2010a).
- T. Crouch, M. Thompson, D. Burton, J. Sheridan, and N. Brown, *Dominant flow structures in the wake of a cyclist*, 30th AIAA Applied Aerodynamics Conference 2012 , 2022 (2012a).
- M. Griffith, T. Crouch, M. Thompson, D. Burton, J. Sheridan, and N. Brown, *Computational fluid dynamics study of the effect of leg position on cyclist aerodynamic drag*, *Journal of Fluids Engineering* **136**, 101105 (2014).
- W. Terra, A. Sciacchitano, and F. Scarano, *Evaluation of aerodynamic drag of a full-scale cyclist model by large-scale tomographic-PIV*, International Workshop on Non-Intrusive Optical Flow Diagnostics (2016).
- D. Giaquinta, *The flow topology of the Ahmed body in cross-wind*, Master's thesis, Technische Universiteit Delft (2018).
- P. Lallement, *Velocipede*, Patent US 000059915 (United States Patent and Trademark Office, 1866).
- AeroVelo, *ETA AeroVelo human powered*, <http://www.aerovelo.com/> (2016), accessed: 2018-05-03.
- G. Atkinson, R. Davison, A. Jeukendrup, and L. Passfield, *Science and cycling: Current knowledge and future directions for research*, *Journal of Sports Sciences* **21**, 767 (2003).
- H. Chowdury and F. Alam, *Bicycle aerodynamics: an experimental evaluation methodology*, *Sports Engineering* **15**, 73 (2012).
- C. Kyle and E. Burke, *Improving the racing bicycle*, *Mechanical Engineering* **106**, 34 (1984).
- J. Martin, D. Milliken, J. Cobb, K. McFadden, and A. Coggan, *Validation of a mathematical model for road cycling power*, *Journal of Applied Biomechanics* **14**, 276 (1998).

- J. Anderson, *Fundamentals of Aerodynamics*, 5th ed. (McGraw-Hill series in Aeronautical and Aerospace Engineering, 2011).
- G. Gibertini and D. Grassi, *Cycling aerodynamics*, in *Sport Aerodynamics*, edited by H. Nørstrud (Springer Vienna, Vienna, 2008) pp. 23–47.
- P. Debraux, F. Grappe, A. Manolova, and W. Bertucci, *Aerodynamic drag in cycling: methods of assessment*, *Sports Biomechanics* **10**, 197 (2011).
- T. Nonweiler, *The air resistance of racing cyclist*, Tech. Rep. 106 (The College of Aeronautics Cranfield, 1956).
- C. Kyle, *The aerodynamics of handlebars and helmets*, *Cycling Science* **1** (1989).
- F. Grappe, R. Candau, A. Belli, and J. D. Rouillon, *Aerodynamic drag in field cycling with special reference to the Obree's position*, *Ergonomics* **40**, 1299 (1997).
- T. Defraeye, B. Blocken, E. Koninckx, P. Hespel, and J. Carmeliet, *Aerodynamic study of different cyclist positions: Cfd analysis and full-scale wind-tunnel tests*, *Journal of Biomechanics* **43**, 1262 (2010b).
- N. Barry, D. Burton, J. Sheridan, M. Thompson, and N. Brown, *Aerodynamic performance and riding posture in road cycling and triathlon*, *Proceedings of the Institution of Mechanical Engineers, Part P: Journal of Sports Engineering and Technology* **229**, 28 (2015).
- G. Tew and A. Sayers, *Aerodynamics of yawed racing cycle wheels*, *Journal of Wind Engineering and Industrial Aerodynamics* **82**, 209 (1999).
- C. Capelli, G. Rosa, F. Butti, G. Ferretti, A. Veicsteinas, and P. di Prampero, *Energy cost and efficiency of riding aerodynamics bicycle*, *European Journal of Applied Physiology* **67**, 144 (1993).
- R. Hill, *The design and development of the lotussport pursuit bicycle*, *Proceedings of the Institution of Mechanical Engineers, Part D: Journal of Automobile Engineering* **207**, 285 (1993).
- L. Oggiano, L. Bardal, C. Sæter, and L. Saetran, *Dynamic measurements and drag crisis hysteresis in garment aerodynamics*, *Procedia Engineering* **60**, 99 (2013).
- T. Crouch, D. Burton, J. Venning, M. Thompson, N. Brown, and J. Sheridan, *A comparison of the wake structures of scale and full-scale pedalling cycling models*, *Procedia Engineering* **147**, 13 (2016b).
- T. Crouch, J. Sheridan, D. Burton, M. Thompson, and N. Brown, *A quasi-static investigation of the effect of leg position on cyclist aerodynamic drag*, *Procedia Engineering* **34**, 3 (2012b).
- J. Zhou, R. Adrian, S. Balachandar, and T. Kendall, *Mechanisms for generating coherent packets of hairpin vortices in channel flow*, *Journal of Fluid Mechanics* **387**, 353 (1999).
- F. Scarano, *Tomographic PIV: principles and practice*, *Measurement Science and Technology* **24**, 012001 (2013).
- J. Jeong and F. Hussain, *On the identification of a vortex*, *Journal of Fluid Mechanics* **285**, 69 (1995).
- S. Roa, D. Ferreira, L. Muñoz, and O. Lòpez, *Analysis of aerodynamic drag on cycling based on complementary numerical and experimental studies*, *Proceedings of the ASME Design Engineering Technical Conference* **3** (2016), 10.1115/DETC2016-60287.
- T. Defraeye, B. Blocken, E. Koninckx, P. Hespel, and J. Carmeliet, *Computational fluid dynamics analysis of drag and convective heat transfer of individual body segments for different cyclist positions*, *Journal of Biomechanics* **44**, 1695 (2011).
- T. Defraeye, B. Blocken, E. Koninckx, P. Hespel, P. Verboven, B. Nicolai, and J. Carmeliet, *Cyclist drag in team pursuit: Influence of cyclist sequence, stature, and arm spacing*, *Journal of Biomechanics* **136**, 011005 (2014).
- B. Blocken, T. Defraeye, E. Koninckx, J. Carmeliet, and P. Hespel, *Cfd simulations of the aerodynamic drag of two drafting cyclists*, *Computers and Fluids* **71**, 435 (2013).

- L. Oggiano, L. Spurkland, L. Sætran, and L. Bardal, *Aerodynamical resistance in cycling on a single rider and on two drafting riders: Cfd simulations, validation and comparison with wind tunnel tests*, *Communications in Computer and Information Science* **632**, 22 (2016).
- J. Barlow, W. Rae, and A. Pope, *Low-speed wind tunnel testing*, 3rd ed. (John Wiley and Sons, 1999).
- R. Candau, F. Grappe, M. Ménard, B. Barbier, G. Millet, M. Hoffman, A. Belli, and J. Rouillon, *Simplified deceleration method for assessment of resistive forces in cycling*, *Medicine and Science in Sports and Exercise* **31**, 1441 (1999).
- B. Celis and H. Ubbens, *Design and construction of an open-circuit wind tunnel with specific measurement equipment for cycling*, *Procedia Engineering* **147**, 98 (2016).
- M. Bäckström, P. Carlsson, J. Danvind, A. Koptuyug, D. Sundström, and M. Tinnsten, *A new wind tunnel facility dedicated to sports technology research and development*, *Procedia Engineering* **147**, 62 (2016).
- M. Unal, J.-C. Lin, and D. Rockwell, *Force prediction by PIV imaging: A momentum-based approach*, *Journal of Fluids and Structures* **11**, 965 (1997).
- B. Van Oudheusden, F. Scarano, E. Roosenboom, E. Casimiri, and L. Souverein, *Evaluation of integral forces and pressure fields from planar velocimetry data for incompressible and compressible flows*, *Experiments in Fluids* **43**, 153 (2007).
- F. Scarano, S. Ghaemi, G. Caridi, J. Bosbach, U. Dierksheide, and A. Sciacchitano, *On the use of helium-filled soap bubbles for large-scale tomographic PIV in wind tunnel experiments*, *Experiments in Fluids* **56**, 42 (2015).
- B. Van Oudheusden, *PIV-based pressure measurement*, *Measurement Science and Technology* **24**, 032001 (2013).
- Y. Shah, *Drag analysis of full scale cyclist model using large-scale 4D-PTV*, Master's thesis, Technische Universiteit Delft (2017).
- SRM, *Our story of success; from the first powermeter to the gold standard of power measurement*, <http://www.srm.de/company/history/> (2015), accessed: 2018-05-06.
- S. Watkins and F. Alam, *The turbulent flow field relevant to outdoor sports*, *Procedia Engineering* **72**, 792 (2014).
- W. Terra, A. Sciacchitano, and F. Scarano, *Aerodynamic drag of a transiting sphere by large-scale tomographic-PIV*, *Experiments in Fluids* **58**, 83 (2017).
- R. Hanna, *Cfd in sport - a retrospective; 1992 - 2012*, *Procedia Engineering* **34**, 622 (2012).
- R. Adrian, *Dynamic ranges of velocity and spatial resolution of particle image velocimetry*, *Measurement Science and Technology* **8**, 1393 (1997).
- M. Raffael, C. Willert, S. Wereley, and J. Kompenhans, *Particle Image Velocimetry: a practical guide*, 2nd ed. (Springer, 2007).
- R. Mei, *Velocity fidelity of flow tracer particles*, *Experiments in Fluids* **22**, 1 (1996).
- A. K. Prasad and R. J. Adrian, *Stereoscopic particle image velocimetry applied to liquid flows*, *Experiments in Fluids* **15**, 49 (1993).
- A. Prasad, *Stereoscopic particle image velocimetry*, *Experiments in Fluids* **29**, 103 (2000).
- A. Schroeder and C. E. Willert, *Particle Image Velocimetry, New Developments and Recent Applications*, 1st ed. (Springer-Verlag Berlin Heidelberg, 2008).
- A. K. Prasad and K. Jensen, *Scheimpflug stereocamera for particle image velocimetry in liquid flows*, *Applied Optics* **34**, 7092 (1995).

- C. Willert, *Stereoscopic digital particle image velocimetry for application in wind tunnel flows*, *Measurement Science and Technology* **8**, 1465 (1997).
- B. Wieneke, *Stereo-PIV using self-calibration on particle images*, *Experiments in Fluids* **39**, 267 (2005).
- G. C. A. Caridi, *Development and application of helium-filled soap bubbles: For large-scale PIV experiments in aerodynamics*, *Ph.D. thesis*, Technische Universiteit Delft (2018).
- J. Bosbach, M. Kühn, and C. Wagner, *Large scale particle image velocimetry with helium filled soap bubbles*, *Experiments in Fluids* **46**, 539 (2009).
- M. Kühn, K. Ehrenfried, J. Bosbach, and C. Wagner, *Large-scale tomographic particle image velocimetry using helium-filled soap bubbles*, *Experiments in Fluids* **50**, 929 (2011).
- R. Adrian and C. Yao, *Pulsed laser technique application to liquid and gaseous flows and the scattering power of seed materials*, *Applied Optics* **24**, 44 (1985).
- G. C. A. Caridi, D. Ragni, A. Sciacchitano, and F. Scarano, *HFSB-seeding for large-scale tomographic PIV in wind tunnels*, *Experiments in Fluids* **57**, 190 (2016).
- R. Adrian, *Particle-imaging techniques for experimental fluid mechanics*, *Annual Review of Fluid Mechanics* **23**, 261 (1991).
- R. Hain, C. Kähler, and C. Tropea, *Comparison of CCD, CMOS and intensified cameras*, *Experiments in Fluids* **42**, 403 (2007).
- M. Falchi and G. Romano, *Evaluation of the performance of high-speed PIV compared to standard PIV in a turbulent jet*, *Experiments in Fluids* **47**, 509 (2009).
- A. Sciacchitano and B. Wieneke, *PIV uncertainty propagation*, *Measurement Science and Technology* **27**, 084006 (2016).
- C. Meinhart, S. Wereley, and J. Santiago, *A PIV algorithm for estimating time-averaged velocity*, *Journal of Fluids Engineering* **122**, 285 (2000).
- A. Mohebbian and D. E. Rival, *Assessment of the derivative-moment transformation method for unsteady-load estimation*, *Experiments in Fluids* **53**, 319 (2012).
- J.-Z. Wu, Z.-L. Pan, and X.-Y. Lu, *Unsteady fluid-dynamic force solely in terms of control-surface integral*, *Physics of Fluids* **17**, 1 (2005).
- D. E. Rival and B. van Oudheusden, *Load-estimation techniques for unsteady incompressible flows*, *Experiments in Fluids* **58** (2017), 10.1007/s00348-017-2304-3.
- D. F. Kurtulus, F. Scarano, and L. David, *Unsteady aerodynamic forces estimation on a square cylinder by TR-PIV*, *Experiments in Fluids* **42**, 185 (2007).
- D. Ragni, B. Van Oudheusden, and F. Scarano, *Non-intrusive aerodynamic loads analysis of an aircraft propeller blade*, *Experiments in Fluids* **51**, 361 (2011).
- Giant-Bicycles, *2018 trinity advanced pro tt*, <https://www.giant-bicycles.com/us/showcase/trinity-advanced-pro-tt> (2017), accessed: 2018-03-02.
- Imperx, *Bobcat IGV-B1610*, Tech. Rep. (SICK, 2013) [https://www.imperx.com/wp-content/uploads/Legacy-Cameras/GigE-IGV/bobcat\\_IGV-B1610.pdf](https://www.imperx.com/wp-content/uploads/Legacy-Cameras/GigE-IGV/bobcat_IGV-B1610.pdf), Accessed: 2017-10-02.
- Quantel, *Evergreen Laser Series*, Tech. Rep. (Quantel Laser, 2015) [https://www.quantel-laser.com/tl\\_files/client/MY%20QUANTEL%20SPACE/Sales%20Literature/EverGreen\\_Specs\\_EN\\_072015.pdf](https://www.quantel-laser.com/tl_files/client/MY%20QUANTEL%20SPACE/Sales%20Literature/EverGreen_Specs_EN_072015.pdf), Accessed: 2018-03-06.
- SICK, *WS/WE12L-2P410*, Tech. Rep. (SICK, 2017) [https://www.sick.com/media/pdf/2/62/362/dataSheet\\_WS\\_WE12L-2P410\\_1018256\\_en.pdf](https://www.sick.com/media/pdf/2/62/362/dataSheet_WS_WE12L-2P410_1018256_en.pdf), Accessed: 2017-09-29.

- Garmin, *Understanding how the garmin bike speed sensor (bss) measures speed*, <https://support.garmin.com/faqSearch/en-US/faq/content/9NL91YJSJd3Tnyif9jRSy6> (2018), accessed: 2018-03-03.
- ANT™, *ANT Message Protocol and Usage*, Tech. Rep. (Dynastream Innovations Inc., 2014) <https://www.thisisant.com/resources/ant-message-protocol-and-usage/>, Accessed: 2018-03-03.
- C. Willert and M. Gharib, *Digital particle image velocimetry*, *Experiments in Fluids* **10**, 181 (1991).
- J. Westerweel, *Digital particle image velocimetry - Theory and application*, Ph.D. thesis, Technische Universiteit Delft, Delft University Press, Delft (1993), <http://resolver.tudelft.nl/uuid:85455914-6629-4421-8c77-27cc44e771ed>.
- R. Keane and R. Adrian, *Theory of cross-correlation analysis of PIV images*, *Applied Scientific Research* **49**, 191 (1992).
- J. Westerweel and F. Scarano, *Universal outlier detection for PIV data*, *Experiments in Fluids* **39**, 1096 (2005).
- G. Haller, *An objective definition of a vortex*, *Journal of Fluid Mechanics* **525**, 1 (2005).
- F. M. White, *Viscous Fluid Flow*, 3rd ed. (McGraw Hill Education, 2011).
- T. Morel and G. Sovran, *The effect of base slant on the flow pattern and drag of three-dimensional bodies with blunt ends*. (Boston, MA: Springer, 1978) in G. Sovran, T. Morel, and W. T. J. Mason (Eds.), *Aerodynamic Drag Mechanisms of Bluff Bodies and Road Vehicles* (pp. 191–226).

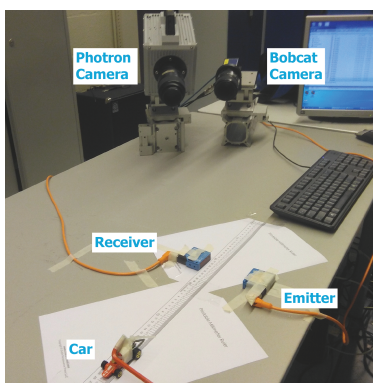


# A

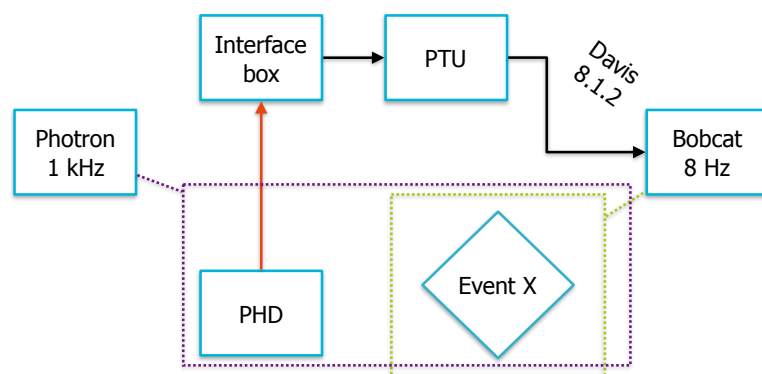
## Determination of the synchronisation system delay

In section 3.4 the implementation of a synchronisation system between the image acquisition and the cyclist's passage was discussed. The aim of the synchronisation system based on a through beam photoelectric sensor was to ensure a similar relative position between the cyclist and the acquired wakes, when comparing different cyclist's passages. Such a sensor is referred as a photodetector device hereafter. The synchronisation process is important to compute the averaged flow field variables, but it is not necessary to compute instantaneous and mean drag areas, if the drag pressure term is not considered. Its necessary implementation is a weak point of a Low-Speed PIV system for the Ring of Fire, as the high frequency in the High-Speed ROF allows for a streamwise relocation of the planes among the instantaneous passages with high precision. In fact, for the case of Spoelstra (2017), with  $\overline{U}_c = 8m/s$  and  $f = 2kHz$ , every wake was  $4mm$  distant from each other, which is a negligible value considering that the average laser thickness was about  $40mm$ .

For the synchronisation system, differences between two triggering modes have been discussed, highlighting that in principle mode 2 is potentially the one providing the best synchronisation among different passages. This potentiality could be spoiled by a non-constant initial delay of the triggering system. Given the photodetector delay being lower than  $0.2ms$ , the possible presence of a larger delay variation would be ascribed to the software part of the triggering system. In this appendix, a second experimental campaign aiming at measuring the mean delay and its standard deviation is presented.



(a) Experiment Setup



(b) Experiment setup schematic

The experiment setup is shown in Fig.A.1a and schematically summarised in Fig.A.1b. On one side it replicates the same hardware-software setup as the Ring of Fire experiment: image acquisition by the Imperx Bobcat IGV-B1610 is performed with a  $f = 8Hz$ , after a triggering signal is provided to the Programmable Timing Unit by the photodetector (PHD). The Bobcat camera observes an event

X occurring and the external trigger signal is sent by the software Davis 8.1.2 through mode 2. In addition, a Photron Fastcam SA-1 is placed from a similar viewpoint so that both the occurring event X and the photodetector are recorded with a frequency of  $1\text{kHz}$ . When the photodetector laser beam is interrupted by a transiting object, a small light on the top of the receiver is switched off and the triggering signal is sent to the interface box.

The occurring event X consists of a small toy car transiting over a printed ruler with millimetre resolution. A screw mounted in the back of the car allows to locate the car position on the ruler with millimetre precision. In order to understand the procedure to compute the synchronisation system delay, consider the schematic in Fig.A.2. Firstly, the low frequency image (ImgX) for a certain millimetre position is selected. Then, the high frequency image (ImgX) for the same position is searched by the user. The ratio of the difference between the image at which event X is occurring and the photodetector light switches off (ImgPHD) over the Photron acquisition frequency ( $1\text{kHz}$ ) is the time interval between event X and the photodetector being triggered. By subtracting the time between the same event X image and the first acquired image (Img1) by the low speed camera, it is possible to measure the synchronisation system delay.

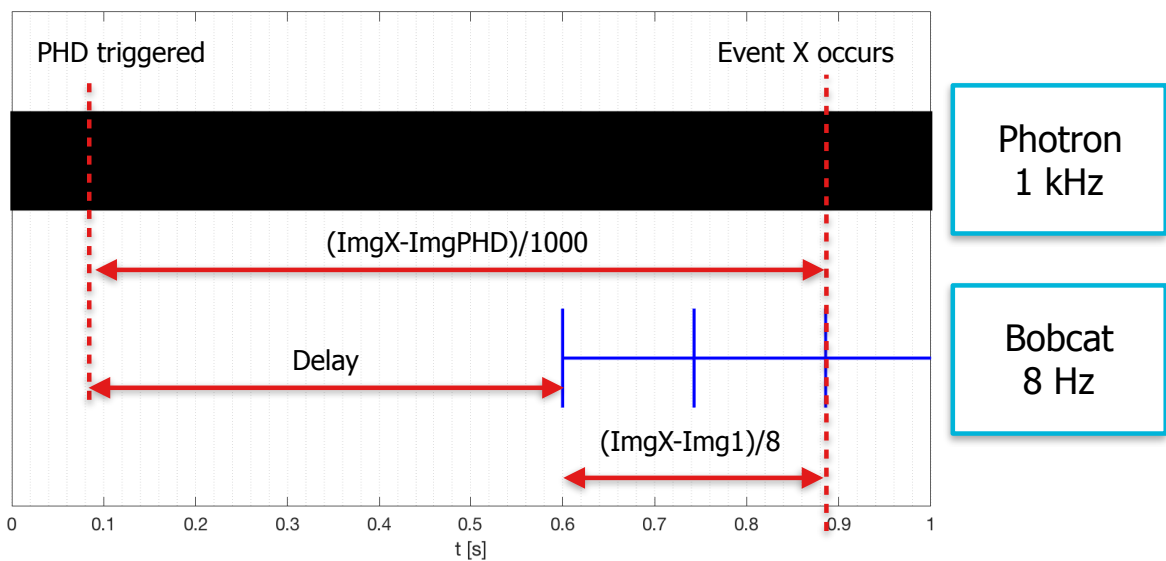


Figure A.2: Measurement procedure to quantify the synchronisation system delay

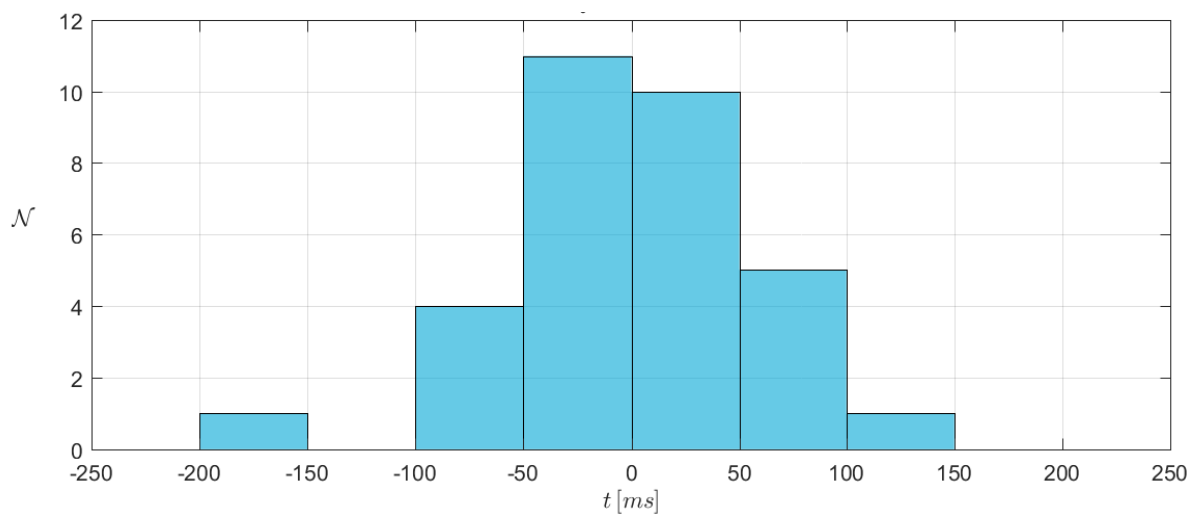


Figure A.3: Frequency distribution of the synchronisation system delay

The experiment is repeated over 31 samples and the corresponding delay frequency distribution is shown in Fig.A.3, after the mean delay equal to 0.685s being subtracted. Rather than the mean, the relevant statistical parameter is the delay standard deviation, equal to 58.5 ms, as it is the one influencing an error in averaging the velocity fields for the same  $n$ -th acquired downstream plane.

**Imprecision in the streamwise wake position** To provide an idea of the effect of such a delay, consider the imprecision in the wake position  $\sigma_x$ . The relative position  $\Delta x$  of the wake with respect to the cyclist is based upon the cyclist mean speed  $\overline{U}_c$  and the number of wakes  $n$  acquired downstream of the cyclist. However, the wakes corresponding to the same numbered plane acquired after the cyclist (for instance the first wake acquired after the cyclist) are never in the same relative position to the cyclist. There are two main sources of uncertainty that cause that: the cyclist speed fluctuation  $\sigma_u$  along different test runs (if the cyclist's speed fluctuation within the same test is disregarded) and the delay fluctuation  $\sigma_t$  in the synchronisation system. The difference between the mean relative streamwise position  $\overline{\Delta x}$  and its imprecision  $\sigma_x$  is provided in eq.A.1:

$$\overline{\Delta x} = \overline{U}_c (n\Delta t) \quad (\text{A.1})$$

$$\Delta x = \overline{\Delta x} \pm \sigma_x = (\overline{U}_c \pm \sigma_u) (n\Delta t \pm \sigma_t) = \overline{U}_c (n\Delta t) \pm \sigma_u n\Delta t \pm \overline{U}_c \sigma_t + \sigma_u \sigma_t$$

where the imprecision in both time, velocity and position has been written in the equation just for one standard deviation. The worst case scenario occurs when all the imprecisions sum up as in Fig.A.4. Consider that the imprecision in the wake position depends on the considered wake ( $n$ ): in fact, the imprecision in determining the relative position is higher if the further downstream planes are considered. Moreover, the relative importance of the cyclist's speed fluctuation and the one of the synchronisation system varies streamwise, as depicted in Fig.A.4 for the upright dynamic case, which had the highest cyclist's speed fluctuation. In the bottom figure the relative weight of the three factors contributing to  $\sigma_x$  is evaluated: the fluctuation of the synchronisation system is always more relevant for the first wakes. Therefore, it is advised to prioritise any improvement on the synchronisation system rather than on the fluctuating cyclist speed. Finally, notice in the top plot that the overall imprecision (with only one standard deviation for both  $\sigma_u$  and  $\sigma_t$ ) is always higher than half the characteristic length of the cyclist, which is of the same order of magnitude as the average separation  $\overline{U}_c \Delta t$  between two wakes: this justifies the necessity of the manual streamwise relocation described in section 4.1.

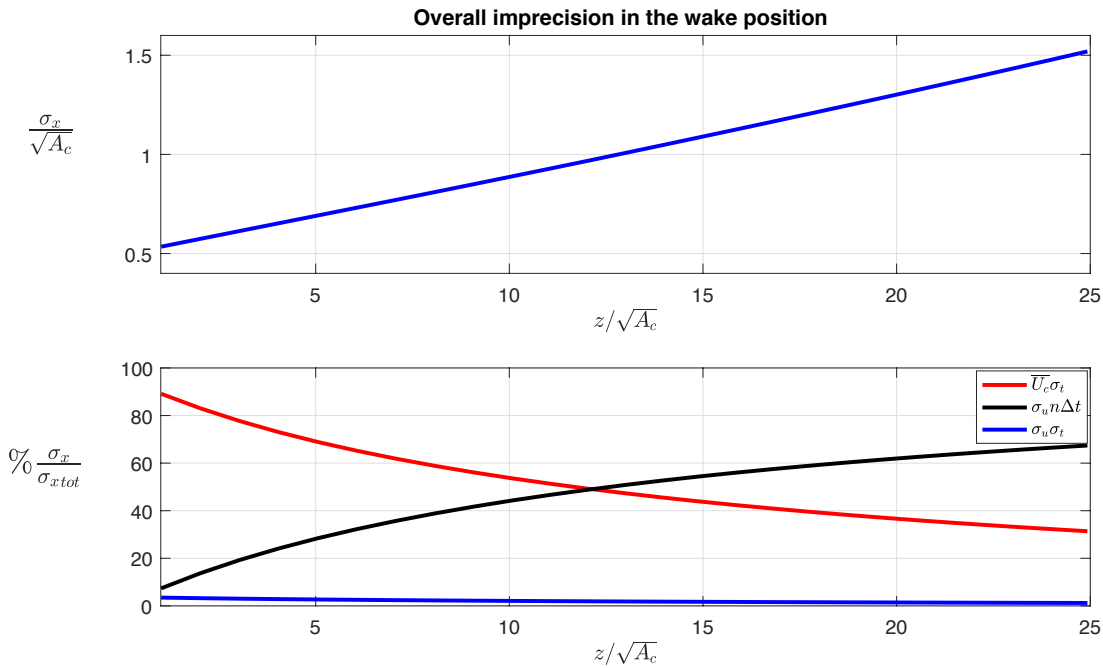


Figure A.4: Streamwise variation of the imprecision in attributing the wake position relative to the cyclist



# B

## On the influence of the environment spatial variation

In section 2.2.2, the equations for momentum conservation within a control volume in the Ring of Fire reference frame have been derived based on the analogy with a typical wind tunnel reference frame. This has followed the previous applications of the control volume approach for transiting objects as in Terra *et al.* (2017) and Spoelstra (2017). Nevertheless, it was highlighted that in this derivation a spatial uniformity of the environmental fluctuation in the upstream acquired plane is implicitly assumed. Understandably, this is not true in reality, as shown in section 4.7.

The main advantage of this assumption is that it does not require the user to know or assume which is the upstream plane area that guarantees mass and momentum conservation, so that the same measurement plane area can be used for both the inlet and the outlet of the control volume.

In this appendix, the extent of the relevance of this assumption on the drag area results is discussed. Furthermore, the validity of the necessity of measuring the upstream flow (Terra *et al.*, 2017) is questioned with regards to the current experiment.

**Spatially constant environment flow** In section 4.7, the effect of the choice of the upstream plane on the drag computation has been established. It has been concluded that a time-average of the flow field in front of the cyclist can provide more precise drag area.

In order to estimate the effect of the implicit assumption of a spatially constant environment fluctuation, the upright posture is reconsidered. The mean momentum term of the drag area is computed in the same way as in the current project, with an exception for the upstream flow. In fact, after averaging the flow field for each test passage along multiple upstream planes, the spatial average is taken and assigned to each bin within the measurement plane. This means that the momentum deficit is evaluated by subtracting a spatially constant velocity for each test passage, and the implicit assumption in 2.6 is respected.

This mean value is positive and between 0.02 and 0.05m/s on average, so about 1% of the cyclist velocity. This is coherent with the flow shown in Fig.4.14. In Fig.B.1 the results are presented. It can be seen that there is no relevant effect on the mean drag area, neither on the uncertainty. In particular, the largest difference occurs for the farthest plane, where the mean differs of 0.4%. The drag uncertainty is equal up to the fourth digit in  $m^2$ .

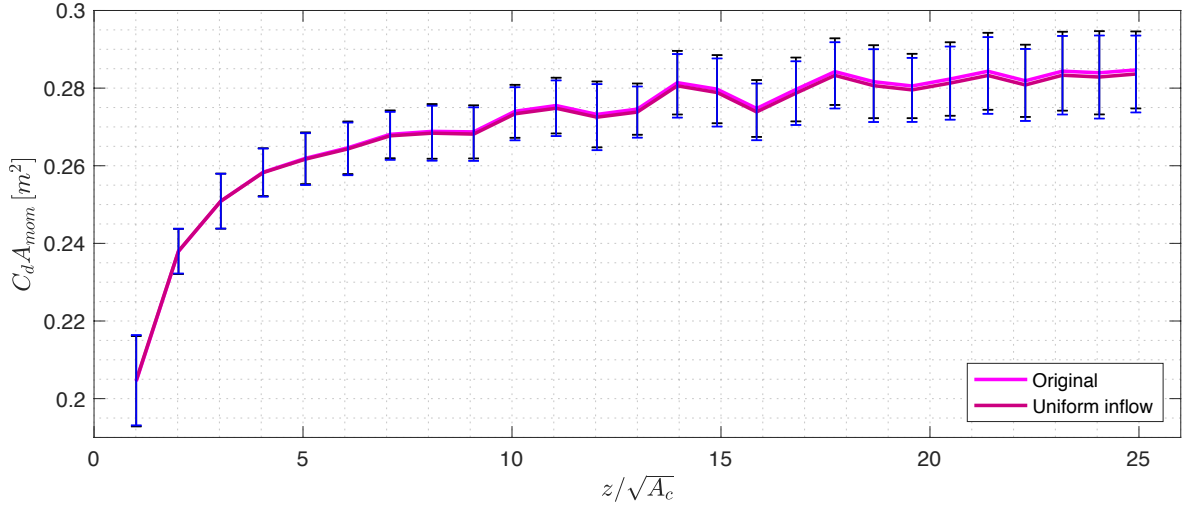


Figure B.1: Streamwise mean momentum term of  $C_d A$  for dynamic upright configuration; effect of constant inflow

**Null environment flow** Given the previous result and the measured spatial mean streamwise velocity in the upstream planes, its effect on the drag evaluation could be regarded as negligible. To verify that, the drag area is evaluated without the environment flow. The plot in Fig.B.2 shows that this is not the case and an accurate drag measurement requires to evaluate the environment flow before the passage of the cyclist. In fact, the mean drag area difference is above 10%, and the uncertainty on the mean is about 1% higher.

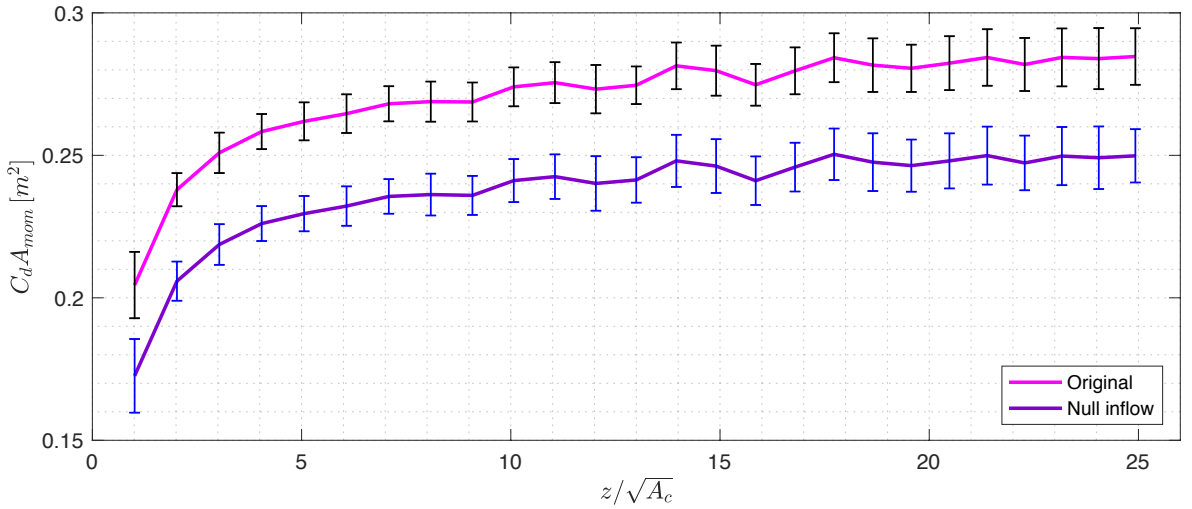


Figure B.2: Streamwise mean momentum term of  $C_d A$  for dynamic upright configuration; effect of null inflow

As this result might be counter-intuitive, consider eq.2.8. Although the mean environment flow can be equal to  $0.05\text{m/s}$ , its contribution  $C_d A_{[u_i]}$  to the drag area can be written as:

$$C_d A_{[u_i]} = \frac{-u_i(x, y) \cdot (U_c - u_o(x, y)) \cdot S_{meas}}{0.5U_c^2} \quad (\text{B.1})$$

with  $S_{meas}$  the measurement plane area and constant grid cell size. Since  $S_{meas} = 3.12\text{m}^2$ , if we assume a constant  $u_i = 0.025\text{m/s}$ , a spatially constant velocity deficit equal to  $0.05U_c$ , so that  $U_c - u_o = 5 - 0.25 = 4.75\text{m/s}$ , then we obtain  $C_d A_{[u_i]} = -0.03\text{m}^2$ .

**Conclusions** In this section, the effect of the assumption of spatially constant inflow is considered. It has been shown that a constant upstream flow does not affect the drag evaluation while a null

upstream flow can underestimate the drag area up to more than 10%.

It is crucial to stress that the first result is good to have an idea about the possible effect of negligible spatial variation of the flow, but not satisfactory. In fact, not only a mathematical proof has not been derived, but even this simple evaluation is based on the constant flow assumption embedded in eq.2.8. A proper comparison would require to compute the drag area by knowing the shape of the two distinct inlet and outlet control volume surfaces and apply momentum conservation.